

UNIVERSITY OF SOUTHAMPTON

Applications of Microfluidics in Nuclear Magnetic Resonance

by

William G Hale

A thesis submitted in partial fulfillment for the
degree of Doctor of Philosophy

in the
Faculty of Engineering and Physical Sciences
School of Chemistry

April 2019

UNIVERSITY OF SOUTHAMPTON

ABSTRACT

FACULTY OF ENGINEERING AND PHYSICAL SCIENCES
SCHOOL OF CHEMISTRY

Doctor of Philosophy

by William G Hale

Microfluidics is a constantly growing field of research finding applications in a diverse range of subjects such as materials science, chemistry and across the life sciences. This is due to many advantageous attributes that microfluidics enjoys, namely small sample volumes which contribute to waste reduction and reduced cost of experimentation; highly controllable local environments that enable very precise investigation of changes in systems to stimuli; rapid prototyping techniques meaning make, test, tweak cycles can be run more than once in a typical day; ease of parallelisation makes gathering statistically significant data much easier without the need to repeat experiments for days at a time; and ease of automation increases precision and repeatability.

Nuclear magnetic resonance (NMR) spectroscopy is widely applied technique in chemistry and the life sciences. Its non-invasive and non-destructive nature makes it ideal to study living, or mass limited samples. However, it is limited by having to have an extremely homogenous magnetic field as well as the low sensitivities possible in a typical experiment.

This thesis describes methods for integrating these two fields. Some NMR experiments being ‘miniaturised’ to be performed ‘on-chip’ as well as microfluidic concepts that have been engineered to be compatible with NMR techniques. These techniques do not seek to replace established methods of microfluidic analysis such as mass spectrometry or fluorescence spectroscopy but could be used to compliment these techniques as an additional method of extracting data from the system.

Contents

Nomenclature	xvii
Acknowledgements	xix
1 Introduction	1
1.1 Microfluidics	1
1.2 NMR theory	2
1.2.1 Classical NMR	2
1.2.1.1 Spin	2
1.2.1.2 Population	3
1.2.1.3 Nuclear spin precession	4
1.2.1.4 Magnetisation as a vector	4
1.2.1.5 Pulses and rotating frame	5
Rotating frame	5
Pulses	6
1.2.1.6 Fourier Transform NMR	7
1.2.1.7 Chemical Shift and J-coupling	9
1.2.1.8 Relaxation	10
1.2.2 Quantum description of NMR	11
1.2.2.1 Nuclear Spin	11
1.2.2.2 Spin States	12
1.2.2.3 Operators	14
1.2.2.4 Superoperators	15
1.2.2.5 Density Operator	16
1.2.2.6 The Hamiltonian	18
1.3 Micro-NMR	20
1.3.1 Sensitivity	21
1.3.1.1 Signal to noise ratio	21
1.3.2 Limit of Detection	23
1.3.3 Concentration limit of detection	23
1.3.4 Transmission line probe	24
2 Microfluidic Droplet NMR	27
2.1 Abstract	27
2.2 Introduction	27
2.2.1 Susceptibility	29
2.2.2 Matching susceptibilities in emulsions	30

2.3	Materials and Methods	35
2.4	Results and Discussion	38
2.5	Conclusion	43
3	Parahydrogen induced polarisation	45
3.1	Abstract	45
3.2	Hyperpolarisation	46
3.2.1	Sensitivity	46
3.2.2	Signal Averaging	46
3.2.3	Hyperpolarisation - not sure on order here	47
3.2.4	Techniques	48
3.2.4.1	Brute Force	48
3.2.4.2	Dynamic Nuclear Polarisation	48
3.3	Parahydrogen Induced Polarisation - PHIP	49
3.3.1	Parahydrogen	49
3.3.2	PASADENA and ALTADENA	51
3.3.2.1	Spin Physics	51
3.4	Introduction	55
3.5	Materials and methods	57
3.6	Results and Discussion	59
3.6.1	ALTADENA	59
3.6.2	PASADENA	60
3.6.3	Signal Analysis	62
3.6.4	Hydrogen Transport	63
3.6.5	Sensitivity and Limit of Detection	65
3.6.6	2D NMR	69
3.7	Conclusions	70
4	An NMR compatible on-chip Peristaltic Pump	73
4.1	Introduction	73
4.1.1	Materials and Methods	76
4.2	Results and Discussion	78
4.2.0.1	Peristaltics	78
4.2.0.2	Characterisation of flow	79
4.2.1	<i>In situ</i> operation of the device	81
4.3	Conclusions	83

List of Figures

1.1	Energy level and ΔE of the two energy levels for a spin-1/2 nucleus	3
1.2	Magnetisation shown as a vector in red, at equilibrium, is orientated on the z -axis. A $\pi/2$ pulse rotates the vector to the xy -plane where it begins to precess around the z -axis.	4
1.3	In the rotating frame the effective field, B_{eff} , is the vector sum of the reduced field, B_{red} and the B_1 field. θ is the tilt angle defined between B_{red} and B_{eff}	6
1.4	A) A graphical representation used to describe a pulse sequence, the width and height of the block refer to the power and duration of pulse respectively, the line represents the acquisition of signal. B)(1) The magnetisation lies in equilibrium along the z -axis. (2) The $\pi/2_y$ pulse rotates the magnetisation around the y -axis. (3) The magnetisation precesses in the xy -plane around the z -axis and returns to thermal equilibrium	6
1.5	A) a magnetisation vector precesses in the xy -plane, eventually returning to equilibrium. B) A plot of the magnetisation along z -axis (yellow) and the x -axis (blue) during the relaxation.	11
1.6	The projection of two states in a spin 1/2 nucleus (red arrow) with the magnitudes indicated (black arrow)	12
1.7	Drawings of the detector assembly and the microfluidic device (1). A: front view (dimensions in mm); B: exploded view. Spacer (4) ensures the alignment of the sample chamber with the constrictions on the PCB planes. In A, PCB plane 5 is hidden to show the orientation of 1 with respect to PCB plane 3. Thickness of each of the PCB planes is 1.52 mm and the copper layers on the PCBs is $35 \mu \text{m}$. Both the microfluidic device and the spacer are made from PMMA and have thickness of 0.9 mm and 1 mm respectively. Figure reproduced from[1]	24
1.8	Plot comparing the limits of detection of previously design micro-NMR detectors. Letters a-t correspond to different authors as cited by Badilita <i>et al.</i> [2] Letters u[3] and t[4] represent more recent work. The probe used here is labelled at TLP and a comercial cyroprobe is shown for reference.	25
2.1	Summary graphic of the work in [5]. This shows how the NMR spectrum of glucose changes in a susceptibility mismatched chip but by cutting shimstructures around the sample chamberhigh resolution NMR is still possible despite the mismatches.	31
2.2	Droplet chip design (left) and detail micrograph of the sample chamber area filled with droplets (right). Some droplets are also visible in the entrance and exit channels.	32

- | | | |
|-----|---|----|
| 2.3 | A: Finite element simulation of relative magnetic field distribution in an uncompensated chip (circular structures filled with PMMA) filled with cyclohexane and B: a compensated chip filled with cyclohexane; C: a linear plot of relative magnetic field along the z-axis through the middle of the sample chamber. | 34 |
| 2.4 | A: Finite element simulation of magnetic field distribution in droplets. z-component of the reduced magnetic field H_{red} in an isolated spherical droplet and B: in a face-centred cubic arrangement of droplets; C: FEM mesh used to calculate the result shown in B; D: histograms of the z-component of the reduced magnetic field in the continuous (orange) and in the droplet (blue) phase in the FCC arrangement. | 35 |
| 2.5 | ^1H NMR line shapes of water (left) and cyclohexane (right) of a water in cyclohexane emulsion as a function of $\text{Eu}[\text{DTPA}]^{2-}$ concentration in the aqueous phase normalised to the sharpest peak. The spectra given in black are the pure phase spectra produced by the same chip. | 36 |
| 2.6 | Predicted ^1H NMR line shapes of water (left) and cyclohexane (right) of a water in cyclohexane emulsion as a function of $\text{Eu}[\text{DTPA}]^{2-}$ concentration in the aqueous phase. | 37 |
| 2.7 | Observed line widths of water (blue circles) and cyclohexane (orange circles) in microfluidic droplet emulsions as a function of the $\text{Eu}[\text{DTPA}]^{2-}$ concentration in the aqueous phase. Inset is the plot around the minimum concentration. The widths of both lines are minimal at the matched concentration of 23.75 mM. | 39 |
| 2.8 | B_0 Field maps obtained by magnetic resonance imaging of emulsions with (A) $\Delta\chi = -1.41 \times 10^{-6}$ and (B) $\Delta\chi \approx 0$. | 39 |
| 2.9 | Spectra of 200 mM Glucose in H_2O obtained from microfluidic droplet emulsions in cyclohexane. 1: Aqueous phase contains $c_0 = 23.75 \pm 0.25$ mM $\text{Eu}[\text{DTPA}]^{2-}$. Spectra 2-7 have been obtained by gradual dilution of the aqueous phase with small amounts of DI water. 2: $\ln c/c_0 = -0.5\%$; 3: $\ln c/c_0 = -0.75\%$; 4: $\ln c/c_0 = -0.875\%$; 5: $\ln c/c_0 = -1.0\%$; 6: $\ln c/c_0 = -1.125\%$; 7: $\ln c/c_0 = -1.25\%$. A spectrum of pure phase 200mM glucose with optimised Eu doping in the same chip is included for comparison (black). The nonuniform peak at 4.8 ppm is due to carrier frequency drift during water suppression | 42 |
| 3.1 | Left: The rotational energy levels of para- and orthohydrogen with their associated J values. Right: a graph showing the fraction of para- and orthohydrogen as a function of temperature. The dotted line shows 50% para enrichment that is achieved by cooling to 77K using liquid nitrogen. Image taken from [6]. | 50 |
| 3.2 | Above: Populations of states represented as balls in a thermal (left) and a PASADENA experiment. Below: Simulations of spectra arising from adding thermal hydrogen to a molecule (left) and of a PASADENA experiment when adding parahydrogen. | 53 |
| 3.3 | Correlation diagram for the ALTADENA effect. Hydrogenation at low field populates the singlet state, adiabatically increasing the field carries the population into a high field state. | 54 |
| 3.4 | Top: Populations of Zeeman states represented by balls for thermal(left) and ALTADENA(right) experiments. Bottom: Simulations of a thermal spectrum after applying a $\pi/4$ pulse and an ALTADENA experiment. | 54 |

3.5	Overview of the PHIP@chip experiment. a: scheme of the hydrogenation reaction; b: CAD rendering of the chip assembly with individual chip layers separated, consisting of the PMMA chip, PDMS membrane, and two 3D printed holders with threads for the gas and fluid connections; The hydrogen gas diffuses through the PDMS membrane into the flowing liquid; c: Outline drawing of the chip (dimensions in mm).	55
3.6	Ortho-para conversion of hydrogen in PDMS after various times under vacuum.	58
3.7	A) Liquid channel (blue) and hydrogen channel (red) as scored onto the PMMA layer of the device. B) A 3D render of the hydrogenation device used for the ALTADENA experiments.	60
3.8	Spectra obtained from i) a thermal hydrogenation and ii) a parahydrogenation of propargyl acetate to give allyl acetate with hydrogens derived from parahydrogen labelled a and b. By comparison of SNR the enhancement for the ALTADENA experiment is 200.	61
3.9	Drawing of PHIP@chip setup. It shows the solution (blue line) of propargyl acetate, catalyst and methanol being fed into the magnet via a syringe pump. Simultaneously, parahydrogen (red line) is fed in at the desired pressure and regulated by a mass flow controller to a flow rate of 20 ml min^{-1} . Both of these are fed into the microfluidic device depicted in Fig. 3.5	62
3.10	Proton NMR spectra obtained in continuous flow. a: Buildup of the hyperpolarised signal after initiation of flow; b: hyperpolarised NMR spectrum. Antiphase doublets from the two hyperpolarised protons A and B are clearly visible at 5.2 ppm and 5.9 ppm, respectively. c: control spectrum obtained with thermal H_2 gas. Top right: traces b and c with the vertical axis expanded by a factor of 10.	63
3.11	Finite element simulation of hydrogen uptake. a: Diffusive hydrogen flux in the PDMS membrane for different liquid flow rates; b: final hydrogen concentration in flowing methanol as a function of flow rate. Dashed line: simulation, open circles: NMR measurements.	64
3.12	Labelled ^1H spectrum acquired using a flow rate of $2 \mu \text{ l min}^{-1}$ and a normal hydrogen pressure of 5 bar. The spectrum was collected using 64 transients with a delay of 5 seconds.	64
3.13	Saturation recovery results. a: signal buildup at constant flow rate after saturation; b: magnitude of the steady-state signal after full recovery (at least 100 s after saturation) as a function of flow rate. A clear maximum at $8 \mu \text{ l min}^{-1}$ is observed. c: single-scan steady-state spectrum obtained at the optimum flow rate with para-enriched H_2 ; d: spectrum obtained with hydrogen gas in thermal equilibrium. 512 transients have been averaged. Signal enhancement by PHIP was determined by comparing the integral of the positive lobe of signal A in spectrum c to the integral of the corresponding (purely absorptive) peak in spectrum d.	67

- 3.14 Signal recovery after saturation, normalised by the maximum signal observed at long recovery times. The horizontal axis is the volume moved through the chip during the recovery time τ_r , i.e., $q\tau_r$, where q is the flow rate. Filled circles correspond to flow rates below the optimum ($q < 8 \mu\text{l min}^{-1}$), whereas open circles are obtained at flow rates $q \geq 8 \mu\text{l min}^{-1}$. The solid and dashed lines are guides to the eye for the solid and open circle data points, respectively. 67
- 3.15 The continuous flow PHIP@chip approach allows acquisition of two-dimensional spectra with very high sensitivity. Left pane: experimental 2D NMR spectra of the hyperpolarised reaction mixture, flowing at $8 \mu\text{l min}^{-1}$, along with simulations (right). The diagonal in the TOCSY spectrum is marked by a dashed grey line. Only the protons originating from parahydrogen give signals on the diagonal; the polarisation is transferred to the other locations by the isotropic mixing sequence. The $^1\text{H}-^{13}\text{C}$ HMQC NMR spectrum shows two separate multiplets, each correlating one of the two hyperpolarised protons with the directly bonded ^{13}C spin. The ^{13}C traces in the HMQC spectrum are shown in absolute mode. Right pane (top): Pulse sequences used to acquire TOCSY and HMQC spectra. Right pane (bottom): 1D ^1H spectrum obtained in directly after a single $\pi/4$ pulse (top) and after applying the MLEV-17 isotropic mixing sequence (bottom). This demonstrates that the hyperpolarisation can be spread throughout the J -coupling network. 68
- 4.1 A) A 3D scale diagram of an elastomeric peristaltic pump. The channels are 100 m wide and 10 m high. Peristalsis was typically actuated by the pattern 101, 100, 110, 010, 011, 001, where 0 and 1 indicate “valve open” and “valve closed,” respectively. B) Pumping rate of a peristaltic micropump versus various driving frequencies. this figure is reproduced from[7] 74
- 4.2 A cut-through view of the valves in the device showing how when air pressure is applied the PDMS membrane is pushed down and seals the small hole cut in the middle layer. 77
- 4.3 3D render of a single valve with 3D printed layer shown too 77
- 4.4 A CAD drawing of the chip designed for pumping and mixing. Inner (red) and outer (blue) liquid circuits; liquid ports (A-D) and valve positions (1-6) shown 79
- 4.5 A 3D representation of the device with separate layers of chips and PDMS layers shown. 80
- 4.6 Micrographs of A: free chip showing two valves B: An assembled device with an open valve C: An assembled device with a closed valve, the arrows indicate the area where the PDMS is in contact with the PMMA and is sealing the hole. 81
- 4.7 An arduino controller is connected to, and powered by, a laptop via USB. The controller is connected to a darlington array via six 5V logic connections (shown in red) when addressed, these allow the corresponding pin opposite to draw power from the +24V connected from an outside source. The blue lines indicate the wires carrying 24V to the solenoid bank which are pneumatically connected to the valves in the chip as labelled. 82
- 4.8 Plot of the total volume pumped vs time for a chip in the open configuration 82
- 4.9 Flow rates produced by the pump at different frequencies. 83

- 4.10 NMR spectra recorded with 16 transients on a device containing 100mM Sodium acetate in the inner circuit and 100mM DSS in the outer circuit. . 84

List of Tables

2.1 Bulk magnetic susceptibilities	33
--	----

Listings

Nomenclature

w The weight vector

Acknowledgements

Thanks to no one.

To ...

Chapter 1

Introduction

1.1 Microfluidics

- What is it? Microfluidics is a broad term that covers a wide variety of research, it is classified by the analysis of small volumes of liquids usually nL to μ l in doing so it offers a numerous benefits. The small volumes involved make it ideal to study mass limited samples, as in macromolecular chemistry or protein classification in biochemistry whilst reducing the costs associated with these experiments. Microfluidic systems possess precisely defined geometry of paths which enable control of mixing and separation of fluids, this also lends itself well to the control of the microenvironment with the device. Devices usually consist of cheap fabrication materials such as polydimethylsiloxane (PDMS) or polymethyl methacrylate (PMMA).
- Why do we want to use it? - The fine control of reaction conditions allows for precise investigations of reaction kinetics - Currently, NMR not widely used in microfluidics and can be used to provide extra information on the system can also be used in conjunction with existing methods of analysis in microfluidics (mass spec, fluorescence) as NMR leaves sample unperturbed, perfect for *in situ* monitoring of living systems. Coupling could take the form of a longitudinal NMR metabolomic study of cells whilst monitoring specific protein expression with fluorescence.
- Who uses it?(What has been done in literature?) - need help with this, maybe discuss with Marcel?
- Goal - combination without compromise (MF + μ NMR) - We'd like to incorporate functional microfluidic experiments with high resolution NMR spectroscopy. In such a way that the validity either part, microfluidic or magnetic resonance, remains intact. In that way not only would NMR become a more widely used

tool for the microfluidic toolbox it could also become a valuable attachment to compliment existing tools. However, this combination is not without significant challenges. Firstly, a probe capable of μ NMR must be designed, that fits with a removable chip for ease of parallelisation. This probe must be of comparable performance to existing probes, to maintain validity, and work with existing magnets and spectrometers. Secondly, the chip, and any functionality that it possesses, must fit into the bore of the magnet which is typically around 38 mm in diameter. Thirdly, materials used in construction of the chip must be non-magnetic and susceptibility matched to the sample of interest so it can enable high resolution NMR. Lastly, the device used must be bio-compatible as most applications in microfluidics are in some way biological. -Motivation:

1.2 NMR theory

Nuclear magnetic resonance (NMR) theory can be described using two approaches:

1. The classical approach, in which the nuclei are thought of as small bar magnets which rotate in 3D space. Experiments can be described by approximating the net magnetisation as a vector in 3D space.
2. The quantum mechanical approach, in which each spin in the system is in a distinct quantised state. Operators are used to describe the state of a system as a whole. Experiments are described by propagating these operators.

The theory described in this chapter is mainly from [8, 9] and is intended to provide sufficient background knowledge in order for the reader to understand later chapters.

1.2.1 Classical NMR

1.2.1.1 Spin

Nuclei, often modelled as a clump of neutrons and protons surrounded by electrons at the centre atoms, have a property referred to as spin.

In fact, nuclear spin is an intrinsic property of the nucleus and can take half or whole integer values, including 0. In this thesis we will be mainly concerned about one spin- 1/2 nucleus, the proton (^1H), with another spin-1/2 nucleus ^{13}C making sparse appearances. Just like in this thesis, ^{13}C only has an $\approx 1\%$ abundance in nature with the other $\approx 99\%$ ^{12}C having a spin-0 nucleus.

All spin-1/2 nuclei possess a magnetic dipole moment and behave rather like small bar magnets in that, when placed in an external magnetic field they have a tendency to

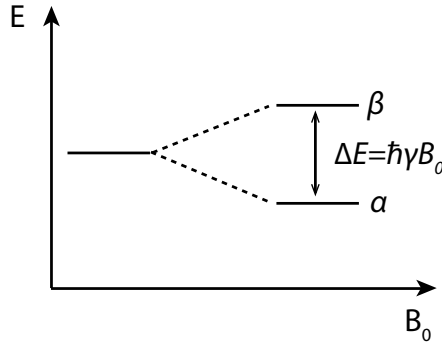


FIGURE 1.1: Energy level and ΔE of the two energy levels for a spin-1/2 nucleus

align with the field. In NMR this external field is called B_0 , and is orientated along the z -axis.

1.2.1.2 Population

In a magnetic field a spin-1/2 nucleus has two energy levels with a separation that is proportional to the strength of the magnetic field a schematic is show in Fig. 1.1. We label these levels α and β .

When measuring a group of spins each spin can exist in either the α or β state and overall the spins have a slight preference for the lower energy state, α . This preference can be quantified by calculating the difference in populations (P) which at thermal equilibrium is governed by the Boltzmann distribution:

$$\frac{P_\beta}{P_\alpha} = \exp\left\{\frac{-\Delta E}{k_B T}\right\} \quad (1.1)$$

where P_β/P_α is the population ratio between the states, k_B is Boltzmann constant, and T is the temperature. The polarisation, p , of a system of spin-1/2 nuclei is

$$p = \frac{P_\alpha - P_\beta}{P_\alpha + P_\beta} \quad (1.2)$$

For a system in an NMR experiment which typically operates at $298K$ and a field of 14.1 T the polarisation level is circa 10^5 meaning That the spins are aligned weakly in the same direction as the magnetic field. It is this small polarisation that gives rise to the NMR signal and why NMR is famed for sensitivity issues. One possible solution to this will be described in a later chapter.

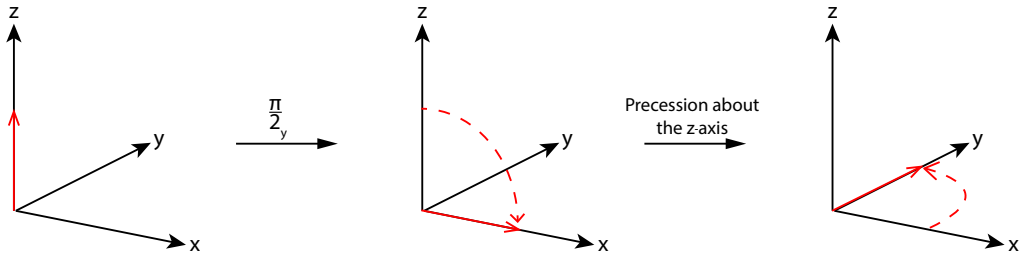


FIGURE 1.2: Magnetisation shown as a vector in red, at equilibrium, is orientated on the z -axis. A $\pi/2$ pulse rotates the vector to the xy -plane where it begins to precess around the z -axis.

1.2.1.3 Nuclear spin precession

When placed in a magnetic field, the nuclei will precess around the axis of the field at a rate known as the larmour frequency defined as:

$$\omega_j^0 = -\gamma_j B_0 \quad (1.3)$$

where γ_j is the gyromagnetic ratio for a nucleus, j . The gyromagnetic ratio is typically 10s of MHz T⁻¹ that give larmour frequencies in the 100s of MHz in an NMR experiment.

1.2.1.4 Magnetisation as a vector

The net magnetic moment of a spin ensemble can be modelled by a 3D vector that can rotates in space. The essence of this is shown in Fig. 1.2. Magnetisation is intially taken to be orientated along the z -axis, this is called longitudinal magnetisation. It is then rotated into the xy -plane which is called transverse magnetisation that then precesses about the z -axis.

How this vector changes in a magnetic field is described using the Bloch equations[10]. These are a group of differential equations that describe how the magnetisation vector components evolves in time in the presence of orthogonal magnetic fields.

$$\frac{dM_x(t)}{dt} = \gamma(M_y(t)B_z(t) - M_z(t)B_y(t)) \quad (1.4)$$

$$\frac{dM_y(t)}{dt} = \gamma(M_z(t)B_x(t) - M_x(t)B_z(t)) \quad (1.5)$$

$$\frac{dM_z(t)}{dt} = \gamma(M_x(t)B_y(t) - M_y(t)B_x(t)) \quad (1.6)$$

where M_a is the magnetisation vector component along the a -axis, B_a is the magnetic field along the a -axis, and γ is the gyromagnetic ratio as described before.

In the case of processing magnetisation around the z -axis, here denoted B_0 , the Bloch equations can be written as

$$\frac{dM_x(t)}{dt} = \gamma B_0 M_y(t) \quad (1.7)$$

$$\frac{dM_y(t)}{dt} = -\gamma B_0 M_x(t) \quad (1.8)$$

$$\frac{dM_z(t)}{dt} = 0 \quad (1.9)$$

these have the solution

$$\frac{dM_x(t)}{dt} = \cos(\omega^0 t) M_x(0) + \sin(\omega_0 t) M_y(0) \quad (1.10)$$

$$\frac{dM_y(t)}{dt} = \cos(\omega^0 t) M_y(0) + \sin(\omega_0 t) M_x(0) \quad (1.11)$$

$$\frac{dM_z(t)}{dt} = 0 \quad (1.12)$$

where ω^0 is the Larmour frequency from Eqn. 1.3.

1.2.1.5 Pulses and rotating frame

Rotating frame The field, B_0 , of a regular NMR experiment is many Tesla, giving precession frequencies of hundreds of megahertz. These frequencies correspond to radio frequencies in the electromagnetic spectrum. Considering these precessing spins it can be useful to change from a static frame to a rotating frame of reference.

The general case is when the rotating frame is at frequency ω_{rot} , in this frame, the Larmour frequency will appear to be $(\omega - \omega_{rot})$. This is called the offset, Ω and is given by:

$$\Omega = \omega - \omega_{rot} \quad (1.13)$$

It follows from this, that if the apparent Larmour frequency in the rotating frame is different from that in the static frame, it must also be the case that the apparent magnetic field in the rotating frame must be different from the applied field. We can use Eqn. 1.3 to compute the apparent magnetic field, B_0^{red} :

$$\Omega = -\gamma B_0^{red} \quad (1.14)$$

$$\text{hence } B_0^{red} = \frac{\Omega}{\gamma} \quad (1.15)$$

this apparent magnetic field in the rotating frame is called the reduced field.

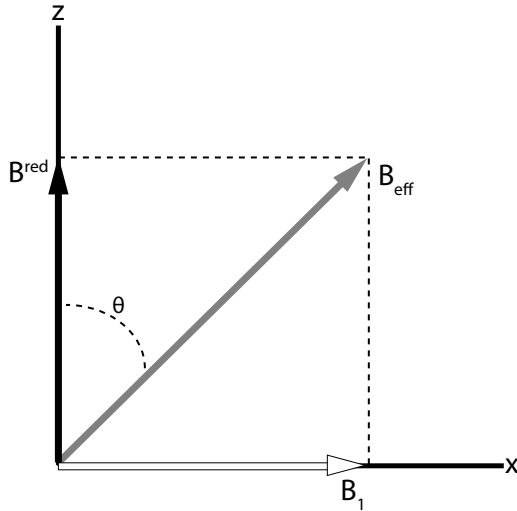


FIGURE 1.3: In the rotating frame the effective field, B_{eff} , is the vector sum of the reduced field, B_{red} and the B_1 field. θ is the tilt angle defined between B_{red} and B_{eff}

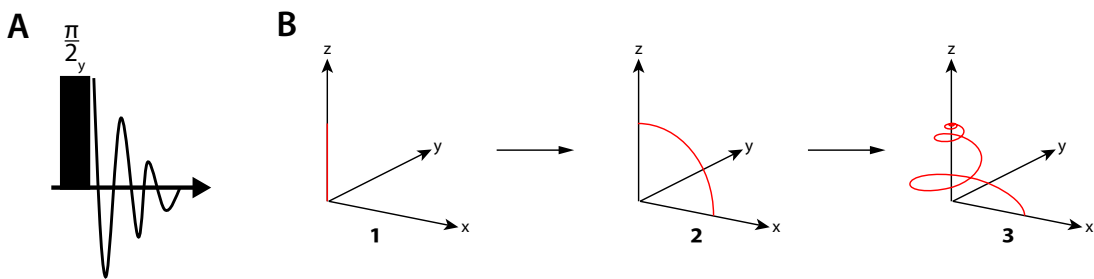


FIGURE 1.4: A) A graphical representation used to describe a pulse sequence, the width and height of the block refer to the power and duration of pulse respectively, the line represents the acquisition of signal. B)(1) The magnetisation lies in equilibrium along the z -axis. (2) The $\pi/2_y$ pulse rotates the magnetisation around the y -axis. (3) The magnetisation precesses in the xy -plane around the z -axis and returns to thermal equilibrium

Pulses In NMR experiments pulses are used to manipulate magnetisation in order to obtain a signal. A pulse can be thought of as a magnetic field oscillating at the frequency of the rotating frame applied in the xy -plane in order to induce precession of the magnetisation. This magnetic field is labelled B_1 and is much smaller in amplitude than B_0 , the actual applied field.

In the static frame, the magnetisation is precessing around B_0 at the Larmour frequency, so a relatively weak B_1 applied along the y -axis, for example, would do little to perturb it, given the effective magnetic field, B_0^{eff} , is calculated by:

$$B_0^{\text{eff}} = \sqrt{(B_1)^2 + (B_0)^2} \quad (1.16)$$

the much larger B_0 dominates here, however, if we apply the B_1 in the rotating frame this becomes

$$B_0^{\text{eff}} = \sqrt{(B_1)^2 + (B_0^{\text{red}})^2} \quad (1.17)$$

and using Eqn. 1.14 as $\omega_{\text{rot}} \rightarrow \omega$, $\Omega \rightarrow 0$ and $B_0^{\text{red}} \rightarrow 0$ so by making the offset small, or zero, the effective field then lies close to the xy -plane and so the magnetisation will be rotated down from z which is what we'd like to achieve for our experiments.

The key, is that although B_0 is much larger than B_1 , we can still affect magnetisation using B_1 by making it oscillate close to the larmour frequency this is the phenomena of resonance. The angle between B_0^{red} and B^{eff} is called the tilt angle, θ . It can be seen from Fig. 1.3 that:

$$\sin(\theta) = \frac{B_1}{B_{\text{eff}}} \quad \cos(\theta) = \frac{B_0^{\text{red}}}{B_{\text{eff}}} \quad \tan(\theta) = \frac{B_1}{B_0^{\text{red}}} \quad (1.18)$$

These radio frequency (rf) pulses are useful because they can be used to address spins at a specific larmour frequency. By applying an rf pulse on resonance with ${}^1\text{H}$ we can manipulate the magnetisation of the nuclei whilst not affecting other spins (e.g. ${}^{13}\text{C}$) contained in the sample.

1.2.1.6 Fourier Transform NMR

In this section we will examine how we can produce an NMR spectrum from the magnetisation of a sample using the rf pulses we introduced.

In NMR we use a pulse sequence to describe the intensity and duration of pulses used in an experiment, shown in Fig. 1.4. The rf pulse, B_1 , is a $\pi/2$ pulse in the y -axis, followed by a signal acquisition. This pulse tips the magnetisation into the xy -plane, and if the pulse length is much less than the precession period (we will assume so), the spins begin to precess freely around the z -axis at the larmour frequency, ω_0 , until they return to the z -axis through a process described in 1.2.1.8.

In a usual NMR experiment the signal is inductively detected. The oscillation of the spins in the sample induces a current in the pick-up coils around the sample, which is detected, amplified and transformed into a spectrum. The resulting free induction decay (FID) is typically an exponentially decaying sinusoidal function. The signal produced from this can be written as:

$$S(t) = \sum_l s_l(t) \quad (1.19)$$

$$s_l(t) = a_l \exp\{-i(\omega_l + \lambda_l)t\} = a_l (\cos(\omega_l t) + i \sin(\omega_l t)) \exp\{-\lambda_l t\} \quad (1.20)$$

where $S(t)$ is the total signal from the sample and s_l are the individual spins. Each spin has an amplitude, a_l , and an associated decay constant, λ_l . The nature of which will be discussed in 1.2.1.8 section. Exponential to trigometric function conversion is done according to Euler's formula: $\exp\{ix\} = \cos(x) + i\sin(x)$.

$S(t)$ is easy to evaluate and interpret if it originates from one spin or a group of spins precessing at precisely the same frequency, however, if there are more spins in the sample processing at different frequencies the FID becomes extremely hard to interpret on its own.

We can clear this picture up however by employing a Fourier transform. This converts the time-domain data into the frequency-domain, such that the total signal in the frequency domain, $S(\omega)$ is the sum of all individual spin signals in the frequency, $S_l(\omega)$:

$$S(\omega) = \sum_l S_l(\omega) \quad (1.21)$$

This allows us to clearly see which resonances are possessed by our spins in the sample. To perform a Fourier transform we must do the following:

$$S_l(\omega) = \int_0^\infty s_l(t)\exp\{-i\omega t\}dt \quad (1.22)$$

and using Eqn. 1.19 can be rewritten:

$$S_l(\omega) = a_l \int_0^\infty \exp\{(-i(\omega + \omega_l) + \lambda_l t\}dt \quad (1.23)$$

sometimes written more concisely as:

$$S(\omega) = \mathcal{F}\{S(t)\}(\omega) \quad (1.24)$$

where $S(t)$ is the signal for the time domain (FID) and $S(\omega)$ is the signal in the frequency domain.

The Fourier transform of our general case is:

$$\mathcal{F}\{S(t)\}(\omega) = a_l \frac{1}{\lambda_l + i(\omega - \omega_l)} \quad (1.25)$$

which is Lorentzian function centered at ω_l with peak width parameter λ_l .

The NMR signal represented in the frequency domain is a spectrum. It is usually many peaks indicating different resonance frequencies of spins in the sample. In the next section we will discuss chemical shift and J-coupling. Two additional effects that when combined with larmour frequencies already discussed forms the NMR spectrum as we know it.

1.2.1.7 Chemical Shift and J-coupling

In a molecule, nuclei are surrounded by clouds of electrons which can shield, or de-sheild, it from the effects of the external field B_0 .

The chemical shielding factor, *sigma*, shifts the resonance frequency of the nuclear spin. We can now include it in Eqn. 1.3:

$$\omega_j^0 = -\gamma_j B_0 (1 - \sigma) \quad (1.26)$$

this chemical shielding is specific to each nucleus in the molecule. It is possible for two or more nuclei to share the same factor. We refer to these as being chemically equivalent.

The shielding is often around 10^{-6} for ${}^1\text{H}$. When plotting and examining spectra it is would not be useful to use absolute frequencies, as discussed they are regularly in the hundreds of MHz, whereas the differences in peaks might only be kHz or less. To combat this we use a relative frequency scale called chemical shift, δ , it is defined as:

$$\delta = \frac{\omega_j - \omega_j^{\text{ref}}}{\omega_j^{\text{ref}}} \quad (1.27)$$

where ω_j is the precession frequency of the nucleus of interest, and ω_j^{ref} is the precession frequency of a reference nuclei. δ is a dimensionless number, unaffected by magnetic field strength, it often small compared to the size of the field and is reported in parts per million (ppm).

In addition to the external B_0 field, the nuclear spins are also affected by the magnetic fields generated by neighboring spins. These magnetic fields are mediated by the electrons in the chemical bonds. This is referred to as spin-spin coupling or *J*-coupling and gives rise to peak splittings in spectra. These splittings, and therefore the values of *J*-couplings, range from a few Hz to a thousand Hz typically. It is an important factor and is incorporated in the quantum description on NMR in 1.2.2.6.

Both of these, σ and *J*-couplings, are tensors this means they depend on the orientation of the molecule and the spin with respect to the magnetic field. In liquids, however, tumble rapidly compared to the timescale of an NMR experiment. This averages the interactions resulting in a scalar quantity for each.

There are additional effects the nuclear spins experience, for example, dipole-dipole coupling which is a through space spin-spin coupling, and quadrupole coupling where there are spins with $>1/2$ values however, these are not relevant to this work.

1.2.1.8 Relaxation

The last part needed to complete our classical understanding of NMR is relaxation. Relaxation is the process of the spin returning to the thermal equilibrium. The thermal equilibrium of spin-1/2 nuclei in a magnetic field is the bulk magnetisation vector pointing in the direction of the B_0 field.

In this system there are two forms of relaxation, T_1 and T_2 . T_1 is the longitudinal relaxation time constant and T_2 is the transverse relaxation time constant the difference between them is shown in Fig. 1.5. T_1 is the rate constant that governs the return of magnetisation to the z -axis from the xy -plane. T_2 on the other hand is the time constant that governs the return of magnetisation to equilibrium in the xy -plane. It is more accurate to say that T_1 is the relaxation rate constant for populations, and T_2 is the relaxation rate constant for coherences, in the density operator (discussed in 1.2.2). But this is incompatible with the classical description of NMR.

We can now complete the Bloch equations from Eqn. 1.4:

$$\frac{dM_x(t)}{dt} = \gamma(M_y(t)B_z(t) - M_z(t)B_y(t)) - \frac{M_x(t)}{T_2} \quad (1.28)$$

$$\frac{dM_y(t)}{dt} = \gamma(M_z(t)B_x(t) - M_x(t)B_z(t)) - \frac{M_y(t)}{T_2} \quad (1.29)$$

$$\frac{dM_z(t)}{dt} = \gamma(M_x(t)B_y(t) - M_y(t)B_x(t)) - \frac{M_z(t) - M_0}{T_1} \quad (1.30)$$

in order to derive M_{xy} we assume the following:

$$M_{xy} = M_x + iM_y \quad \text{and} \quad B_{xy} = B_x + iB_y \quad (1.31)$$

After some algebra we obtain:

$$\frac{dM_{xy}(t)}{dt} = -i\gamma(M_{xy}(t)B_z(t) - M_z(t)B_{xy}(t)) - \frac{M_{xy}(t)}{T_2} \quad (1.32)$$

$$\frac{dM_y(t)}{dt} = i\frac{\gamma}{2}(M_{xy}(t)\overline{B_{xy}}(t) - \overline{M_{xy}}(t)B_z(t)) - \frac{M_y(t)}{T_2} \quad (1.33)$$

$$(1.34)$$

where $\overline{M_{xy}} = M_x - iM_y$ and $\overline{B_{xy}} = B_x - iB_y$ solving these gives:

$$M_z(t) = M_{z,\text{eq}} - (M_{z,\text{eq}} - M_z(0))\exp\left\{-\frac{t}{T_1}\right\} \quad (1.35)$$

$$M_{xy}(t) = M_{xy}(0)\exp\left\{-\frac{t}{T_2}\right\} \quad (1.36)$$

Relaxation occurs when the spins exchange energy with their surroundings. They do this when local magnetic fields, usually caused by the motion of surrounding molecules,

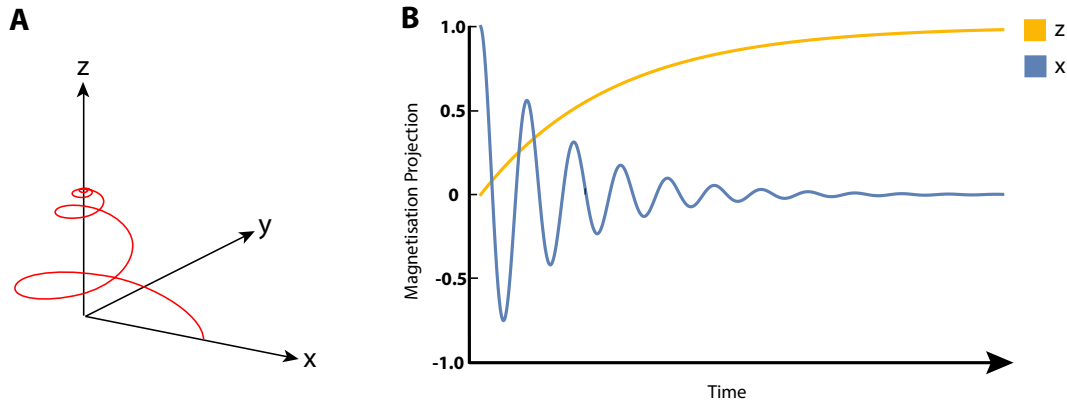


FIGURE 1.5: A) a magnetisation vector precesses in the xy -plane, eventually returning to equilibrium. B) A plot of the magnetisation along z -axis (yellow) and the x -axis (blue) during the relaxation.

oscillate near the larmour frequency of the relaxing spin. These oscillating fields can be thought of as local RF pulses we discussed earlier, the key difference is that they only affect a few spins and not the sample as a whole. Essentially relaxation is an energy exchange between the spins and the molecules surrounding them. This is the origin of the original name for longitudinal relaxation - spin-lattice relaxation.

1.2.2 Quantum description of NMR

In this chapter, I will introduce the the quantum description of NMR. Including how we use operators and superoperators to understand how states change under different conditons and how the energies of the system can be extracted.

1.2.2.1 Nuclear Spin

Nuclear spin can be treated as a type of angular momentum. Spin angular momentum can be characterized by its total angular momentum, and the angular momentum with respect to a reference axis (usually z). Denoted by \hat{I} it is comprised of a magnitude, $|\hat{I}|$, and a direction, m_I . The magnitude is given by

$$|\hat{I}| = \hbar\sqrt{I(I+1)} \quad (1.37)$$

where \hbar is the reduced Planck constant and $I = 0, \frac{1}{2}, 1, \dots$. The projection of \hat{I} in the z direction, \hat{I}_z , is given by

$$\hat{I}_z = m_I \hbar \quad (1.38)$$

m_I can take integer values from $-I$ to $+I$ shown in Fig. 1.6

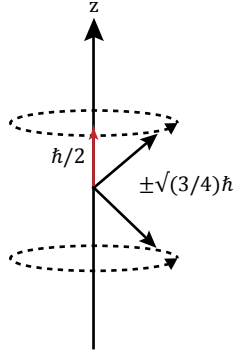


FIGURE 1.6: The projection of two states in a spin 1/2 nucleus (red arrow) with the magnitudes indicated (black arrow)

For the commonly occurring case of a spin-1/2 nucleus, $I = 1/2$ and $m_I = \pm 1/2$ and if we were to measure \hat{I}_z we would get a value of with an associated probability depending which state the system is in. Indicating the possible measurement outcomes for \hat{I}_z are $\pm \frac{\hbar}{2}$.

1.2.2.2 Spin States

If a spin-1/2 nucleus is placed in a magnetic field (taken to be oriented along z) it can be represented using two basis states. State one has $I = 1/2$, $m_I = 1/2$ and State two has $I = 1/2$, $m_I = -1/2$. We denote these as $|I, m_I\rangle$ [11], for simplicity we omit the I and are left with $|m_I\rangle$. For the special case of a spin-1/2 the two states are known as zeeman states denoted by $|\alpha\rangle$ and $|\beta\rangle$. Where the $|\alpha\rangle$ state has angular momentum +1/2 and $|\beta\rangle$ has -1/2.

The zeeman states take the following form:

$$|\alpha\rangle = \begin{pmatrix} 1 \\ 0 \end{pmatrix} \quad |\beta\rangle = \begin{pmatrix} 0 \\ 1 \end{pmatrix} \quad (1.39)$$

bras are also defined by taking the conjugate transpose of the ket, $|\alpha\rangle^\dagger = \langle\alpha|$ such that

$$\langle\alpha| = (1 \ 0) \quad \langle\beta| = (0 \ 1) \quad (1.40)$$

The state, $|\psi\rangle$, of a two level system can now be completely described in this basis as the linear combination of the basis states:

$$|\psi\rangle = c_1 |\alpha\rangle + c_2 |\beta\rangle = \begin{pmatrix} c_1 \\ c_2 \end{pmatrix} \quad (1.41)$$

$$\langle \psi | = c_1^* |\alpha\rangle + c_2^* |\beta\rangle = \begin{pmatrix} c_1^* & c_2^* \end{pmatrix} \quad (1.42)$$

These are normalised such that $c_1 c_1^* + c_2 c_2^* = 1$.

To complete the picture the states must be orthonormal. Orthonormality between states exists if the inner product of the basis states $|r_i\rangle$ and $|r_j\rangle$ satisfies the following conditions:

$$\langle r_i | r_j \rangle = \delta_{ij} \quad (1.43)$$

where the Kronecker delta is:

$$\delta_{ij} = \begin{cases} 0 & \text{if } i \neq j \\ 1 & \text{if } i = j \end{cases} \quad (1.44)$$

where $\langle r_i | r_j \rangle = \delta_{ij}$ denotes taking the dot product between the two vectors $|r_i\rangle$ and $|r_j\rangle$.

The basis states help to quantify the component of a state vector along that state. Take our example from Eqn. 1.41, we can construct inner products of the overall state, $|\psi\rangle$ with $|\alpha\rangle$ and $|\beta\rangle$ to determine component of the basis states.

$$\langle \alpha | \psi \rangle = c_1 \quad \langle \beta | \psi \rangle = c_2 \quad (1.45)$$

The outer product of the basis state, $|r_n\rangle$, for an N-spin system must satisfy:

$$\sum_{n=1}^N |r_n\rangle \langle r_n| = \mathbb{1} \quad (1.46)$$

where $\mathbb{1}$ is an N by N identity matrix.

When a second spin is introduced, the Hilbert space is extended to accommodate additional spin states by taking the tensor product of the basis states

$$|\alpha_1 \alpha_2\rangle = |\alpha_1\rangle \otimes |\alpha_2\rangle = \begin{pmatrix} 1 \\ 0 \\ 0 \\ 0 \end{pmatrix} \quad |\alpha_1 \beta_2\rangle = |\alpha_1\rangle \otimes |\beta_2\rangle = \begin{pmatrix} 0 \\ 1 \\ 0 \\ 0 \end{pmatrix} \quad (1.47)$$

$$|\beta_1 \alpha_2\rangle = |\beta_1\rangle \otimes |\alpha_2\rangle = \begin{pmatrix} 0 \\ 0 \\ 1 \\ 0 \end{pmatrix} \quad |\beta_1 \beta_2\rangle = |\beta_1\rangle \otimes |\beta_2\rangle = \begin{pmatrix} 0 \\ 0 \\ 0 \\ 1 \end{pmatrix} \quad (1.48)$$

The subscripts indicate which spin we are referring to, e.g. $|\beta_1\alpha_2\rangle$ means that spin 1 is in the β state and spin 2 is in the α state.

1.2.2.3 Operators

Operators act on states. To explain this, let's consider a generic operator \hat{B} with eigenstates $|\alpha\rangle$ and $|\beta\rangle$. When a state is acted upon by an operator it is denoted by:

$$\hat{B}|\alpha\rangle = b|\alpha\rangle \quad (1.49)$$

the same state is returned, multiplied by some scalar b , that is an eigenvalue of $|\alpha\rangle$ in the operator basis B.

The expectation value of an operator can be found by:

$$\langle \hat{B} \rangle = \langle \alpha | \hat{B} | \alpha \rangle = b \langle \alpha | \alpha \rangle = b \quad (1.50)$$

this returns the eigenvalue.

In NMR we use three operators to determine the projection of angular momentum along a specific axis, \hat{I}_x , \hat{I}_y , and \hat{I}_z . These are defined by the Pauli matrices multiplied by $\frac{\hbar}{2}$.

$$\hat{I}_x = \frac{\hbar}{2} \begin{pmatrix} 0 & 1 \\ 1 & 0 \end{pmatrix} \quad \hat{I}_y = \frac{\hbar}{2i} \begin{pmatrix} 0 & 1 \\ -1 & 0 \end{pmatrix} \quad \hat{I}_z = \frac{\hbar}{2} \begin{pmatrix} 1 & 0 \\ 0 & 1 \end{pmatrix} \quad (1.51)$$

as an example, let's take the example from before of a spin-1/2 particle in a magnetic field and see what happens if we were to project the $|\alpha\rangle$ state along the z-axis.

$$\hat{I}_z |\alpha\rangle = \frac{\hbar}{2} \begin{pmatrix} 0 & 1 \\ 1 & 0 \end{pmatrix} \begin{pmatrix} 1 \\ 0 \end{pmatrix} = \frac{\hbar}{2} \begin{pmatrix} 1 \\ 0 \end{pmatrix} = \frac{\hbar}{2} |\alpha\rangle \quad (1.52)$$

We find that $\frac{\hbar}{2}$ is the eigenvalue of $|\alpha\rangle$ for the operator \hat{I}_z . For ease of handling in the following examples we will take $\hbar = 1$.

We will now examine three more operators and explore how they act on states. They are the total square angular momentum, \hat{I}^2 and the two shift operators \hat{I}^+ and \hat{I}^- defined as the following:

$$\hat{I}^2 = \hat{I}_x^2 + \hat{I}_y^2 + \hat{I}_z^2 \quad (1.53)$$

$$\hat{I}^+ = \hat{I}_x + i\hat{I}_y \quad (1.54)$$

$$\hat{I}^- = \hat{I}_x - i\hat{I}_y \quad (1.55)$$

They act on states according to:

$$\hat{I}^2 |I, m_I\rangle = I(I+1) |I, m_I\rangle \quad (1.56)$$

$$\hat{I}^+ |I, m_I\rangle = \sqrt{(I(I+1) - m_I(m_I+1))} |I, m_{I+1}\rangle \quad (1.57)$$

$$\hat{I}^- |I, m_I\rangle = \sqrt{(I(I+1) - m_I(m_I-1))} |I, m_{I-1}\rangle \quad (1.58)$$

Using a spin-1/2 particle in a magnetic field as an example we'll let these operators act on the $|\alpha\rangle$ state

$$\hat{I}^2 |\alpha\rangle = \frac{3}{4} |\alpha\rangle \quad (1.59)$$

$$\hat{I}^+ |\alpha\rangle = 0 \quad (1.60)$$

$$\hat{I}^- |\alpha\rangle = |\beta\rangle \quad (1.61)$$

$$\hat{I}^+ |\beta\rangle = |\alpha\rangle \quad (1.62)$$

$$\hat{I}^- |\beta\rangle = 0 \quad (1.63)$$

As the '+' and '-' denote raising or lowering m_I by 1

We can see if two operators commute by using the commutator which is defined as:

$$[\hat{A}, \hat{B}] = \hat{A}\hat{B} - \hat{B}\hat{A} \quad (1.64)$$

If $[\hat{A}, \hat{B}] = 0$ the operators are said to commute. The \hat{I}_x , \hat{I}_y and \hat{I}_z have cyclic commutation rules:

$$[\hat{I}_x, \hat{I}_y] = i\hat{I}_z \quad (1.65)$$

$$[\hat{I}_y, \hat{I}_z] = i\hat{I}_x \quad (1.66)$$

$$[\hat{I}_x, \hat{I}_z] = i\hat{I}_y \quad (1.67)$$

These relationships are important in NMR as they help govern the rules for the rotations of spins.

1.2.2.4 Superoperators

Like states, that can be transformed by operators, we can define objects that act in a similar manner on operators. These objects are called superoperators.

To start, let's take a simple commutation superoperator, $\hat{\hat{A}}$, defined as:

$$\hat{\hat{A}}\hat{B} = [\hat{A}, \hat{B}] = \hat{A}\hat{B} - \hat{B}\hat{A} \quad (1.68)$$

Applying it to operator \hat{B} results in the commutation of \hat{A} and \hat{B}

In NMR, three rotational superoperators can be defined using the commutation super-operators from Eqn. 1.52:

$$\hat{R}_x(\theta) = \exp\{-i\hat{I}_x\theta\} \quad \hat{R}_y(\theta) = \exp\{-i\hat{I}_y\theta\} \quad \hat{R}_z(\theta) = \exp\{-i\hat{I}_z\theta\} \quad (1.69)$$

These are applied to the angular momentum operators using the sandwich formula:

$$\hat{R}_x(\theta)\hat{I}_z = \exp\{-i\hat{I}_x\theta\}\hat{I}_z\exp\{+i\hat{I}_x\theta\} \quad (1.70)$$

The result of this is a rotation of \hat{I}_z around the x -axis by an angle θ :

$$\hat{R}_x(\theta)\hat{I}_z = \cos\theta\hat{I}_z - \sin\theta\hat{I}_y \quad (1.71)$$

The rotational direction (sign of the $\sin\theta$ term) is determined by the right hand coordinate system defined in Eqn. 1.65.

We will now discuss how these are used in describing the spin dynamics of a spin system.

1.2.2.5 Density Operator

The density operator gives us information on the state of groups of spins in a spin system.

Let's go back once again to a spin-1/2 particle in a magnetic field. Where $|\psi\rangle$ is some superposition state in the two level system such that:

$$|\psi\rangle = \begin{pmatrix} c_1 \\ c_2 \end{pmatrix} = c_1 |\alpha\rangle + c_2 |\beta\rangle \quad (1.72)$$

$$\langle\psi| = \begin{pmatrix} c_1^* & c_2^* \end{pmatrix} = c_1^* \langle\alpha| + c_2^* \langle\beta| \quad (1.73)$$

The density operator has the form:

$$\hat{\rho} = \overline{|\psi\rangle\langle\psi|} = \begin{pmatrix} c_1c_1^* & c_1c_2^* \\ c_2c_1^* & c_2c_2^* \end{pmatrix} \quad (1.74)$$

If the number of spins is increased, the density operator's form does not change instead it provides an average for the entire group of spin states. The population of a given state is given by the expectation value of the density operator as in Eqn. 1.50. If we would like to know the population of state $|\alpha\rangle$ we would perform the following:

$$\langle\alpha|\hat{\rho}|\alpha\rangle = \langle\alpha|\psi\rangle\langle\alpha|\psi\rangle = c_1^*c_1 \quad (1.75)$$

The diagonal elements of $\hat{\rho}$ are state populations or the probabilities of being in a certain state.

The off-diagonal elements are coherences between states. These coherences are complex numbers and two coherences between the same pair of states are complex conjugates of each other. e.g.:

$$\langle \alpha | \hat{\rho} | \beta \rangle = (\langle \beta | \hat{\rho} | \alpha \rangle)^* = c_1 c_2^* = (c_1^* c_2)^* \quad (1.76)$$

The coherence order between two states in a magnetic field is defined as the difference in angular momentum projection along the z axis. In our two spin this would be (with $\hbar = 1$):

$$\hat{I}_z |\beta\rangle = m_\alpha = +\frac{1}{2} |\alpha\rangle \quad (1.77)$$

$$\hat{I}_z |\beta\rangle = m_\beta = -\frac{1}{2} |\beta\rangle \quad (1.78)$$

We can use these results to calculate the coherence order of the coherence $\langle \alpha | \hat{\rho} | \beta \rangle$:

$$m_\alpha - m_\beta = +1 \quad (1.79)$$

and conversely the coherence order of $\langle \beta | \hat{\rho} | \alpha \rangle$ is:

$$m_\beta - m_\alpha = -1 \quad (1.80)$$

Now let's look at how $\hat{\rho}$ relates to the angular momentum operators give in Eqn. 1.52.

Usually in NMR there are $> 10^{20}$ spins in the sample, the density operator becomes more advantageous here as mentioned it contains information about the entire spin ensemble. Normally, there is only a small population difference between α and β (see 1.2.1.2), but for this example let's imagine we have found a sufficiently strong enough field for a population difference of 0.1. The density operator in this case would be:

$$\hat{\rho} = \frac{1}{2} \begin{pmatrix} 1 + 0.1 & 0 \\ 0 & 1 - 0.1 \end{pmatrix} \quad (1.81)$$

using the definition given in Eqn. 1.52 we can re-write this as

$$\hat{\rho} = \frac{1}{2} \hat{1} + 0.1 \hat{I}_z \quad (1.82)$$

$\hat{1}$ is identity matrix and corresponds to no population difference between $|\alpha\rangle$ and $|\beta\rangle$.

$\hat{1}$ is unaffected by rotations so can be ignored in the context of NMR and so we write

$$\hat{\rho} = 0.1 \hat{I}_z \quad (1.83)$$

to describe the z magnetisation of our sample.

The density operator can also be used to describe the evolution of a spin system under operations. If we applied a 90 degree pulse along the y axis, denoted using radians by $(\pi/2)_y$. That is the equivalent of propagating the initial density operator, ρ_0 under the rotation superoperator $\hat{R}_y(\pi/2)$:

$$\hat{\rho}_1 = \hat{R}_y\left(\frac{\pi}{2}\right)\hat{\rho}_0 = \exp\left\{-i\left(\frac{\pi}{2}\right)\hat{I}_y\right\}\hat{I}_z\exp\left\{+i\left(\frac{\pi}{2}\right)\hat{I}_y\right\} = \hat{I}_x \quad (1.84)$$

Now the magnetisation is in the x -axis it will begin to precess about the z -axis which using our notation is the equivalent of propagating \hat{I}_x ($\hat{\rho}_1$) under $\hat{R}_z(\omega t)$:

$$\hat{\rho}_2 = \hat{R}_z(\omega t)\hat{\rho}_1 = \exp\left\{-i\omega t\hat{I}_z\right\}\hat{I}_x\exp\left\{+i\omega t\hat{I}_z\right\} \quad (1.85)$$

$$= \cos(\omega t)\hat{I}_x + \sin(\omega t)\hat{I}_y \quad (1.86)$$

where ω is the larmour frequency, and t is time.

the $\exp\{i\omega t\}$ is called a propagator, because it propagates the density operator in time.

The Hamiltonian, the energy operator, describes how the system evolves in time and uses progators, rotational superoperators and the density operator in order to do so.

1.2.2.6 The Hamiltonian

As mentioned the Hamiltonian is the energy operator. It provides information on the enrgies of states in a system.

If we let $|\psi_1\rangle$ and $|\psi_2\rangle$ be eigenstates of the Hamiltonian \hat{H} then

$$\hat{H}|\psi_1\rangle = E_1|\psi_1\rangle \quad (1.87)$$

$$\hat{H}|\psi_2\rangle = E_2|\psi_2\rangle \quad (1.88)$$

The Hamiltonian can also be expressed in matrix form:

$$\hat{H} = \begin{pmatrix} E_1 & 0 \\ 0 & E_2 \end{pmatrix} \quad (1.89)$$

If the Hamiltonian is written in the eigenbasis of the system its main diagonal correspond to state energies and it has values of 0 everywhere else.

The evolution in time of a quantum system is described by the Schrödinger equation:

$$i\hbar\frac{\partial}{\partial t}|\psi\rangle = \hat{H}|\psi\rangle \quad (1.90)$$

The \hbar was included for completeness sake and will again be set to equal 1.

In NMR we describe the dynamics of a system using the density operator evolution rather than the evolution of the states using

$$\frac{\partial}{\partial t} |\psi\rangle = -i\hat{H} |\psi\rangle \quad (1.91)$$

$$\frac{\partial}{\partial t} \langle\psi| = i \langle\psi| \hat{H} \quad (1.92)$$

we can derive[12]:

$$\frac{\partial}{\partial t} \hat{\rho} = \frac{\partial}{\partial t} [|\psi\rangle \langle\psi|] \quad (1.93)$$

$$= \left[\frac{\partial}{\partial t} |\psi\rangle \right] \langle\psi| + |\psi\rangle \left[\frac{\partial}{\partial t} \langle\psi| \right] \quad (1.94)$$

$$= -i\hat{H} |\psi\rangle \langle\psi| + i |\psi\rangle \langle\psi| \quad (1.95)$$

to give the relationship

$$\frac{\partial}{\partial t} \hat{\rho} = -i[\hat{H}, \hat{\rho}] \quad (1.96)$$

this is called the Louisville von Neumann equation.

Returning to our spin-1/2 particle in a magnetic field. The Hamiltonian is initially proportional to the z angular momentum operator

$$\hat{H} = \omega \hat{I}_z \quad (1.97)$$

where $\omega = -\gamma B_0$. In matrix form, in our original zeeman basis, the Hamiltonian is:

$$\hat{H} = \begin{pmatrix} +\frac{\omega}{2} & 0 \\ 0 & -\frac{\omega}{2} \end{pmatrix} \quad (1.98)$$

where

$$\hat{H} |\alpha\rangle = +\frac{\omega}{2} |\alpha\rangle \quad (1.99)$$

The density operator evolves under a Hamiltonian like so:

$$\hat{\rho}(t) = \exp\{-i\hat{H}t\} \hat{\rho}(0) \exp\{+i\hat{H}t\} \quad (1.100)$$

In Eqn. 1.85, we saw that the precession of a spin-1/2 particle in a magnetic field can be described using the rotation superoperator around the z -axis $\hat{R}_z(\omega t)$. We know that for this system its analagous to $\hat{H} = \omega \hat{I}_4$.

If the density operator commutes with the Hamiltonian there is no evolution of the system this can be seen more clearly using propagators with $\hat{H} = \omega \hat{I}_z$ and $\rho(0) = \hat{I}_z$

$$\rho(t) = \exp\{-i\omega t \hat{I}_z\} \hat{I}_z \exp\{+i\omega t \hat{I}_z\} = \hat{I}_z \quad (1.101)$$

If the density operator does not commute with the Hamiltonian it will evolve. To demonstrate this we use $\hat{H} = \omega \hat{I}_z$ as before however this time $\hat{\rho}(0) = \hat{I}_x$

$$\hat{\rho}(t) = \exp\{-i\omega t \hat{I}_z\} \hat{I}_x \exp\{+i\omega t \hat{I}_z\} = \cos(\omega t) \hat{I}_x + \sin(\omega t) \hat{I}_y \quad (1.102)$$

The Hamiltonian for multi-spin system is slightly more complicated. Consider a two spin system I_1 and I_2 with J -coupling J_{12} the Hamiltonian then becomes:

$$\hat{H} = \omega_1 \hat{I}_1 + \omega_2 \hat{I}_2 + 2\pi J_{12} \hat{\mathbf{I}}_1 \cdot \hat{\mathbf{I}}_2 \quad (1.103)$$

where $\hat{\mathbf{I}}_1 \cdot \hat{\mathbf{I}}_2 = \hat{I}_{1x}\hat{I}_{2x} + \hat{I}_{1y}\hat{I}_{2y} + \hat{I}_{1z}\hat{I}_{2z}$. In matrix form in the zeeman basis this is:

$$\hat{H} = \frac{1}{2} \begin{pmatrix} +\omega_1 + \omega_2 + \pi J_{12} & 0 & 0 & 0 \\ 0 & +\omega_1 - \omega_2 - \pi J_{12} & 2\pi J_{12} & 0 \\ 0 & 2\pi J_{12} & -\omega_1 + \omega_2 - \pi J_{12} & 0 \\ 0 & 0 & 0 & -\omega_1 - \omega_2 - \pi J_{12} \end{pmatrix} \quad (1.104)$$

The zeeman basis is no longer an eigenbasis of the Hamiltonian because the J -coupling introduces off-diagonal terms. In practice, when $|\omega_1 - \omega_2| \gg 2\pi J_{12}$ these terms are ignored because the zeeman basis is approximately the eigen basis of the Hamiltonian. This is termed the secular approximation.

However, when this is not the case, the Hamiltonian requires diagonalisation which is beyond the scope of this introduction but will be addressed if needed in later chapters.

1.3 Micro-NMR

All NMR experiments depend on two performance metrics: sensitivity and resolution. Sensitivity here means the minimum number of spins needed to give a signal clearly above the noise. Resolution quantifies how well different spins in the sample can be differentiated. These two properties are often linked, by selecting a smaller sample it is possible to enhance resolution by detecting a smaller portion of spins in the sample but this compromises sensitivity as the number of spins become more limited.

In NMR, the long life time of the nuclear spin states (minutes in some cases) contribute to extremely narrow lines in the spectrum with resolutions of one part per billion regularly achieved in commercial systems.

1.3.1 Sensitivity

1.3.1.1 Signal to noise ratio

Sensitivity in NMR at thermal equilibrium is always in short supply. In an NMR experiment the signal is proportional to the net magnetisation, M_0 , of the sample[13]:

$$M_0 = \frac{\gamma h}{4\pi} (I(I+1))(P_\alpha - P_\beta) = N\gamma^2 \hbar^2 I(I+1) \frac{B_0}{3k_B T} \quad (1.105)$$

where γ is the gyromagnetic ratio of the nucleus, \hbar is Plankc's constant $h/2$, $P_\alpha - P_\beta$ is the population difference between zeeman energy levels seen in 1.2.1.2, B_0 is the magnetic field, N is the number of spins per unit volume, k_B is the Boltzmann constant and T is the absolute temperature. The magnetisation and therefore signal depends on the population difference which at room temperature is on the order of 10^{-25}J which is much lower than the thermal energy of the system. From the equation, increasing B_0 would seem a valid strategy and comparatively it can be, increasing from 14.1T to 23.5T can almost double the signal, however even at 23.5T there is only a factor of 6×10^{-6} in population difference. It's this very small value that is responsible for the low sensitivity of NMR compared to other techniques.

Detection in NMR is typically done through the induction of a voltage in a coil that's close to the precessing nuclear spins this is usually referred to as the sample coil. Unfortunately, this coil also brings with it a type of interference, noise, analogous to the 'hiss' in the background of radio it is produced mainly from thermal motion of electrons in the sample coil with some contribution from thermal motion of ions in solution. The signal to noise ratio, SNR, is an important factor in NMR experiments if its too low the signal will never be seen.

The SNR was formulated by Abragam[14] and the analysis extended by Hoult and Richards[15] and is defined as the peak signal divided by the root mean square (rms) noise including the magnetisation from Eqn. 1.105 we find[16]:

$$\text{SNR} = \frac{k_0 \frac{B_1}{i} V_s \omega_0 \frac{1}{\sqrt{2}} M}{F \sqrt{4k_B T R_{\text{noise}}} \Delta f} \quad (1.106)$$

where k_0 is a contant that accounts for spatial inhomogeneities in the B_1 field, V_s is the sample volume, ω_0 is the larmour frequency, the factor $\frac{1}{\sqrt{2}}$ is introduced as the noise is rms noise. The factor B_1/i the magnetic field from the coil per unit current is defined as the coil sensitivity. The denominator is the noise determined by the noise factor from the spectrometer (F) and the dissipative loses (R_{noise}) of the coil, circuit and sample for the spectral bandwidth Δf . T is the absolute temperature and k_b is the boltzmann constant.

In the same paper, Hoult and Richards introduced the principle of reciprocity for calculating the sensitivity of the RF coil. This states that the signal received from a sample by a coil is proportional to the magnetic field which would have been created in the sample if unit current were passed through the coil. Therefore the SNR is directly proportional to the sensitivity of the coil, B_1/i . This can be seen if we define an effective sample volume $V'_s = k_0 V_s$ that is the volume in which B_1 is within 10% of the maximum value at the center of the coil. The SNR is given by a more simple expression[16]:

$$SNR = C \frac{B_1 N_s}{i \sqrt{R \Delta f}} \quad (1.107)$$

where N_s is the number of spins located within an effective volume V'_s . For protons at 600MHz the constant, C equals 1.4×10^{-11} in SI units ($B_0 = 14.1\text{T}$, $T = 300\text{K}$, $\gamma = 0.2675 \times 10^9 \text{ radT}^{-1}\text{s}^{-1}$, $I = 1/2$ and $F = 1$ assuming negligible noise from the spectrometer.)

From the simple expression it becomes clear that the way to improve SNR is to increase the filling factor (optimize the number of spins in the number of spins in B_1), maximise coil sensitivity, B_1/i , and minimise the total resistance. The filling factor, α_F is given by:

$$\alpha_F = \frac{\int B_1^2 \rho(r) dV}{\int B_1^2 dV} \quad (1.108)$$

where the function ρ is unity in the sample area, and zero elsewhere. For a long solenoid coil with the interior space filled with sample, $\alpha_F = 1/2$. Most other designs have a lower filling factor.

Two of these three can be solved by decreasing the size of the detector. The third, minimising resistance can be tackled by commercially available cryoprobes where the coil is cooled with a stream of He gas to 20K this reduces the thermal noise from the source and can increase SNR by a factor of four.

To see how size of coil affects SNR we take an RF helical coil. An idealised coil is a cylindrical shell with uniform current density. The RF current penetrates to a frequency specific depth δ . For copper at 600 MHz and room temperature $\delta = 2.7 \mu\text{m}$. The center field is given by:

$$\frac{B_1}{i} = \frac{\mu_0}{\sqrt{l^2 + d^2}} \quad (1.109)$$

Resistance is:

$$R = \rho \frac{\pi d}{l \delta} \quad (1.110)$$

with l , the height of the copper cylinder, d the diameter and ρ the resistivity. Optimum coil sensitivity is given by $d/l = 1$ in this case the signal to noise is:

$$SNR = 0.9 \times 10^{-16} \frac{N_s}{d \sqrt{\delta f}} \quad (1.111)$$

For a fixed number of spins the SNR scales with $1/d$ as predicted by [15]

1.3.2 Limit of Detection

The signal to noise ratio can be found in the time or frequency domain. In the time domain the noise, N , is $\sqrt{\Delta f}$. Therefore the SNR in the time domain is not a good measure of sensitivity, it can be artificially inflated by narrowing the bandwidth. Instead it is better to use *limit of detection*, defined as the number of spins that have to resonate within a bandwidth of 1 Hz to give an SNR of 3. This gives the normalised limit of detection as[2]:

$$\text{nLOD}_t = \frac{3n_s}{\text{SNR}_t \sqrt{\Delta f}} \quad (1.112)$$

Where n_s is the number of spins that were present in the sample for the measurement and SNR_t is the signal to noise ratio in the time domain. In the frequency domain, this becomes

$$\text{nLOD}_\omega = \frac{3n_s \sqrt{\Delta t}}{\text{SNR}_\omega} \quad (1.113)$$

here, Δt is the effective acquisition time for a single scan given by the inverse of the line broadening applied in the processing of the spectrum.

Practically, NMR relies on signal averaging see 3.2.2 to enhance the spectra, this method requires waiting between scans for the spins to reach thermal equilibrium. In this case the a better measure of sensitivity can be applied by using total measurement time as Δt . The drawback here, is that the limit of detection now depends on instrumentation and sample as T_1 relaxation dictates the experiment repetition rate.

1.3.3 Concentration limit of detection

Both types of LOD discussed so far are absolute measures. It is often of more interest to examine the *concentration* limit of detection cLOD. This is given by dividing the LOD by the sample volume:

$$\text{cLOD} = \frac{\text{nLOD}}{\alpha_f V_c} \quad (1.114)$$

Where V_c is the volume of the coil and α_f is the filling factor defined in Eqn. 1.108

One of the major reasons for development of micro-NMR has been the scaling of SNR and therefore LOD with coil size. The trade off here is that as the coil size, and LOD, becomes lower and lower, the volume shrinks too which leads to losses in cLOD. Micro-NMR therefore, only makes sense for mass or volume limited samples.

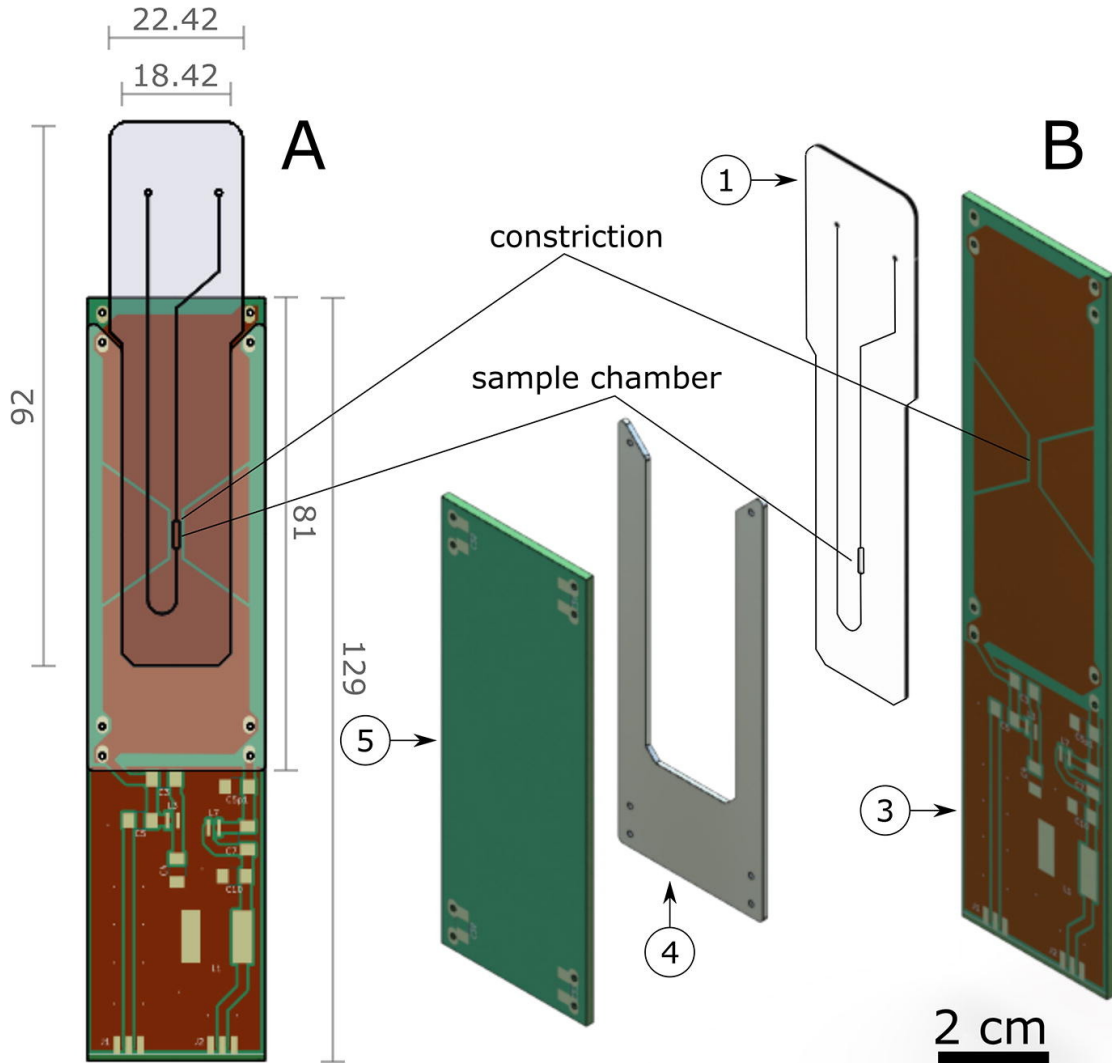


FIGURE 1.7: Drawings of the detector assembly and the microfluidic device (1). A: front view (dimensions in mm); B: exploded view. Spacer (4) ensures the alignment of the sample chamber with the constrictions on the PCB planes. In A, PCB plane 5 is hidden to show the orientation of 1 with respect to PCB plane 3. Thickness of each of the PCB planes is 1.52 mm and the copper layers on the PCBs is $35 \mu\text{m}$. Both the microfluidic device and the spacer are made from PMMA and have thickness of 0.9 mm and 1 mm respectively. Figure reproduced from [1]

1.3.4 Transmission line probe

This work employs the use of a planar transmission line probe(TLP)[17, 1], in which the geometry differs from that of a classic micro-coil. The design of which is based off early work by van Bentum *et al.* and for an equivalent helix gives $\sqrt{2}$ larger SNR[16]. The design of the TLP is shown in Fig. 1.7. It works with a generic microfluidic device that has well defined outer geometry and a fixed sample chamber position. The main advantage of using this probe is the compatibility of the device with customisable chips allowing a broad range of applications and enabling the marrying of practical NMR and some

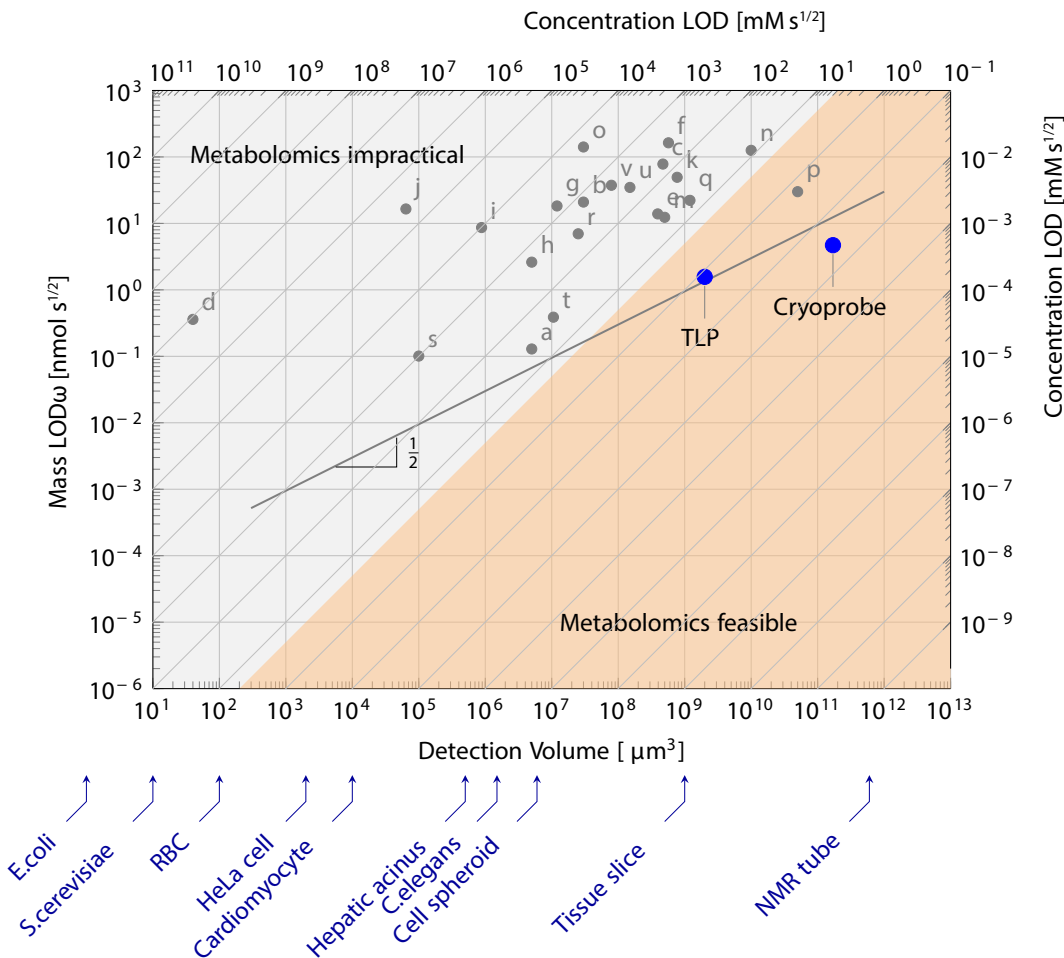


FIGURE 1.8: Plot comparing the limits of detection of previously design micro-NMR detectors. Letters a-t correspond to different authors as cited by Badilita *et al.*[2] Letters u[3] and t[4] represent more recent work. The probe used here is labelled at TLP and a commercial cyroprobe is shown for reference.

microfluidic capabilities which few others allow[4, 18, 19]. The limit of detection LOD for the TLP used is $1.4 \text{ nmol s}^{1/2}$ which comparitatively lower than detectors of a similar size and more similar to the LOD of commercial cryo-probes mentioned previously. Where the probe is exceptional in terms of micro-detector is the cLOD. Demonstrated in Fig. 1.8.

For this work, the goal is not only to combine NMR detection and microfluidics, clearly that has been done before. However, it is the combination of these two in a way that does not compromise in either. That, in an NMR sense, means nLODs comparable to macroprobes as well as sub 0.01 ppm line widths for true spectral resoltuion. This is displayed in Fig. 1.8, the area shaded orange that we define as the 'metabolomics feasible' range is a maximum $5 \text{ mM } \sqrt{s}$ ensuring species present at 0.1 mM can be detected within less than 20 mins to a sufficient resolution. The TLP has a cLOD of $1 \text{ mM } \sqrt{s}$ and can detect species at 0.02 mM in that time frame Whilst this is suitable for some metabolomic information to be gained, however, the subtle changes in molecules

present at less than 0.02 mM still evades us in the given time frame. Efforts towards lowering the nLOD and cLOD are described in [3](#)

Chapter 2

Microfluidic Droplet NMR

The majority of this chapter is work published in [20]

2.1 Abstract

In this chapter a system that enables high-resolution NMR spectroscopy of microfluidic droplet emulsions is discussed. Acquiring NMR spectra of emulsions is complicated by the magnetic susceptibility mismatches that occur between the phases. In order to overcome these challenges a 2-part solution is needed. Firstly, shim structures are cut into the microfluidic chip in order to match the PMMA with the continuous phase (cyclohexane). Secondly, an ideal concentration of chelated Eu³⁺ was doped into the dispersed phase (water) in order to match the susceptibility of the phases. High resolution spectra with linewidths of 3Hz were obtained in the ideal case. However, a serial dilution experiment that was used to obtain spectra of glucose droplets showed the highly sensitive dependence of linewidth on Eu concentration.

2.2 Introduction

Droplet microfluidics is the field of microfluidic research that separates samples into discreet droplets by introducing one immiscible fluid (dispersed fluid) into another (continuous fluid). In this way, samples can be manipulated freely in the lab-on-a-chip (LoC) system, and problems due to viscous dispersion and cross-contamination are avoided. In doing so, microdroplets of tuneable size and volume, typically femto- to nanolitres, are produced at rate reported to be up to 44 kHz [21]. Thorsen et al[22] reported one of the first droplet microfluidic devices. In the letter, they show how one can use microfluidic

channels to generate mono-disperse microemulsions by shearing water into a perpendicular flow of oil. By varying the ratio of the pressures driving the flow of each fluid they produce droplets that range in diameter from $10\text{ }\mu\text{m}$ to $60\text{ }\mu\text{m}$.

Droplets have since emerged as a versatile tool finding wide ranging applications in areas such as microcapsule synthesis[23], crystal growth[24], chemical reactions [25], cell/organism encapsulation [26, 27, 28], PCR[29, 30], and Protein studies[31, 32]. These applications are diverse owing to many advantages that microfluidic droplets possess: limited cross contamination; high production rates; large surface area to volume ratio; small reagent volumes; and independent control of each droplet[33].

Droplet generation can, broadly speaking, be divided into two categories. These are active and passive generation methods. Active methods are defined as applying additional force to the device to create droplets such as electric[34], magnetic[35] or centrifugal[36] or by modifying intrinsic forces by tuning fluid velocity[37]. Passive methods rely on the inherent instability of the liquid-liquid interface when mixing two immiscible fluid in order to generate droplets[38, 39, 40]. Zhu and wang[41] have published an in-depth review of the various methods of droplet generation as well as the equations that govern them.

In this work, active droplet generation was used in the form of fluid velocity variation. Two syringe pumps were employed that allowed separate manipulation of flow rates of the dispersed and continuous fluid. The dispersed and continuous phase are co-flowed to the the droplet generation point. By using this method, one can control the production rate and size of the droplets. Droplets of size $100\text{ }\mu\text{m}$ in diameter and a rate suitable enough to fill the sample chamber. If the flow is too fast the droplets have a very low residence time and there is never enough build up to perform an experiment. If, however, the flow is too slow the droplets that are formed are too big and inconsistent for any kind of reliable experimentation.

Nuclear magnetic resonance (NMR) as a spectroscopic technique has two chief advantages. It is non-invasive and non-destructive which makes it ideally placed to study living systems without destroying them. Indeed, NMR and magnetic resonance imaging (MRI) are both methods actively employed in metabolomics[42], drug discovery[43] and cancer imaging[44]. The nature of NMR means that one can glean quantitative, system level information in one experiment without the need for chemical tags. In a microfluidic context, where fluorescence[45, 46], or mass spec[47, 48], are often the methods of choice for spectroscopy NMR can be used in parallel to these and contribute to a better understanding of the system.

2.2.1 Susceptibility

Magnetic susceptibility, χ_V , is a measure of how much a material will become magnetized in an applied magnetic field. Given by the equation $\mathbf{M} = \chi_V \mathbf{H}$ where \mathbf{M} is the magnetisation of the material and \mathbf{H} is the magnetic field. In [5] a derivation of how the susceptibility can affect the magnetic field around a sample and influence its spectra.

In stationary conditions Ampere's law gives $\nabla \times \mathbf{H} = 0$ therefore the magnetic field \mathbf{H} can be expressed by scalar magnetic potential U as:

$$\mathbf{H} = -\nabla U \quad (2.1)$$

To describe an object being inserted into a magnetic field we split the potentials as $U = U_0 + U_d$, where $U_0 = H_0 z$ represents the original homogeneous field, and $\mathbf{H}_d = -\nabla U_d$ is the field generated by the magnetic dipoles induced in the inserted object (sometimes referred to as demagnetising field). The magnetic field H_0 , which we assume to be along the z-axis, arises from the superconducting coil

The macroscopic magnetic induction \mathbf{B} is given by:

$$\mathbf{B} = \mu_0(\mathbf{H} + \mathbf{M}) \quad (2.2)$$

where $\mu_0 = 4\pi \times 10^7 \text{ VsAm}^{-1}$ denotes vacuum permeability. With Gauss' law $\nabla \cdot \mathbf{B} = 0$ this becomes:

$$\nabla^2 U_d = \nabla \cdot \mathbf{M} \quad (2.3)$$

We assume the object that the object consists of a number of spatial domains characterised by a locally constant magnetic susceptibility χ_k . The magnetisation therefore, is a piecewise constant,

$$\mathbf{M}_k = \chi_k \mathbf{H}_k \mathbf{e}_z \quad (2.4)$$

the right hand side vanishes everywhere except at domain boundaries. The magnetic field satisfies the boundary conditions[49]

$$(\mathbf{H}_{d2} - \mathbf{H}_{d1}) \times \check{\mathbf{n}} = 0, \quad (2.5)$$

$$(\mathbf{H}_{d2} - \mathbf{H}_{d1}) \cdot \check{\mathbf{n}} = H_0(\chi_2 - \chi_1)\mathbf{e}_z \cdot \check{\mathbf{n}}, \quad (2.6)$$

where $\check{\mathbf{n}}$ denotes the surface normal from material 1 to material 2. Equations 2.3, 2.5 and 2.6 are formally solved by:

$$U_d(\mathbf{r}) = \frac{H_0}{4\pi} \int_{\delta_{12}} \frac{\check{\mathbf{n}} \cdot \mathbf{e}_z (\chi_2 - \chi_1)}{\sqrt{(\mathbf{r} - \mathbf{r}')^2}} dS, \quad (2.7)$$

where dS is an infinitesimal surface element, and \mathbf{r}' is the interaction variable. If there are more than two materials involved, as there are in droplets, each boundary gives an additive contribution of the same form.

The resonance frequency observed is proportional to the magnetic induction \mathbf{B}_{ext} experienced by chemically equivalent nuclei within each domain. This induction is determined by the outside field H_0 plus the induced magnetic dipoles of all molecules in the same domain except the one carrying the observed spin.[50] In liquids and isotropic solids, the external magnetic induction differs from the macroscopic \mathbf{B} as:

$$\mathbf{B}_{ext} - \mathbf{B} = \frac{2\mu_0\chi_s}{3}\mathbf{H}_0 \quad (2.8)$$

The magnetic induction relevant for the Larmour precession of nuclear spins in the sample is therefore

$$\mathbf{B}_{ext} = \mu_0 H_0 (1 + \frac{\chi_s}{3}) \mathbf{e}_z - \mu_0 \nabla U_d \quad (2.9)$$

Since χ is a piecewise constant, the $\mu_0 \nabla U_d$ term contributes to continuously varying fields and therefore any line broadening seen in the spectrum, whereas the $\mu_0 H_0 (1 + \frac{\chi_s}{3}) \mathbf{e}_z$ produces a bulk magnetic susceptibility shift (BMS) of the resonance line.

Broadly, this allows a classification of most materials as para- ($\chi > 0$) or dia- ($\chi < 0$) magnetic. Materials used in this work are listed in Table 2.1

2.2.2 Matching susceptibilities in emulsions

This usually isn't a problem in microfluidic NMR as usually the materials susceptibilities are matched in most of our experiments for example the solvent is water and the chip material is PMMA. However, when the susceptibilities are mismatched, as they are in droplets, this can cause inhomogeneities in the magnetic field, this shifts the resonances and broadens the lines in the spectra rendering them useless. For any kind of useful NMR, the magnetic field needs to be very homogeneous with most commercial superconducting magnets achieving homogeneities of a few parts per billion. Utz and co workers[5] have shown that susceptibility mismatches induced by the doping of Eu_3^+ into a solvent can be compensated for by installing shim structures that contain air around the NMR sensitive region, to produce an equal and opposite demagnetising field to the one caused by the solution, well resolved spectra can be taken of glucose dissolved in the mismatched liquid.

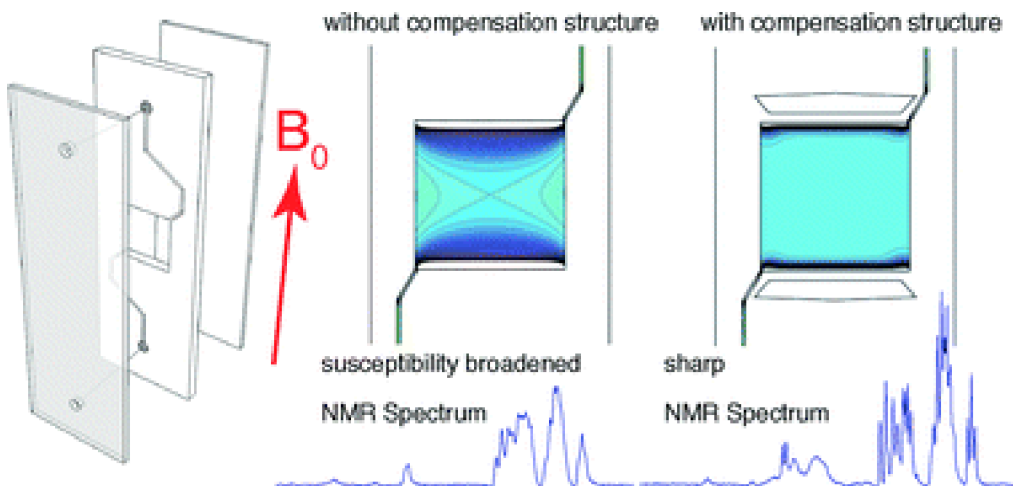


FIGURE 2.1: Summary graphic of the work in [5]. This shows how the NMR spectrum of glucose changes in a susceptibility mismatched chip but by cutting shimstructures around the sample chamberhigh resolution NMR is still possible despite the mismatches.

This work, combines both structural shimming and chelated lanthanide doping, to glean high resolution NMR spectroscopy from a microfluidic droplet emulsion. The system, made of a PMMA chip, aqueous dispersed phase and cyclohexane continuous phase. As mentioned the PMMA and water are susceptibility matched. The cyclohexane, however, is matched to neither. Hence, for all materials and solvents to be matched, structural shimming will be employed to match the PMMA to the cyclohexane and a chelated lanthanide $[\text{Eu}(\text{DTPA})]^{2-}$ will be used to match the water susceptibility.

In emulsions, susceptibility differences between the oil and aqueous phases lead to similar line broadening[51] NMR spectroscopy is extensively used to characterise emulsion droplet size distributions using pulsed field gradient methods[52, 53, 54, 55, 56, 57, 58]. These methods do not require spectral resolution of individual compounds other than the two solvents, and are therefore unaffected by the susceptibility broadening. By contrast, high-resolution NMR spectroscopy, with sufficient resolution to distinguish multiple compounds present in either of the two phases, requires careful mitigation of the susceptibility differences. It has also been shown that susceptibility differences can be compensated for in a liquid sample by doping of a chelated lanthanide[59] For example, Lennon *et al.* demonstrated that the susceptibility mismatch between the inside and outside of deoxygenated red blood cells could be compensated for by doping 3mM of dysprosium tripolyphosphate $[\text{Dy}(\text{PPP})_2]^{7-}$ into the extracellular fluid[60]

In this work, the possibility to obtain high-resolution NMR spectra from small volumes of droplet emulsions on a chip is explored. Integration of high-resolution NMR spectroscopy with microfluidic systems is challenging for a number of reasons. On the one hand, small sample volumes place stringent demands on detector sensitivity[2, 61] This has recently been addressed with the design of highly efficient planar NMR microcoils[62]

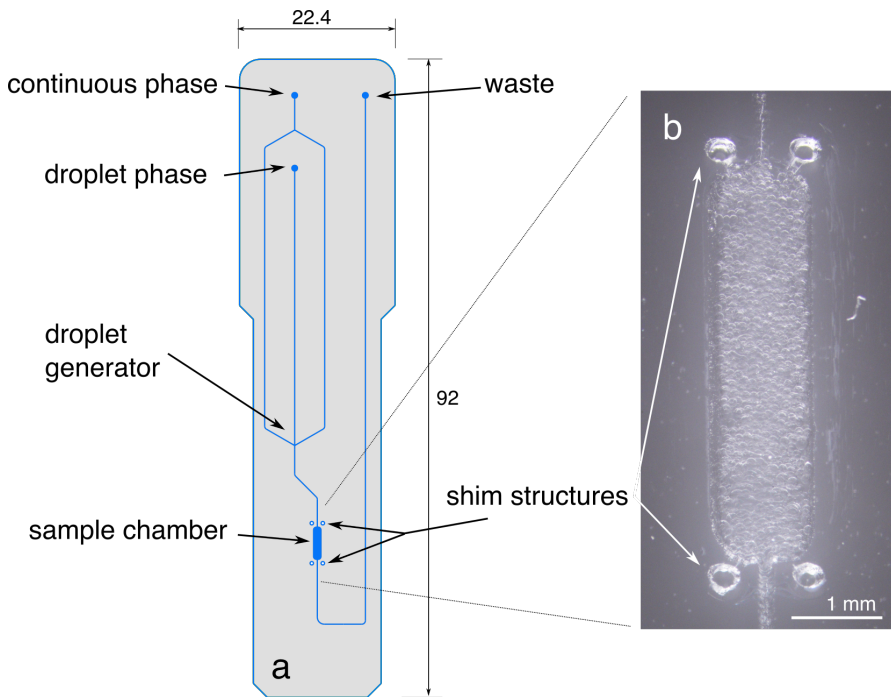


FIGURE 2.2: Droplet chip design (left) and detail micrograph of the sample chamber area filled with droplets (right). Some droplets are also visible in the entrance and exit channels.

and transmission line resonators[17] Another challenge is the preservation of high spectral resolution, which depends on a highly homogeneous magnetic field over the sample volume. Differences in magnetic susceptibility between the materials used for the microfluidic chip and the sample fluid, as well as the materials and geometry of the probe assembly, lead to a demagnetising field that varies continuously over the sample volume. Typical diamagnetic volume susceptibilities range from about -11 ppm to about -5 ppm (in SI units);[51, 63] differences of the order of several ppm are therefore commonplace. Unmanaged, they lead to broadening of NMR spectral lines over a ppm or more, which corresponds to a severe loss of resolution in ^1H liquid state NMR.

Managing susceptibility differences for an emulsion of droplets on a microfluidic chip adds additional complexity, since three different materials are now involved: the chip, the continuous phase, and the droplet phase, all with different susceptibilities. This can be mitigated in a two-step approach, which is based on the observation that most organic solvents in use as continuous phases for droplet microfluidics are less diamagnetic than water. First, the susceptibility difference between the chip and the continuous phase are compensated by shimming structures that are added to the chip design. Then, the susceptibility of the aqueous droplet phase is matched to that of the continuous phase by adding a paramagnetic solute.

It should be noted that in principle, the same effect could be achieved if a diamagnetic dopant could be added to the continuous phase. However, while paramagnetic dopants

TABLE 2.1: Bulk magnetic susceptibilities

Compound	$\chi_V/10^{-6}$ (SI)	Ref
water	-9.05	[65]
cyclohexane	-7.640	[65]
PMMA	-9.01	[66]
Air	+0.36	[67]

are easily available in the form of transition metal ions, no effective diamagnetic dopants exist in the literature.

Eu^{3+} complexes are paramagnetic, and are frequently used as shift agents in NMR spectroscopy. Unlike other lanthanide ions such as Gd^{3+} or Ho^{3+} , which are powerful nuclear relaxation agents, Eu^{3+} has only a minimal effect on nuclear magnetic relaxation due to its extremely short electron spin-lattice relaxation time[64] Addition of millimolar quantities of Eu^{3+} to aqueous solutions therefore does not cause significant relaxation line broadening, but changes the bulk magnetic susceptibility of the solution proportionally to the Eu^{3+} concentration. It is therefore possible to adjust the susceptibility difference in a droplet emulsion by adding a Eu^{3+} complex that selectively dissolves in (or at least strongly partitions to) the aqueous phase.

In the present work, the diethyl-triamine pentaacetate (DTPA) complex of Eu^{3+} , $\text{Eu}[\text{DTPA}]^{2-}$ is used. As an ion species, it is readily soluble in aqueous media, while exhibiting only negligible solubility in apolar organic solvents. Microfluidic chips are fabricated from poly methyl methacrylate (PMMA). By a fortunate coincidence, the susceptibilities of PMMA and water are very close to each other (Table 2.1). NMR lines in microfluidic devices made from PMMA are therefore narrow if aqueous samples are used, provided that the boundaries of the chip and the environment are either aligned with the external magnetic field, or are kept sufficiently remote from the detection area. By contrast, most organic solvents are considerably less diamagnetic than water, as exemplified by the case of cyclohexane, which has been used in the present study.

In the remainder of this chapter, finite element calculations (Should I add something about M. Utz performing these?) are used to estimate the NMR line widths expected in a droplet emulsion depending on the susceptibility mismatch. The results are then compared to experimental line widths obtained with varying concentrations of $\text{Eu}[\text{DTPA}]^{2-}$ in the aqueous phase. Finally, narrow NMR lines are obtained by combining structural shimming[68] with susceptibility matching, and demonstrate that this approach can be used to obtain a high resolution of glucose contained within the compensated droplets. The chip used in this work is shown in Fig. 2.2. It consists of a sample chamber in the centre of the chip, which is designed to line up with the sensitive area of a transmission-line micro-NMR detector,[17] and a convergent flow droplet generator. The aqueous phase and the continuous phase are fed into the two ports at the top. Droplets are

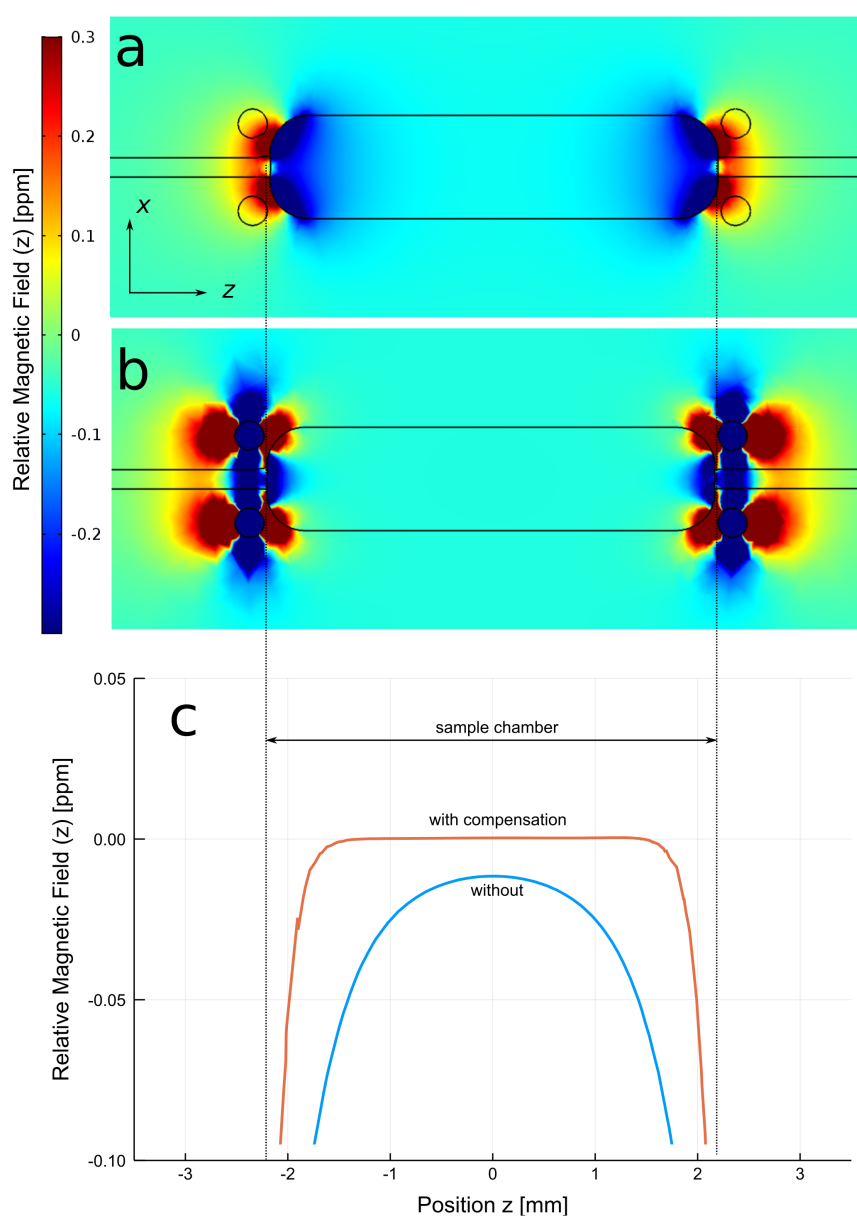


FIGURE 2.3: A: Finite element simulation of relative magnetic field distribution in an uncompensated chip (circular structures filled with PMMA) filled with cyclohexane and B: a compensated chip filled with cyclohexane; C: a linear plot of relative magnetic field along the z-axis through the middle of the sample chamber.

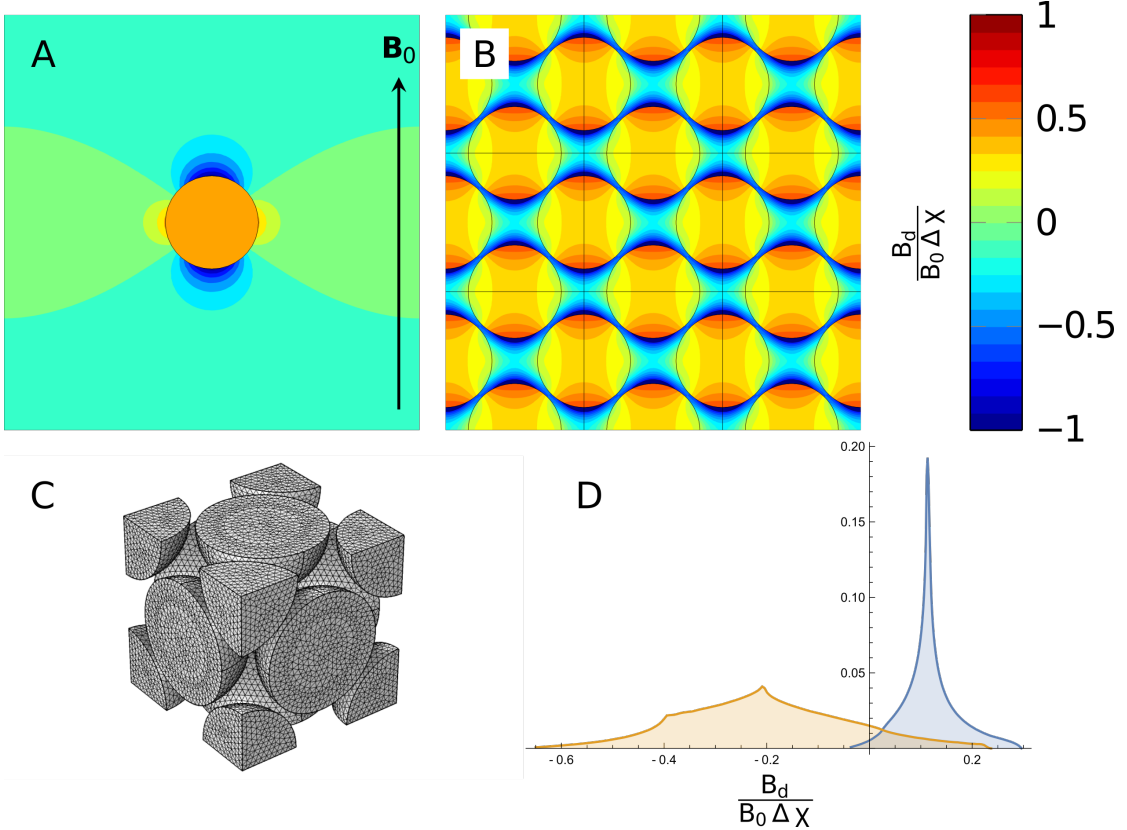


FIGURE 2.4: A: Finite element simulation of magnetic field distribution in droplets. z -component of the reduced magnetic field H_{red} in an isolated spherical droplet and B: in a face-centred cubic arrangement of droplets; C: FEM mesh used to calculate the result shown in B; D: histograms of the z -component of the reduced magnetic field in the continuous (orange) and in the droplet (blue) phase in the FCC arrangement.

formed and transported downstream into the sample chamber. The chamber is surrounded by four shim structures, which are circular shaped cutouts filled with air. They have been designed to compensate for the difference in susceptibility between the chip material (PMMA) and the oil phase (cyclohexane) as shown in Fig. 2.3. The operation of the chip is shown on the right side of Fig. 2.2; droplets of about $100 \mu\text{m}$ diameter are formed and fill the sample chamber.

2.3 Materials and Methods

Microfluidic chips of the design shown in Fig. 2.2 were fabricated from PMMA sheet material by laser cutting, and subsequent bonding of layers with a plasticiser under heat and pressure[69]. The chips consist of a top and bottom layer of $200 \mu\text{m}$ thickness each, and a middle layer of $500 \mu\text{m}$. Fluid channels upstream from the flow-focussing droplet generator were scored into the middle layer at low laser power to a depth of about $100 \mu\text{m}$. Downstream from the droplet generator, the channels and the sample chamber

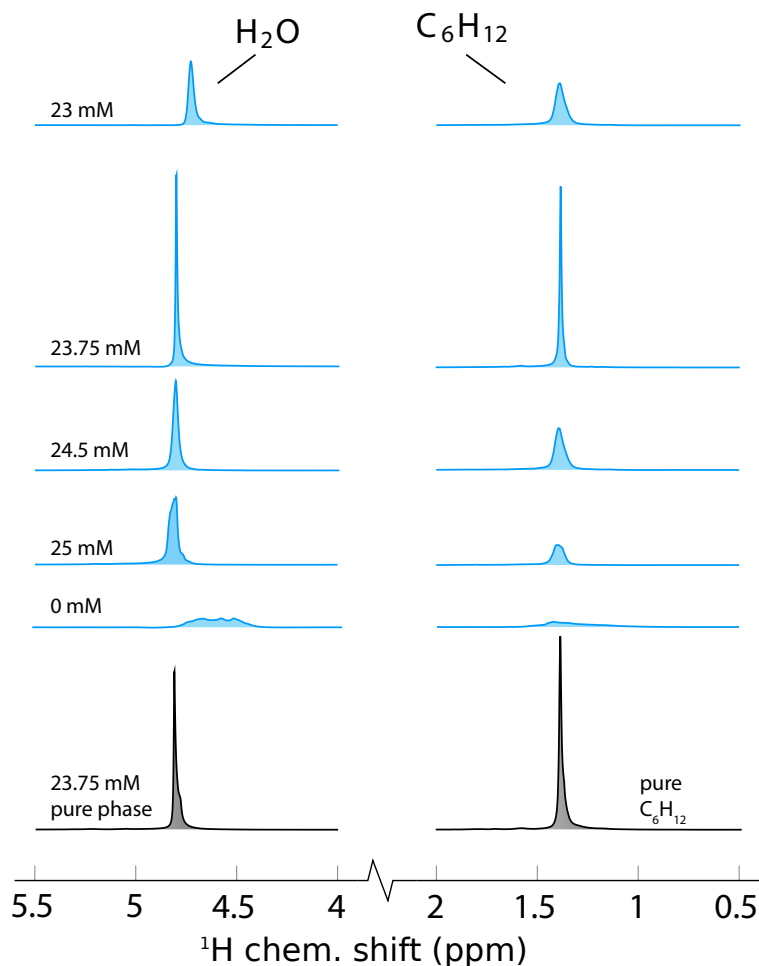


FIGURE 2.5: ^1H NMR line shapes of water (left) and cyclohexane (right) of a water in cyclohexane emulsion as a function of $\text{Eu}[\text{DTPA}]^{2-}$ concentration in the aqueous phase normalised to the sharpest peak. The spectra given in black are the pure phase spectra produced by the same chip.

were cut through the $500 \mu\text{m}$ middle layer by increased laser power, as were the shimming structures. The chips were connected to a pair of Cole-Palmer 200-CE syringe pumps for droplet generation. A flow rate of $20 \mu\text{l}/\text{min}$ was typically used for the continuous phase and $4 \mu\text{l}/\text{min}$ for the aqueous droplet phase. The continuous phase consisted of cyclohexane (Sigma-Aldrich) with 0.5% w/v of span-65 (sorbitan tristearate, Sigma-Aldrich) as a surfactant to ensure droplet stability. The cyclohexane/span solution was kept in a water bath at 30°C for at least 2h to ensure complete dissolution of the span. Prior to use, all solutions were left to equilibrate at a controlled room temperature of 25°C for at least 4h. Steady state conditions were ensured by letting the droplet generation run until the volume inside the chip had been exchanged at least five times. The chip was then disconnected from the syringe pumps, and the connection points sealed prior to insertion of the chip into the NMR probe.

NMR measurements were carried out on a Bruker AVANCE III spectrometer equipped

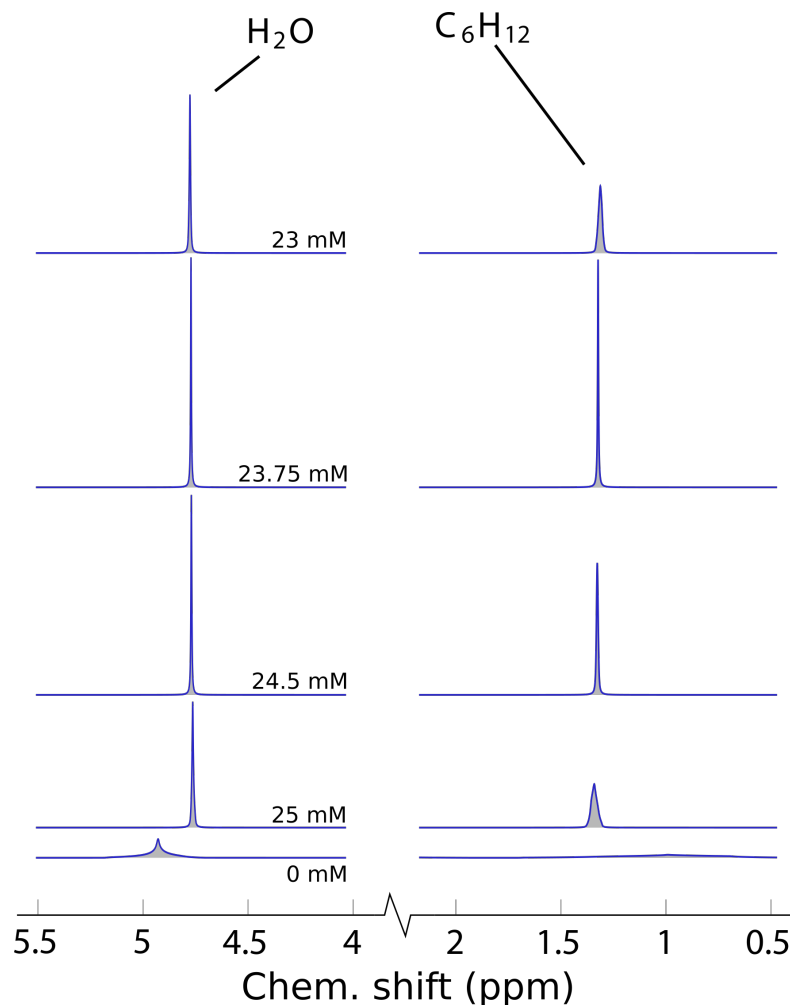


FIGURE 2.6: Predicted ^1H NMR line shapes of water (left) and cyclohexane (right) of a water in cyclohexane emulsion as a function of $\text{Eu}[\text{DTPA}]^{2-}$ concentration in the aqueous phase.

with an Oxford wide bore magnet operating at 7.05 Tesla, corresponding to a ^1H Larmor frequency of 300 MHz. A home-built NMR probe based on a transmission-line detector was used[17]. It accommodates microfluidic chips of the shape shown in Fig. 2.2. In the present work, the probe was doubly tuned to allow irradiation both at 300 MHz for ^1H and at 75 MHz for ^{13}C . Details of the electronic and mechanical design of the probe are given in Ref. [70].

NMR spectra were obtained at an RF nutation frequency of 66 kHz for ^1H , corresponding to 90 degree pulse length of 3.8 μs . Shimming of the sample was first performed on a sample of pure cyclohexane in an identical chip, these resulting values were used throughout all subsequent experiments with minor adjustments being made to linear shims (X,Y,Z) before each experiment to minimise line width. NMR spectra were acquired using Bruker spectrometer software (TopSpin 2.0), and were processed using

home-built scripts written in *Julia*.^[71] 20 mM of 4,4-Dimethyl-4-silapentane-1-sulfonic acid (DSS, Sigma Aldrich) was added to the aqueous phase as a chemical shift standard.

MRI gradient echo images of the sample chamber were obtained using ParaVision software and the fast low-angle shot (FLASH) pulse program. Flip angles of 30° were employed as well as a repetition time of 600 ms; 8 scans were averaged for each image. Two images were acquired for each field map at echo times of 6 and 10ms, respectively. The data was processed using home built software in *Mathematica*.

$\text{Eu}[\text{DTPA}]^{2-}$ solutions were prepared from a 82.2 ± 0.25 mM stock solution, which was prepared by adding 1 g of EuCl_3 (Sigma Aldrich) to a 50 mL volumetric flask. Separately, 3.93 g of diethylenetriaminepentaacetic acid (DTPA, Sigma Aldrich) and 1.99 g of NaOH (Fischer) were dissolved in 100 mL deionised (DI) water (Sigma Aldrich). An equimolar amount of the DTPA solution was added to the EuCl_3 solution. The pH of this solution was then adjusted by addition of 2M NaOH solution dropwise until a neutral pH was attained. This was then topped up to 50 mL using DI water.

Finite element calculations of field distributions in emulsions were carried out using COMSOL Multiphysics with the "magnetic fields, no currents" (mfnc) physics module. Optimisation of the shim structures was done with COMSOL Multiphysics^[72] Starting from a SolidWorks model of the chip design, which was also used as a basis for production of the devices using a laser cutter, a finite element model was assembled and meshed. The shim structures consist of four symmetrically arranged circular holes through the middle layer of the three-layered devices. The positions and the diameters of these holes were optimised using a Nelder-Mead simplex algorithm. At each iteration, the magnetic field distribution inside the sample chamber was calculated using the mfnc physics module. The square norm of the second derivative of the z -component of the magnetic field was integrated over the volume of the sample chamber, and was used as optimisation target.

2.4 Results and Discussion

While it is possible to predict the magnetic field distribution in a system of multiple phases with differing susceptibilities by solving the magnetostatic equation, this requires precise geometric information on the arrangement of the two phases. In the case of an emulsion, the arrangement of the droplets is not regular. However, at high droplet densities, it can be expected to approximate a dense packing of spheres. In order to obtain a semi-quantitative prediction, the demagnetising field in face-centred cubic (FCC) and simple cubic (SC) lattices of diamagnetic spheres was simulated; the results are shown in Fig. 2.4. A single unit cell containing one (SC) or two (FCC) independent spheres was meshed under periodic boundary conditions in all directions (Fig. 2.4C). As is well known, the demagnetising field inside an isolated diamagnetic sphere is homogeneous,

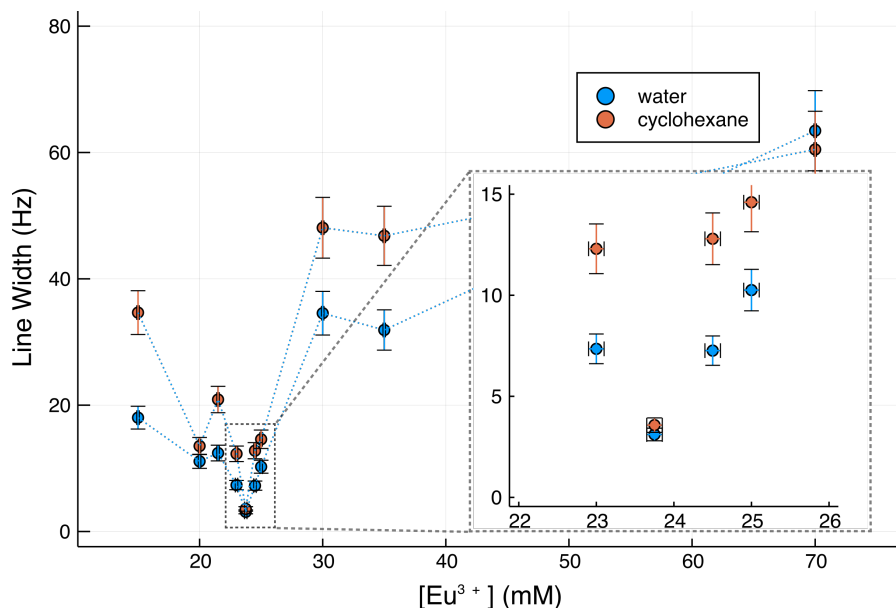


FIGURE 2.7: Observed line widths of water (blue circles) and cyclohexane (orange circles) in microfluidic droplet emulsions as a function of the $\text{Eu}[\text{DTPA}]^{2-}$ concentration in the aqueous phase. Inset is the plot around the minimum concentration. The widths of both lines are minimal at the matched concentration of 23.75 mM.

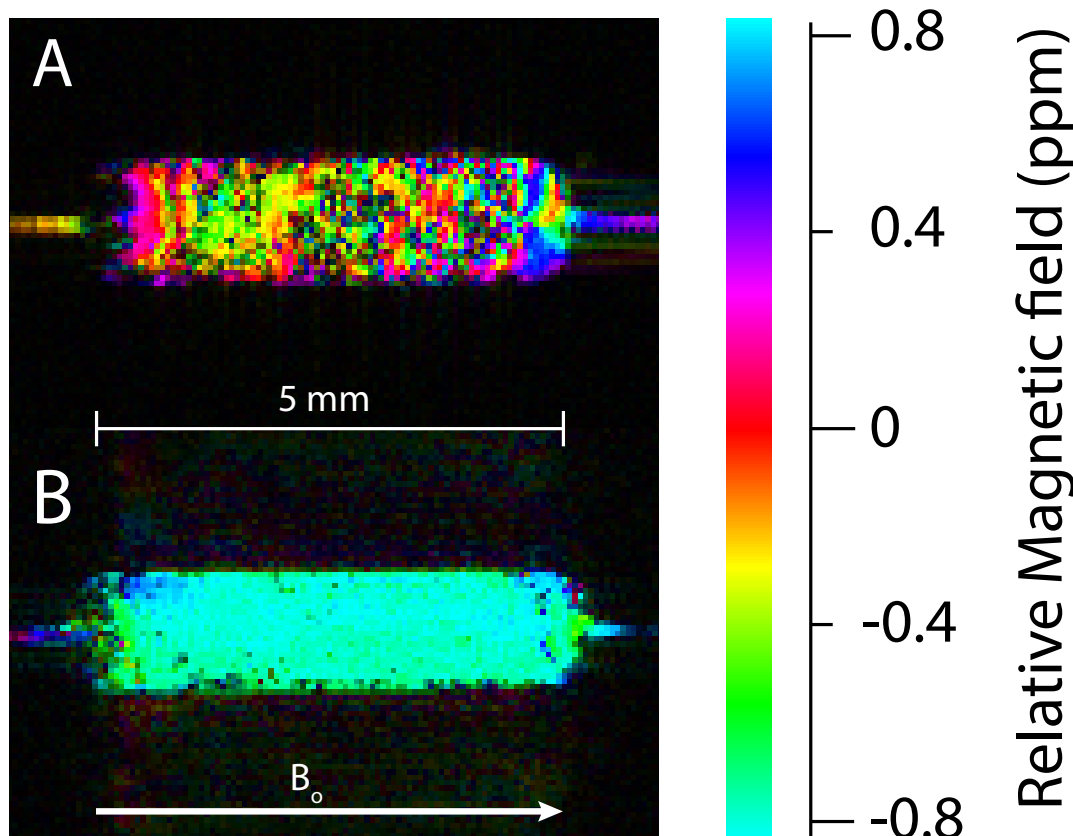


FIGURE 2.8: B_0 Field maps obtained by magnetic resonance imaging of emulsions with (A) $\Delta\chi = -1.41 \times 10^{-6}$ and (B) $\Delta\chi \approx 0$.

while the field outside of the sphere is that of a magnetic point dipole located at the sphere's centre. This situation is approximated in a lattice if the lattice constant is much larger than the sphere diameter. The computed demagnetising field of a small sphere in an SC lattice is shown in Fig. 2.4A. The contour levels display the z -component of the local demagnetising field normalised by the background B_0 field and the susceptibility difference $\Delta\chi = \chi_{\text{sphere}} - \chi_{\text{continuous}}$. The field is homogeneous inside the sphere, and a spatially varying demagnetising field only exists in the continuous phase. By contrast, in a densely packed face-centered cubic lattice the field is no longer homogeneous inside the spheres (Fig. 2.4B). The FCC lattice approximates the geometry of a dense microemulsion of homogenous water-in-oil droplets. Fig. 2.4D shows the histograms of the z -components of the demagnetising field in the continuous and droplet phases of the FCC lattice, respectively.

The NMR spectra expected from an ideal emulsion of the same geometry can be predicted from these histograms (neglecting no broadening contributions from the sample container). The magnetic field relevant for nuclear Larmor precession, often referred to as the "external" field[50] \mathbf{B}_{ext} is given by[68]

$$\mathbf{B}_{\text{ext}}(\mathbf{r}) = B_0(1 + \frac{\chi_s}{3})\mathbf{e}_z - \mu_0\nabla U_d(\mathbf{r}), \quad (2.10)$$

where B_0 is the magnitude of the external field, χ_s is the local magnetic susceptibility, and $U_d(\mathbf{r})$ is the scalar magnetic potential of the demagnetising field. The volume susceptibility of a solution containing a paramagnetic species at low concentration c_p is

$$\chi_s \approx \chi_0 + c_p \zeta_P, \quad (2.11)$$

where χ_0 is the volume susceptibility of the pure solvent, and ζ_P is the molar susceptibility of the paramagnetic species. ζ_P depends slightly on the molecular environment. For example, values of $5.86 \cdot 10^{-5}$ l/Mol, $5.68 \cdot 10^{-5}$ l/Mol, and $6.14 \cdot 10^{-5}$ l/Mol have been measured at 300K for Eu₂O₃, EuF₃, and EuBO₃, respectively[73]. To our knowledge, the precise molar susceptibility of Eu[DTPA]²⁻ in aqueous solution has not been measured to date, but it is likely to be similar to the above values.

Fig. 2.5 shows ¹H NMR spectra obtained from emulsions in the chip shown in Fig. 2.2 with varying Eu[DTPA]²⁻ concentrations in the aqueous phase as indicated in the figure. While the spectra are extremely broad without dopant, concentrations in the vicinity of 23 mM lead to much sharper lines for both water and cyclohexane, and the pure phase line widths are recovered at the optimum concentration of $c_p = 23.75$ mM. Using the susceptibilities given in Table 2.1, this leads to molar susceptibility for Eu[DTPA]²⁻ of $5.94 \cdot 10^{-5}$ l/Mol, well within the range of molar susceptibilities reported in literature for other Eu³⁺ compounds. Using this value, the histograms shown in Fig. 2.4D can be converted into predicted emulsion NMR spectra as a function of Eu[DTPA]²⁻

concentration in the aqueous phase, as shown in Fig. 2.6. The predicted behaviour is qualitatively similar to the experimental observation; very broad lines are expected at zero dopant concentration, while sharp lines are recovered near the optimum concentration. Also, the droplet phase peak is predicted to be narrower than the one from the continuous phase; this is already evident in the histograms in Fig. 2.4. However, the predicted spectra are consistently sharper than the experimentally observed ones. It is not entirely clear what causes the discrepancy between the experimental observation and the simulations. However, it should be noted that the experimental geometry of the emulsion differs significantly from the simulation; the droplets are neither uniform in size, nor are they arranged in a crystalline (FCC) lattice.

The observed widths of the NMR signals from cyclohexane and water are summarised in Fig. 2.7. Here, we define the line width as the ratio of the peak integral to the peak height, multiplied by $2/\pi$. In the case of Lorentzian line shapes, this definition is equivalent to the full width at half height (FWHM). However, the expected line shapes from the droplet emulsion are very different from a Lorentzian (Fig. 2.4D), such that using the FWHM would be misleading.

Both line widths exhibit a narrow minimum at 23.75 mM $\text{Eu}[\text{DTPA}]^{2-}$ in the aqueous phase. The water and cyclohexane minimum peak widths are 3.1 Hz and 3.5 Hz, respectively. For comparison, the best resolution that has been reached with the same NMR probe is 1.76 Hz for a homogeneous solution of 150 mM sodium acetate in H_2O . Finch *et al.* [17]

Fig. 2.8 shows magnetic field (B_0) maps of the sample chambers filled with droplet emulsions. In these experiments, two separate images with different echo times are acquired. The phase difference in each pixel is therefore proportional to the echo time difference and to the local magnetic field. The echo time difference is constant therefore the colour denotes the phase acquired by each pixel and can be used to inform on the homogeneity of the magnetic field in the sample.

In Fig. 2.8A, the droplets do not contain any paramagnetic dopant. As a result, the susceptibilities of the phases are unmatched, and strong local magnetic field differences are visible in the images. By contrast, the droplets in Fig. 2.8B are doped with 23.75 mM $\text{Eu}[\text{DTPA}]^{2-}$. As is clearly visible in the image, the local differences in the magnetic fields are strongly attenuated in this case.

While the above results have demonstrated that optimal line widths can be minimised in ^1H NMR spectra of microfluidic emulsions by paramagnetic doping, the question remains if this is sufficient to resolve homonuclear J -couplings of a few Hz. This is required in order to do meaningful NMR spectroscopy, particularly in the context of complex metabolic mixtures. The top trace in Fig. 2.9 shows a spectrum of 200 mM glucose and 23.75 mM $\text{Eu}[\text{DTPA}]^{2-}$ in water. The water signal has been suppressed by pre-saturation. In this case, the resolution is about 3 Hz; such that e.g., the triplet at

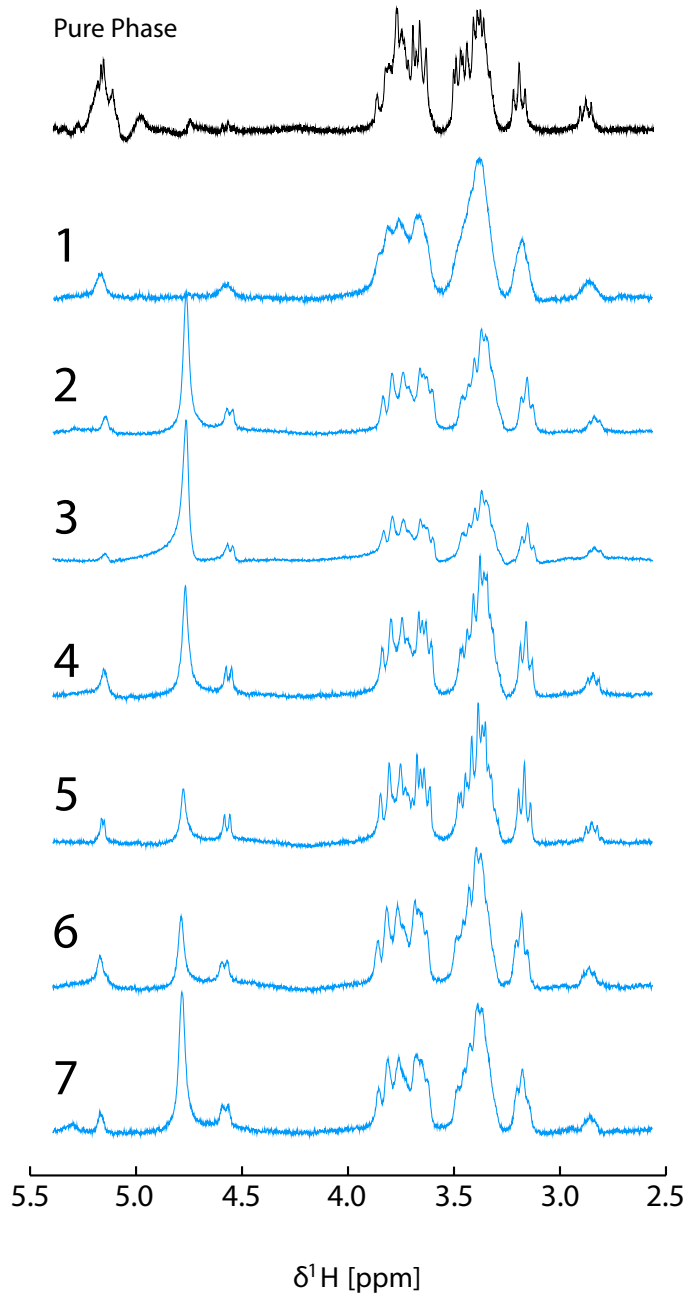


FIGURE 2.9: Spectra of 200 mM Glucose in H_2O obtained from microfluidic droplet emulsions in cyclohexane. 1: Aqueous phase contains $c_0 = 23.75 \pm 0.25$ mM $\text{Eu}[\text{DTPA}]^{2-}$. Spectra 2-7 have been obtained by gradual dilution of the aqueous phase with small amounts of DI water. 2: $\ln c/c_0 = -0.5\%$; 3: $\ln c/c_0 = -0.75\%$; 4 : $\ln c/c_0 = -0.875\%$; 5 : $\ln c/c_0 = -1.0\%$; 6 : $\ln c/c_0 = -1.125\%$; 7 : $\ln c/c_0 = -1.25\%$. A spectrum of pure phase 200mM glucose with optimised Eu doping in the same chip is included for comparison (black). The nonuniform peak at 4.8 ppm is due to carrier frequency drift during water suppression

3.2 ppm (which corresponds to the proton in the 2-position on the β -glucose anomer) is clearly resolved.

Spectrum 1 in Fig. 2.9 has been obtained from droplet emulsions, starting from an aqueous stock solution prepared to a nominal concentration of 23.75 mM in Eu[DTPA]²⁻ and 200 mM in glucose. Initially, the resolution in this spectrum is quite poor, in spite of the attempt to dope at the previously determined optimum concentration. Estimates predicted the pipetting and weighing errors to add up to an uncertainty in the concentration of the stock solution of $\pm 1\%$. Assuming the stock solution was too concentrated, rather than too dilute, it was then gradually diluted with small amounts of DI water corresponding to a change in concentration much less than the experimental error in each step. As can be seen in spectra 2-7, the resolution gradually increases, and matches the pure phase spectrum at spectrum 5, before it deteriorates again. In practice, high resolution spectra therefore require careful calibration of the dopant concentration. It may not be practical to achieve this in one step by preparing the stock solution, particularly if small volumes (around 10 ml or so) are used as in our experiments. Rather, a gradual dilution as in Fig. 2.9 may be required to calibrate the Eu[DTPA]²⁻ concentration for an accurate match of the aqueous and carrier fluid susceptibilities. However, if such a match is established, the resulting resolution is as good as that of the pure aqueous solution.

2.5 Conclusion

In Conclusion, susceptibility differences between the chip, the aqueous phase, and the oil phase in a microfluidic droplet system can be successfully mitigated by a combination of structural shimming and doping of the less diamagnetic of the liquid phases with a europium compound. The ultimate resolution achieved is only slightly inferior to what has been demonstrated in homogeneous solutions on a microfluidic chip and is suitable for high resolution NMR spectroscopy.

Chapter 3

Parahydrogen induced polarisation

The majority of the work in this chapter appears in [74]

3.1 Abstract

In this chapter a device that combines high-resolution NMR and parahydrogen induced hyperpolarization (PHIP) with a high-sensitivity transmission line micro-detector is discussed. The para-enriched hydrogen gas is introduced into solution by diffusion through a membrane integrated into a microfluidic chip. NMR microdetectors, operating with sample volumes of a few μl or less, benefit from a favourable scaling of mass sensitivity discussed in 1.3. However, the small volumes make it very difficult to detect species present at less than millimolar concentrations in microfluidic NMR systems.

In view of overcoming this limitation, parahydrogen-induced polarisation (PHIP) is implemented on a microfluidic device with $2.5 \mu\text{l}$ detection volume. Integrating the hydrogenation reaction into the chip minimises polarisation losses to spin-lattice relaxation, allowing the detection of picomoles of substance. This corresponds to a concentration limit of detection of better than $1\mu\text{M}\sqrt{\text{s}}$, unprecedented at this sample volume. The stability and sensitivity of the system can be used to extract quantitative information on the hydrogenation kinetics and their interplay with nuclear relaxation. It is further exemplified by homo- ($^1\text{H}-^1\text{H}$) and heteronuclear ($^1\text{H}-^{13}\text{C}$) 2D NMR experiments at natural ^{13}C abundance.

3.2 Hyperpolarisation

3.2.1 Sensitivity

In 1.2.1.2 it is demonstrated how NMR has low polarisation levels governed by the Boltzmann distribution given in Eqn. 1.1. For example, for a spin-1/2 particle in a static field of 14.1 Tesla there is only a factor of 6×10^{-6} difference in the populations of the α and β state. Compared to other spectroscopic techniques NMR suffers from poor limits of detection (LODs). Raman Spectroscopy, has LODs of $10^{-12} - 10^{-15}$, Laser induced fluorescence (LIF) has detected concentrations at 10^{-13} and mass spectrometry has achieved 10^{-19} . All of which are several orders of magnitude higher than that of NMR. While sensitivity is not a strong point, NMR is quantitative, non-invasive, and non-destructive making it an ideal tool for mass limited or living samples.

3.2.2 Signal Averaging

In NMR, the total signal that emerges from the probe contains signal from the sample under observation as well as uncontrolled random signals called noise. The most dominant source of noise comes from the thermal motions of the electrons in the receiver coil. In order for the signal that originated from the sample to rise above the noise, signal averaging must be employed. This works as the sum of two identical experiments is twice the signal of the original individual experiment:

$$s_{\text{NMR}}(1+2) = s_{\text{NMR}}(1) + s_{\text{NMR}}(2) = 2s_{\text{NMR}}(1) \quad (3.1)$$

The key is that this relationship doesn't apply equally to the noise which is random. A suitable definition of the noise amplitude in a single experiment is given by the root mean square (RMS) noise defined as:

$$\sigma_{\text{noise}} = \langle s_{\text{noise}}(1)^2 \rangle^{1/2} \quad (3.2)$$

where the angle bracket indicates an average over all sampling points. The RMS noise is the same for two experiments assuming the noise is stationary i.e. the noise doesn't change from one experiment to the next. However this does not imply that the noise from two experiments has twice the value. Summed over the two experiments the RMS noise takes the value:

$$\sigma_{\text{noise}}(1+2) \cong \sqrt{2}\sigma_{\text{noise}}(1) \quad (3.3)$$

Since the noise over two experiments increases by $\sqrt{2}$ but the signal doubles. Therefore the signal to noise ratio over two experiments can be written as:

$$\text{SNR}(1+2) = \sqrt{2} \frac{s_{\text{NMR}}(1)}{\sigma_{\text{noise}}(1)} \quad (3.4)$$

This can be extended to show the signal-to-noise over N transients is a factor \sqrt{N} larger than the signal for a single transient. So by signal averaging over many scans the SNR can be increased.

In principle this allows NMR signals that have a SNR less than one to be 'pulled out' of the noise. In reality this is time consuming as in order to repeat an experiment precisely it is essential to allow the spin system to reach thermal equilibrium again. The different NMR experiments must therefore be separated by an interval many times longer than T_1 , which in some case can be several seconds. For example, if the SNR of the first experiment is 0.1 clearly the signal will be buried in the noise. The SNR may be changed to 10:1 by signal averaging over 10,000 scans. If each scan takes 1 second this amounts to 3 hours of instrument time which is long but acceptable. However, if the SNR is 0.01 then it follows that 300 hours would now be needed which is not feasible.

In order for smaller signals to be detected, the amount of signal i.e. the amount of polarisation in the sample, needs to be increased this can be done by preparing the sample in a specific way and is referred to as 'hyperpolarisation'.

3.2.3 Hyperpolarisation - not sure on order here

As mentioned in 3.2.1 the polarisation levels of nuclear spins at room temperature is low. In fact, for protons it is only 3×10^{-6} per tesla[75]. The signal derived from an NMR experiment is proportional to this polarisation and means that the sensitivity and LOD is limited. The highest field available commercially is 28 Tesla which corresponds to polarisation levels in protons of 10^{-4} and whilst there are clear advantages to working in higher fields the size and more importantly - cost, make them unsuitable for many applications. Clearly just increasing the field is not a viable option if close to unity polarisation is to be achieved.

There are techniques for increasing the spin polarisation levels in samples to beyond the thermal equilibrium. The general term used to describe these is hyperpolarisation. Hyperpolarisation has applications in a diverse range of fields such as MRI [76, 77, 78, 79], drug discovery [80, 81], reaction monitoring [82, 83, 84], metabolomics [85, 86], catalysis[87, 88] and material chemistry [89, 90, 91].

However, these hyperpolarised states are still subject to relaxation as discussed in 1.2.1.8 and return to thermal equilibrium with time constant T_1 . This means the hyperpolarised spin order lasts seconds to minutes which limits their applications.

3.2.4 Techniques

3.2.4.1 Brute Force

The most simple technique for hyperpolarisation is "brute force". It is performed by simply cooling the sample to a few degrees kelvin in a high magnetic field [92, 93]. Under these circumstances the polarisation of the nuclei is 1%. After sufficient time has passed the sample is rapidly dissolved in a warm solvent in order to liberate the hyperpolarised species as a solution for detection.

There are drawbacks however, firstly, long T_1 times at cryogenic temperatures means long wait times are required in order to sufficiently build up polarisation in the sample. Secondly, and perhaps more importantly, the limit of polarisation with this technique is around 10^{-2} at achievable magnetic fields and temperatures.

3.2.4.2 Dynamic Nuclear Polarisation

Several different types of dynamic nuclear polarisation (DNP) have been reported. These are solution state DNP[94], solid state magic angle spinning (MAS) DNP[95] and static solid state DNP with dissolution and observation[96]. The latter is most commonly referred to as dissolution-DNP and written as d-DNP.

DNP methods use the thermal equilibrium electron spin polarisation to polarize the nuclei under investigation. Unity polarisation of the electrons is achieved by cooling to cryogenic temperatures (<2K) in a high magnetic field (>7 T). The electron polarization is transferred to nearby nuclear spins by saturating microwave frequency radiation.

The source of the electrons are 'free radicals' - molecules that have an unpaired electron spin, that are spread homogeneously throughout the sample after cooling the sample is held in a cryostat which is at 1.2 - 1.5K. The electrons have a much shorter T_1 in contrast to nuclear spins so after irradiation with microwave radiation to induce polarization transfer between electrons and nuclei, the electrons repolarise quickly compared to the nuclei who retain non-equilibrium polarization. This polarization diffuses throughout the sample. After some time, tens of minutes is not uncommon, the nuclear spins are polarised to around 0.1. The sample is then rapidly dissolved with a pressurised hot solvent into a separate high field magnet for detection.

The large equipment required for d-DNP, as well as the high cost of liquid helium for the cryostat and the superconducting magnets make this method prohibitive for most NMR groups.

3.3 Parahydrogen Induced Polarisation - PHIP

3.3.1 Parahydrogen

Hydrogen exists as a diatomic made up of two protons and two electrons. As such, the total wave function contains electronic, vibrational, rotational and spin components and can be written as:

$$\Psi^{tot} = \Psi^{elec}\Psi^{vib}\Psi^{rot}\Psi^{spin} \quad (3.5)$$

Because the two protons are fermions they are subject to the Pauli exclusion principle which states that the total wave function must be antisymmetric with respect to exchange. With this in mind, it is important to note that the electronic and vibrational states are symmetrical in the ground state and if we assume that they occupy the ground state, we find that the symmetry of the overall wave function depends of the symmetry of $\Psi^{rot}\Psi^{spin}$.

Rotational wavefunctions have quantum number J . For even numbers of J ($J=0,2,\dots$) the wavefunction is symmetric with respect to particle exchange for odd numbers of J ($J=1,3,\dots$) the wavefunction is antisymmetric. The nuclear spin wave function can also be symmetric or antisymmetric. By adding the angular momentum of both spins it can be shown that they combine to give four possible wavefunctions:

$$\Psi_1^{T+} = |\alpha\alpha\rangle \quad (3.6)$$

$$\Psi_1^{T0} = \frac{1}{\sqrt{2}}(|\alpha\beta\rangle + |\beta\alpha\rangle) \quad (3.7)$$

$$\Psi_1^{T-} = |\beta\beta\rangle \quad (3.8)$$

$$\Psi_0^{S0} = \frac{1}{\sqrt{2}}(|\alpha\beta\rangle - |\beta\alpha\rangle). \quad (3.9)$$

The three triplet (T) states have spin quantum number $I = 1$ and are symmetric with respect to spin exchange whilst the singlet (S) state has $I = 0$ and is antisymmetric. Hydrogen in the triplet state is referred to as *ortho* and the singlet state is referred to as *para*.

In order for Ψ^{tot} to be antisymmetric the antisymmetric rotational states are restricted to the symmetric (triplet) spin states whilst the symmetric rotational states are restricted to the antisymmetric (singlet) state.

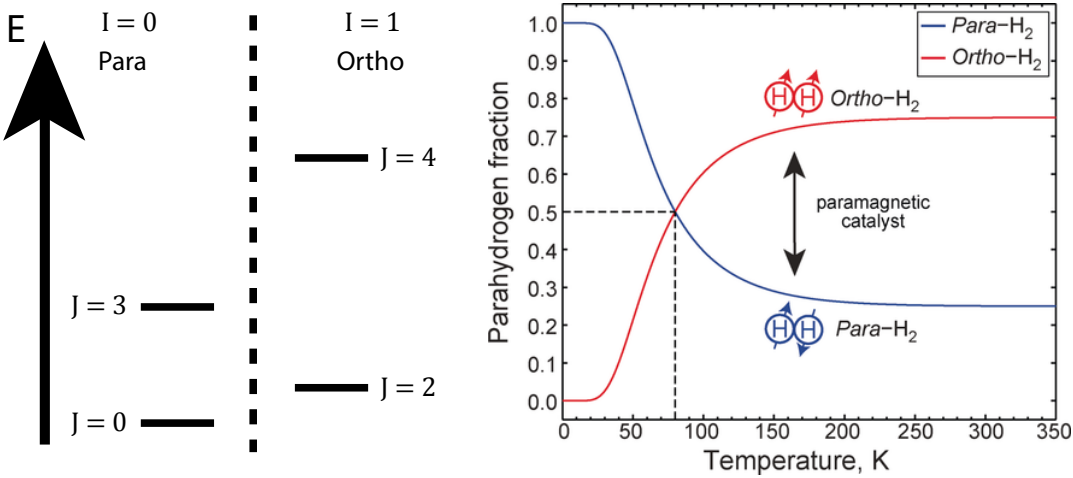


FIGURE 3.1: Left: The rotational energy levels of para- and orthohydrogen with their associated J values. Right: a graph showing the fraction of para- and orthohydrogen as a function of temperature. The dotted line shows 50% para enrichment that is achieved by cooling to 77K using liquid nitrogen. Image taken from [6].

The rotational energy is given by $E_j = \frac{J(J+1)\hbar^2}{2I}$ where I is the moment of inertia of the diatomic and is given by $I = \mu l^2$, where μ is the reduced mass, and l is the internuclear distance.

At room temperature the ratio of *ortho* to *para* hydrogen is 3 to 1. However, by cooling down hydrogen the lowest ($J = 0, 1$) rotational energy states start to become populated. By cooling alone the ratio would remain unchanged. One can't convert from *ortho* to *para* spin states without the aid of a catalyst (typically charcoal or iron (III) oxide). The catalyst temporarily breaks the symmetry of the H_2 molecule and allows these spin-spin transitions and allows a much larger fraction of the *para* form of hydrogen to be produced. Crucially, when warmed up to room temperature in the absence of a symmetry breaking catalyst, no conversion from the singlet state S_0 back to the triplet states T_+ , T_0 , T_- occurs. This is because the nuclear spin flip required would not conserve angular momentum and is therefore disallowed. It is therefore possible to store pure parahydrogen in the right container for days to weeks.

Para enrichment fraction, f , can be measured by NMR. By measuring the oH_2 signal of the enriched H_2 (S_e) and comparing it to the signal obtained from the same amount of H_2 at room temperature (S_{rt}). The enrichment fraction is given by[[97, 98]:

$$f = 1 - (3S_e/4S_{rt}) \quad (3.10)$$

3.3.2 PASADENA and ALTADENA

Parahydrogen and synthesis allow dramatically enhanced nuclear alignment (PASADENA)[99] and adiabatic longitudinal transport after dissociation engenders net alignment (ALTADENA)[100] are subclasses of PHIP experiments characterised by the strength of magnetic field in which the hydrogenation and detection are performed.

The difference between PASADENA and ALTADENA are the J -coupling regimes in which the reaction and detection happens. In PASADENA experiments the reaction and detection is carried out at high field (>1 T) whereas in ALTADENA, the reaction is carried out at low field (< 10 mT), and the product is transferred to a high magnetic field for detection[101].

This difference manifests itself as a difference in J -coupling regimes in the *parahydrogen* derived hydrogens in the product molecule. ALTADENA refers to hydrogens in the strong coupling regime and PASADENA refers to the weak coupling regime. The regime is determined by the value of the J -coupling (in Hz) compared to the value of the difference in chemical shifts of the individual protons. Where the strong regime has J -couplings that take the approximate value of the difference in chemical shift ($\frac{\delta\omega}{J} \approx 1$) and the weak regime has J -couplings much smaller than the difference in chemical shift ($\frac{\delta\omega}{J} \gg 1$). Since the chemical shift depends on external magnetic field (B_0) and the J -couplings are independent of field one can select an appropriate magnetic field for the desired experiment.

3.3.2.1 Spin Physics

The spin physics of these types of hydrogenative PHIP are accessible through the density operator formalism. In a PASADENA type experiment, parahydrogen is then added to molecule in high field forming a weakly coupled AX system of the type discussed in 3.3.2. Due to the weak coupling, $\frac{\delta\omega}{J} \gg 1$, the eigenbasis is close to the Zeeman basis. The initial density operator, $\hat{\rho}_{\text{ini}}$ from our earlier definitions this is:

$$\hat{\rho}_{\text{ini}} = |\Psi_0^S\rangle \langle \Psi_0^S| = \frac{1}{2} |\alpha\beta - \beta\alpha\rangle \langle \alpha\beta - \beta\alpha| \quad (3.11)$$

using the zeeman basis states for a 2 spins system described in 1.2.2.2

$$\hat{\rho}_{\text{ini}} = \frac{1}{2} \begin{pmatrix} 0 \\ 1 \\ -1 \\ 0 \end{pmatrix} \otimes (0 \ 1 \ -1 \ 0) \quad (3.12)$$

$$= \frac{1}{2} \begin{pmatrix} 0 & 0 & 0 & 0 \\ 0 & 1 & -1 & 0 \\ 0 & -1 & 1 & 0 \\ 0 & 0 & 0 & 0 \end{pmatrix} \quad (3.13)$$

(3.14)

These diagonal elements (populations) do not evolve as these components commute with the Hamiltonian. The off-diagonal elements (coherences) evolve at a rate $\approx \delta v$.

As the reaction continues an ensemble of molecules that are hydrogenated at different time points, this gives a new density operator, $\hat{\rho}_p r$, expressed as:

$$\hat{\rho}_{\text{pas}} = \frac{1}{t} \int_t^0 \exp\{-i\hat{H}t\} \hat{\rho}_{\text{ini}} \exp\{+i\hat{H}t\} dt \quad (3.15)$$

Usually, the hydrogenation period is much longer than the coherence evolution. These average to zero and so the density operator becomes:

$$\hat{\rho}_{\text{pas}} = \frac{1}{2} \begin{pmatrix} 0 & 0 & 0 & 0 \\ 0 & 1 & 0 & 0 \\ 0 & 0 & 1 & 0 \\ 0 & 0 & 0 & 0 \end{pmatrix} \quad (3.16)$$

Fig. 3.2 shows the eigenstate populations and general simulated spectra of a thermal equilibrium experiment and a PASADENA experiment.

In a usual NMR spectra a $\pi/2$ pulse is used to excite observable single quantum coherences. For a PASADENA signal to be observed, a $\frac{\pi}{4}$ pulse must be used. The reason becomes clear when $\hat{\rho}_{\text{pr}}$ is rewritten in terms of angular momentum operators, neglecting the identity matrix this is:

$$\hat{\rho}_{\text{pas}} = -\hat{I}_{1z}\hat{I}_{2z} \quad (3.17)$$

a $\frac{\pi}{2}$ pulse has the following effect:

$$\hat{R}_y\left(\frac{\pi}{2}\right)\hat{\rho}_{\text{pas}} = -\hat{I}_{1x}\hat{I}_{2x} \quad (3.18)$$

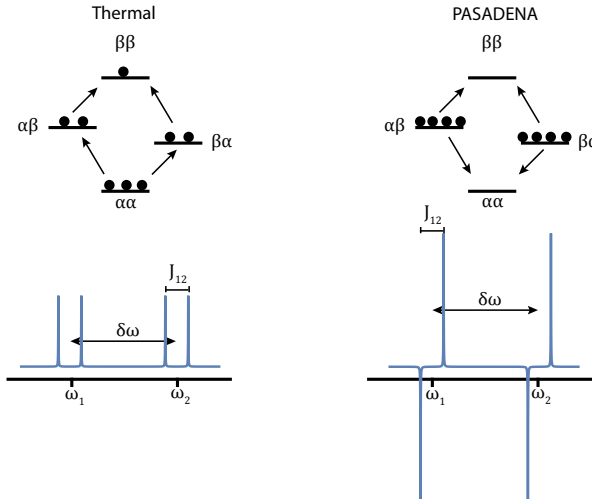


FIGURE 3.2: Above: Populations of states represented as balls in a thermal (left) and a PASADENA experiment (right). Below: Simulations of spectra arising from adding thermal hydrogen to a molecule (left) and of a PASADENA experiment when adding parahydrogen.

which is an unobservable double quantum coherence and the reason pure parahydrogen is NMR silent. However, a $\pi/4$ y -pulse gives:

$$\hat{R}_y\left(\frac{\pi}{4}\right)\hat{\rho}_{\text{pas}} = -\frac{1}{2}(\hat{I}_{1x}\hat{I}_{2x} + \hat{I}_{1x}\hat{I}_{2z} + \hat{I}_{1z}\hat{I}_{2x} + \hat{I}_{1z}\hat{I}_{2z}) \quad (3.19)$$

where the $\hat{I}_{1x}\hat{I}_{2z}$ and $\hat{I}_{1z}\hat{I}_{2x}$ terms are observable.

In an ALTADENA exeriment, the hydrogenation is performed at low field. In this case, when a molecule of hydrogen is added to a substrate the denstiy operator - $\hat{\rho}_{\text{ini}}$, is projected onto the new eigenbasis which at low field (where $\frac{\delta\omega}{J} \ll 1$) is the singlet-triplet basis. To a good approximation the only term is the $|S_0\rangle$ and there is no evolution of the system.

The sample is then transferred to high-field (where $\frac{\delta\omega}{J} \gg 1$). It is done adiabatically, this is defined as the rate of change of magnetic field being small with respect to the value of the J -coupling between them, squared denoted as $(J_{12})^2$. As the field increases, the eigenbasis changes from singlet-triplet to the Zeeman basis. The adiabatic change carries the population of the $|S_0\rangle$ state to the $|\alpha\beta\rangle$ state this is shown graphically in Fig. 3.3 In this case, only one of the four energy levels, namely $\alpha\beta$ is now populated, therefore the density operator, $\hat{\rho}_{\text{alta}}$ is given by:

$$\hat{\rho}_{\text{alta}} = |\alpha\beta\rangle\langle\alpha\beta| \quad (3.20)$$

This leads to [100]:

$$\hat{\rho}_{\text{alta}} = \hat{I}_{1z}\hat{I}_{2z} \pm (\hat{I}_{1z} - \hat{I}_{2z}) \quad (3.21)$$

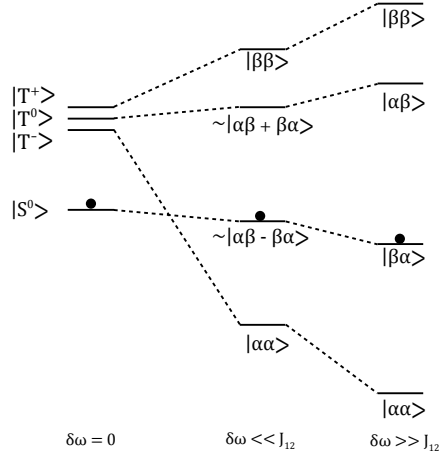


FIGURE 3.3: Correlation diagram for the ALTADENA effect. Hydrogenation at low field populates the singlet state, adiabatically increasing the field carries the population into a high field state.

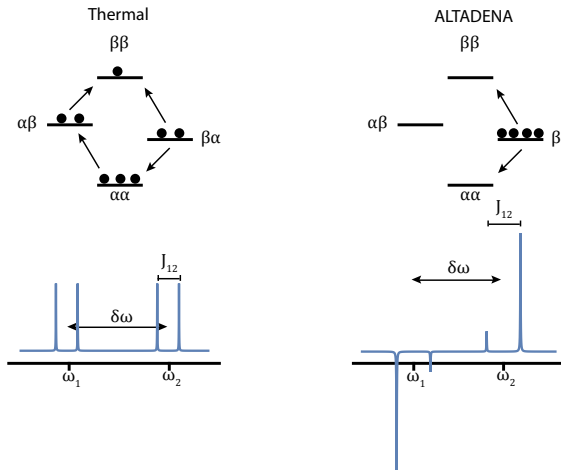


FIGURE 3.4: Top: Populations of Zeeman states represented by balls for thermal(left) and ALTADENA(right) experiments. Bottom: Simulations of a thermal spectrum after applying a $\pi/4$ pulse and an ALTADENA experiment.

The result of a $\pi/4$ pulse along the y -axis yields:

$$\hat{R}_y\left(\frac{\pi}{2}\right)\hat{\rho}_{\text{alta}} = \frac{1}{2}(\hat{I}_{1z}\hat{I}_{2x}) \pm \frac{1}{2\sqrt{2}}(\hat{I}_{1x} - \hat{I}_{2x}) \quad (3.22)$$

This gives rise to the two out of phase doublets that are typical for an ALTADENA experiment on an AX system. A diagram is provided in Fig. 3.4 that shows a simulated spectra compared to a thermal spectrum.

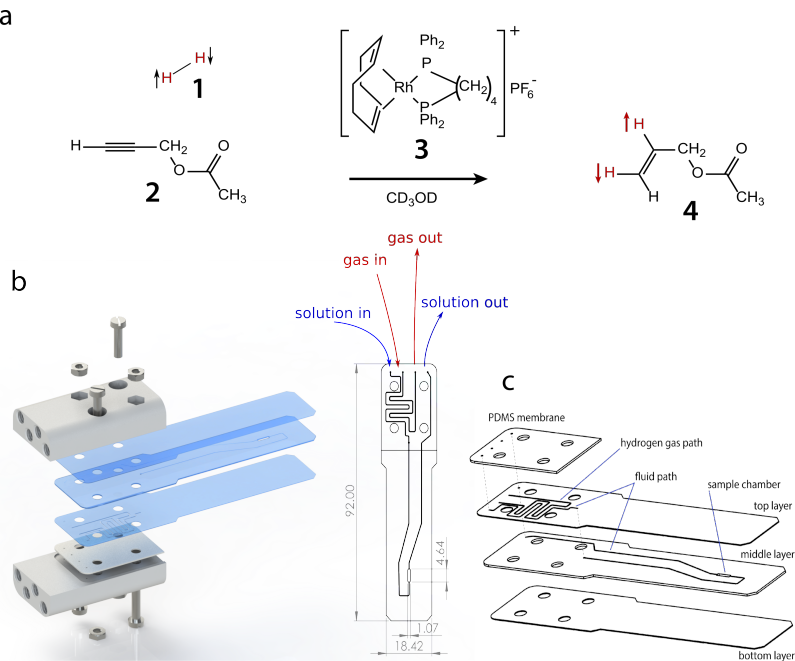


FIGURE 3.5: Overview of the PHIP@chip experiment. a: scheme of the hydrogenation reaction; b: CAD rendering of the chip assembly with individual chip layers separated, consisting of the PMMA chip, PDMS membrane, and two 3D printed holders with threads for the gas and fluid connections; The hydrogen gas diffuses through the PDMS membrane into the flowing liquid; c: Outline drawing of the chip (dimensions in mm).

3.4 Introduction

High-resolution NMR spectroscopy is a superbly versatile method which provides detailed and quantitative information on chemical composition and structure. It is widely used to follow the progress of chemical reactions [102, 103], as well as metabolic processes in living systems [104, 105, 106, 107]. However, NMR suffers from inherently low sensitivity, which is due in part to the very weak polarisation of nuclear spins along the magnetic field for samples in thermal equilibrium at ambient conditions. Conventional high-resolution NMR therefore requires nanomole quantities of sample. Many important problems require detection of analytes at low micromolar concentrations, such as transient reaction intermediates, or metabolic species. Despite the comparatively higher mass sensitivity of NMR for small sample volumes [108, 109], conventional micro-NMR systems around 1 l achieve mass limits of detection of no better than [17] $1 \text{ nmol}\sqrt{\text{s}}$, corresponding to a concentration limit of detection of $1 \text{ mM}\sqrt{\text{s}}$. An increase of several orders of magnitude in sensitivity is therefore required to enable NMR studies of mass-limited samples at micromolar concentrations.

Microfluidic lab-on-a-chip devices are finding increasing applications in chemistry and the life sciences. They provide detailed control over the experimental conditions at a much smaller length scale than conventional reactors, and allow integration of synthesis, separation, and analytical steps on a single platform [110, 111, 112, 113, 114, 115, 116,

[117]. The small size also affords the possibility of high experimental throughput. In the life sciences, microfluidic devices are increasingly used as sophisticated culture platforms for cells, cell assemblies, tissues, and small organisms [118, 119, 120, 121, 122, 123]. The integration of NMR with microfluidics [124, 2, 125, 17] is promising, as it enables in-situ, non-invasive monitoring of chemical and metabolic processes in lab-on-a-chip systems.

The usefulness of microfluidic NMR could therefore be significantly enhanced if the following conditions could be met: (i) sample volumes around $1 \mu\text{l}$ or less; (ii) a concentration limit of detection near $1 \mu\text{M}\sqrt{s}$; and (iii) spectral resolution of better than 0.01 ppm to allow distinction and identification of chemical species.

Although exquisitely sensitive NMR detection schemes exist, approaching even single-spin detection in favourable cases [126, 127, 128, 129, 130, 131, 132, 133, 134, 135, 136], they lack spectral resolution. While a recent study has demonstrated resolution of J couplings using a nitrogen-vacancy (NV) centre magnetometer.[137], none of these alternative detection schemes are compatible with high (several Tesla) magnetic fields, which are essential to produce spectral dispersion by chemical shifts. So far, no method has been demonstrated with the combination of high spectral resolution, high chemical dispersion, and high sensitivity for small volumes required for advanced microfluidic NMR measurements significantly below the 1 mM concentration scale.

Hyperpolarisation methods generate substances which exhibit a transiently high level of nuclear spin polarisation, with an increase in the NMR signal strength of more than 4 orders of magnitude [138], can be combined with micro-NMR detectors and microfluidic systems [139, 140, 141, 142, 143, 144, 145, 146]. One such method involves the chemical reaction of the singlet spin isomer of molecular hydrogen, and is called parahydrogen-induced hyperpolarisation (PHIP) [147, 148, 149, 150].

While most studies have so far brought the reaction liquid in direct contact with hydrogen gas either through bubbling or by atomisation of the liquid in a hydrogen-filled chamber [151, 152, 153, 154, 155, 156, 157], liquid-gas interfaces and in particular bubbles pose difficulties in the context of microfluidic devices, since they tend to alter the flow properties, and can block fluid transport altogether. Continuous delivery of parahydrogen by diffusion through gas-permeable membranes has been demonstrated at conventional size scales [158, 159]. It has been shown that silicone elastomer membranes can be used to deliver parahydrogen directly to a flowing liquid in a microfluidic device [145]. Bordonali et al[146] have recently combined a microfluidic NMR probe system with a gas exchange chip based on a silicone elastomer membrane to implement the SABRE (signal enhancement by reversible exchange) variant of parahydrogen-induced polarisation, but achieved only small signal enhancement factors (3 to 4).

In distinction from previous work [151, 152, 153, 154, 155, 156, 157, 159], this work integrates the hydrogenation reactor into the chip itself, which greatly reduces the polarisation losses due to spin-lattice relaxation. As shown below, a signal enhancement

factor over thermal polarisation of about 1800 is achieved, allowing detection of a picomole quantity of analyte in a sample volume of $2.5 \mu\text{l}$, while maintaining the full resolution of conventional ^1H NMR spectroscopy.

This is accomplished by letting the parahydrogen gas diffuse through a silicone elastomer membrane [159] to come into contact with a solution flowing through the chip at a constant rate. The solution contains a precursor, which is hydrogenated through a homogeneous catalyst also present in the solution. The microfluidic device is held in the bore of a conventional NMR magnet using a purpose-built transmission line NMR probe. This yields a continuous on-chip stream of hyperpolarised material. As shown in the following, in addition to very high detection sensitivities, this also results in a continuous and highly stable operation of the system, making it possible to perform hyperpolarised two-dimensional NMR experiments [158, 160, 161, 162]. By replacing the hyperpolarised gas feed with hydrogen gas at thermal equilibrium, it is possible to gain kinetic information on the hydrogenation process, as well as to calibrate the intensity of the hyperpolarised NMR signals. This allows accurate assessment of the achieved polarisation levels, something that has been notoriously difficult in the context of parahydrogen-induced polarisation.

3.5 Materials and methods

The microfluidic chips were constructed from three layers of cell cast PMMA sheet material (Weatherall Equipment). The sheet thickness was $200 \mu\text{m}$ for the top and bottom layers, and $500 \mu\text{m}$ for the middle layer. The fluid and gas channels were designed on AutoCAD and cut into the PMMA using a laser cutter (HPC Laser L3040) to a width and depth of $150 \mu\text{m}$. The layers were subsequently bonded together with a plasticiser (2.5% v/v dibutyl phthalate in isopropyl alcohol) under heat and pressure (358 K, 3.5 tonnes) [69]. The total internal fluid volume is $4 \mu\text{l}$, and the sample chamber is $2.5 \mu\text{l}$.

The device also employs a poly(dimethyl siloxane) (PDMS) membrane (Shielding Solutions) to facilitate para- H_2 transport, of 1 mm thickness with laser-cut screw holes. The parahydrogen polarisation lifetime in the PDMS after O_2 removal was measured to be $\sim 4 \text{ h}$. To determine the hydrogen ortho- para conversion in PDMS, the ortho-para conversion time of H_2 dissolved in PDMS was measured. A high-pressure NMR tube of 5 mm outer diameter (Sigma-Aldrich) was filled with PDMS resin (Sylgard 84, 3M). A teflon capillary of 1/16 inch outer diameter (Sigma-Aldrich) was pushed into the NMR tube along the central axis, and the PDMS was allowed to cure. The capillary was then removed, leaving a cylindrical void in the centre of the NMR tube. The tube was then exposed to vacuum for varying amounts of time, in order to study the conversion effect of the residual oxygen the results of which are shown in Fig. 3.6.

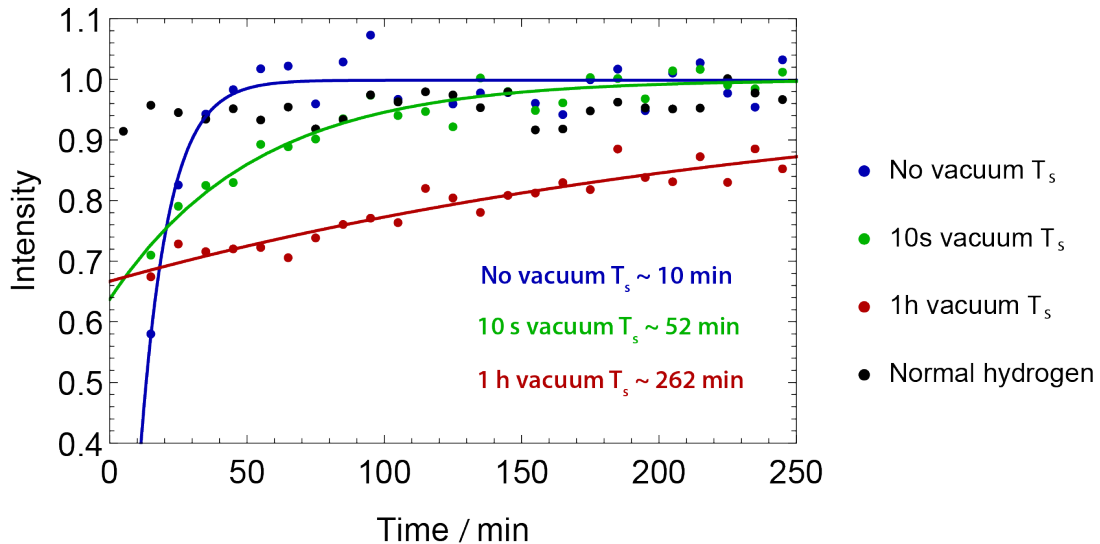


FIGURE 3.6: Ortho-para conversion of hydrogen in PDMS after various times under vacuum.

The PMMA chip and PDMS membrane layer are sealed with a pair of screw-tightened 3D printed (Accura Xtreme, Proto Labs) holders, with fluid and gas in/out ports (to fit Kinesis UK NanoPorts).

The assembled microfluidic device was put in a transmission line based home-built probe [1]. The device sits between the two stripline planes on a sample holder having sample chamber of the device coinciding with the constriction on stripline planes. All NMR experiments were performed at a field strength of 11.7 T with an AVANCE III console. Nutation frequencies for RF pulses were 100 kHz for protons, and 20 kHz for carbon in the case of the HMQC spectrum. 16k data points were acquired over 1.2 s for proton 1D spectra. Saturation recovery experiments used a train of 512 $\pi/2$ pulses separated by a delay of 0.1 ms, followed by a recovery delay, and a $\pi/4$ excitation pulse. The PH-TOCSY spectrum was acquired using the States-TPPI method, with 256 t_1 increments, averaging 8 transients per increment. 2048 complex data points in 0.2 s were acquired for each increment. The PH-HMQC experiment was acquired using the States method, with 128 t_1 increments, averaging 8 transients with 2048 complex points over 0.2 s. 1D spectra were processed using MestreNova (Mestrelab, Italy). 2D spectra were processed using scripts written in Julia [71].

To generate parahydrogen gas at 50% para enrichment, hydrogen gas (purity 99.995%) was passed through a home-built parahydrogen generator containing an iron (III) oxide catalyst cooled to 77 K using liquid nitrogen.

The solution before reaction was 20 mM propargyl acetate and 5 mM 1,4-bis(diphenylphosphino)butane(1,5-cyclooctadiene)rhodium tetrafluoroborate in methanol-d₄. In an attempt to avoid possible spin relaxation or chemical side-reaction effects, dissolved oxygen from the atmosphere was removed by 5 minutes of vigorous helium bubbling.

The parahydrogen gas was delivered through a PTFE tube (1/16 inch O.D., 1/32 inch I.D.) into the 3D printed chip holder, and out via a second PTFE line, using a mass flow controller (Cole-Parmer) to limit the flow to 20 ml min^{-1} at an overpressure of 5 bar. Although most of the parahydrogen gas passes directly through the system, some amount dissolves into the PDMS layer, which in terms of H_2 solubility behaves similarly to other organic solvents. The solution was loaded into a 3.5 ml plastic syringe with a Luer lock connection to in-flow PEEK tubing (1/16 inch O.D., 0.007 inch I.D.) leading to the chip. The same tubing was used for the solution out-flow into a container exposed to a back pressure of 1.5 bar of nitrogen gas, to preventing formation of hydrogen bubbles in the chip. Solution flow into the chip was controlled with a syringe pump (Cole-Parmer).

3.6 Results and Discussion

The hydrogenation reaction system employed in the present work is shown in Fig. 3.5a. Parahydrogen-enriched hydrogen gas **1** was allowed to react with propargyl acetate **2**, in the presence of a rhodium catalyst **3**. The substrate **2** was chosen in view of future studies based on side-arm hydrogenation [155, 156, 163].

3.6.1 ALTADENA

In order to verify that the parahydrogen transfer on chip was possible, an experiment was performed whereby the parahydrogen transfer was microfluidic and ‘on chip’ but the detection was performed in a conventional NMR tube and probe.

This ALTADENA type experiment involved the addition of para enriched hydrogen gas to propargyl acetate outside the magnetic field in a device shown in FIG. This device is a simpler version of the one eventually used. It features 3D printed holders that are used to deliver the gas and liquid as well as seal against any liquid or gas leak. The chip is made from a single 500 μm thick layer of PMMA with serpentine paths for liquid and gas flow. B in the Fig. 3.7 shows the path structure in the chip as well as the hydrogen and fluid paths respectively.

The set-up for this experiment employs a syringe pump, the hydrogenation device outside the magnet and a standard 5 mm NMR tube inside the 16.5 T magnet. The device was pressurised with 5 bar of 50% enriched parahydrogen and allowed to equilibrate for some time. Then, $100 \mu\text{l}$ was flown through the device at a flow rate of $1000 \mu\text{l min}^{-1}$ this was done to ensure the sample from the experiment would reside completely in the sensitive area. For the ALTADENA, $350 \mu\text{l}$ was flown through the device and collected in the magnet. A $\pi/4$ pulse was applied and the spectra recorded the result of the experiment is shown in Fig. 3.8.

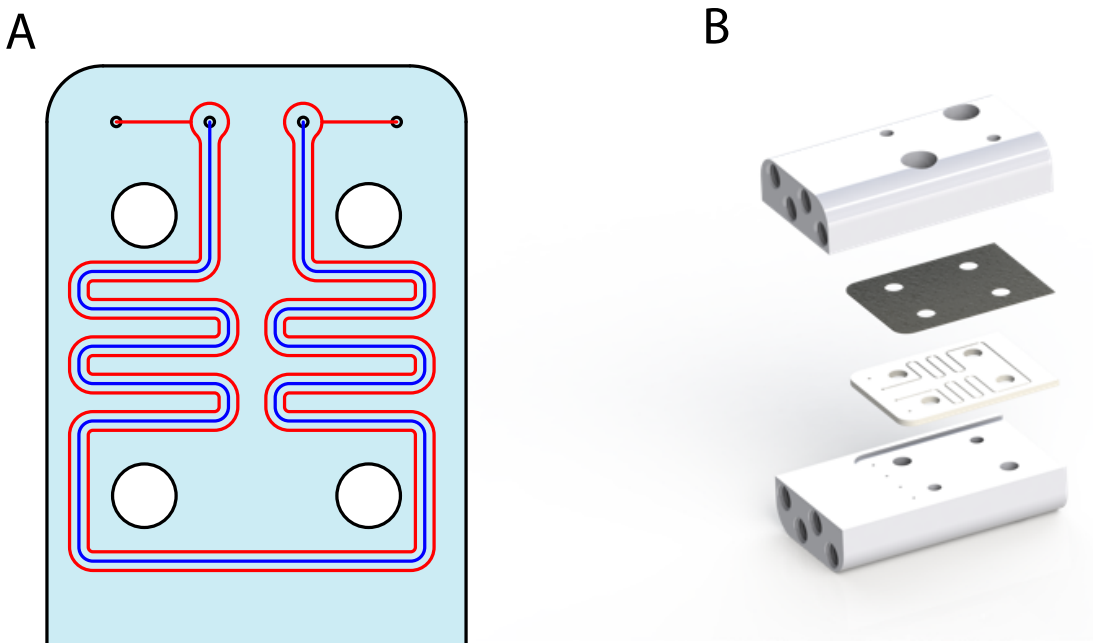


FIGURE 3.7: A) Liquid channel (blue) and hydrogen channel (red) as scored onto the PMMA layer of the device. B) A 3D render of the hydrogenation device used for the ALTADENA experiments.

A comparison is shown between scans taken of the same experiment, in Fig. 3.8 i) spectra from an experiment with thermal hydrogen and ii) one with parahydrogen. The parahydrogen ALTADENA signal (ii) exhibits the characteristic inverted peaks and a much higher signal to noise ratio (SNR) and gives enhancement by comparison of the SNR of around 200. This result proved that parahydrogenation induced polarisation (PHIP) on a chip was possible by bubble free transfer through a PDMS membrane in our devices.

3.6.2 PASADENA

Fig. 3.5b and c show the microfluidic device used for the present study. It consists of a chip made from PMMA, which houses a sample chamber of 2.5 l volume that aligns with the transmission line detector of a home-built NMR probe assembly, which was fitted inside of an 11.7 T NMR magnet. Fluid is flown through the chip by means of a syringe pump installed outside of the magnet bore; connections are made through threaded ports in the two 3D-printed holders shown in Fig. 3.5b. Para-enriched H₂ gas at 5 bar above ambient pressure flows through a second channel in the chip (shown in red in Fig. 3.5b), which runs in the immediate vicinity of the liquid channel (a depiction of the set-up is given in Fig. 3.9).

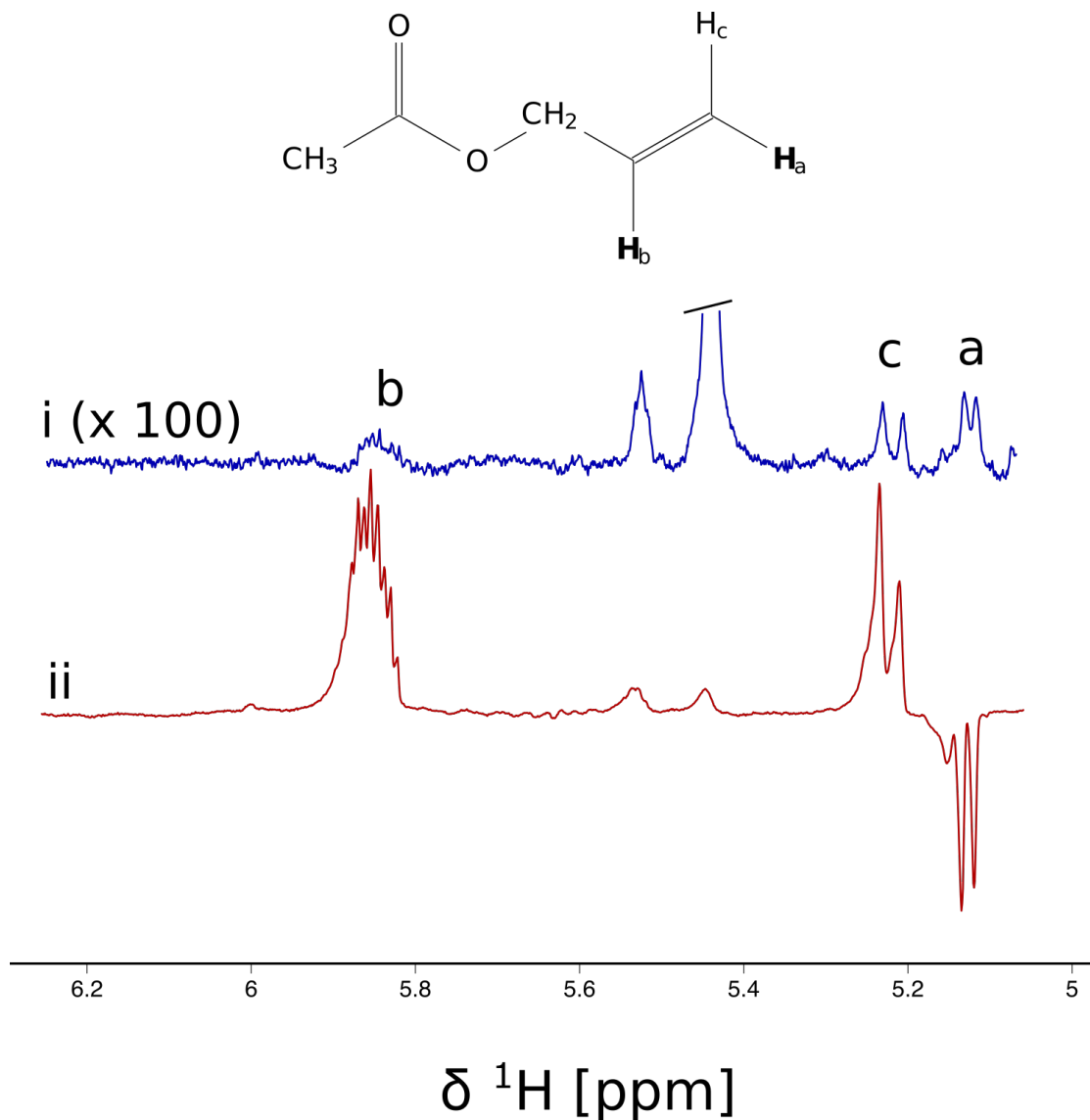


FIGURE 3.8: Spectra obtained from i) a thermal hydrogenation and ii) a parahydrogenation of propargyl acetate to give allyl acetate with hydrogens derived from parahydrogen labelled a and b. By comparison of SNR the enhancement for the ALTADENA experiment is 200.

The chip consists of three laser-cut layers of poly methylmethacrylate (PMMA) bonded together, as shown in Fig. 3.5b and c. Channels in the left part of the chip, where it is clamped between the holders, are cut through the top layer, while they are scored into the middle layer of the chip (and hence sealed from the outside) in the free part of the device. Within the clamps, the exposed channels are sealed by means of a PDMS membrane. The flowing liquid as well as the pressurised hydrogen gas are therefore exposed to the PDMS layer, which serves as a diffusion bridge for the hydrogen. The holders, made by 3D printing, keeps the membrane and the chip aligned, and maintains mechanical pressure to ensure sealing. Channels inside the holders guide the fluid and gas to and from the four access points at the top end of the chip, as shown in Fig. 3.5c.

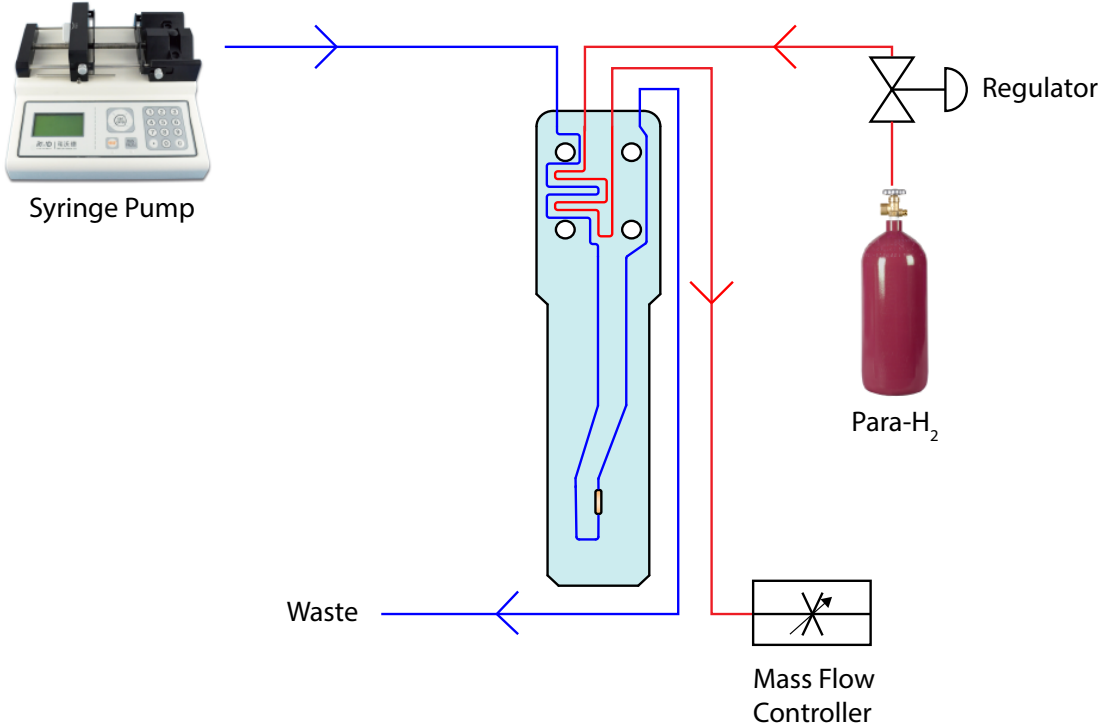


FIGURE 3.9: Drawing of PHIP@chip setup. It shows the solution (blue line) of propargyl acetate, catalyst and methanol being fed into the magnet via a syringe pump. Simultaneously, parahydrogen (red line) is fed in at the desired pressure and regulated by a mass flow controller to a flow rate of 20 ml min^{-1} . Both of these are fed into the microfluidic device depicted in Fig. 3.5

The PDMS membrane acts both as a diffusion conduit for hydrogen gas and as a fluid seal. In a crucial difference to the otherwise similar geometry of the hydrogenation chip used by Bordonali et al[164], the gas and liquid channels are arranged side by side, and molecular hydrogen diffuses through the bulk of the PDMS membrane rather than through the thickness. By clamping the PDMS membrane onto the chip using the holders, this makes it possible to use large gas pressures (up to 5 bar in the present experiments). This would be difficult to achieve in the chip presented by Bordonali et al, which has the liquid and gas channels arranged on opposite sides of the membrane.

3.6.3 Signal Analysis

Fig. 3.10 shows the results of a steady-state PHIP@chip experiment. The PDMS membrane is equilibrated with para-enriched hydrogen gas, which is supplied from an aluminium storage tank at a regulated pressure of 5 bar. The gas flow rate is kept constant at 20 ml min^{-1} by means of a mass flow controller placed after the chip. This ensures that the gas channel always contains fresh para-enriched hydrogen gas at the design pressure of 5 bar. The fluid channel of the chip is pre-filled with a solution of 20 mM precursor **2** and 5 mM catalyst **3** in methanol-d₄. NMR spectra are acquired every 30 s,

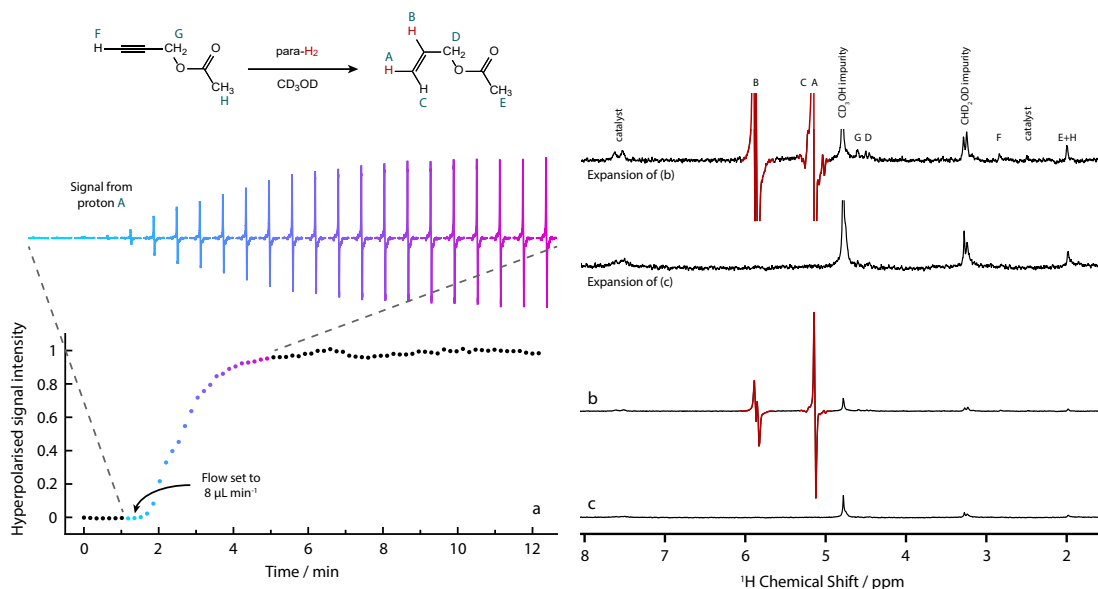


FIGURE 3.10: Proton NMR spectra obtained in continuous flow. a: Buildup of the hyperpolarised signal after initiation of flow; b: hyperpolarised NMR spectrum. Antiphase doublets from the two hyperpolarised protons A and B are clearly visible at 5.2 ppm and 5.9 ppm, respectively. c: control spectrum obtained with thermal H₂ gas. Top right: traces b and c with the vertical axis expanded by a factor of 10.

using a $\pi/4$ excitation pulse. The fluid channel is connected to a syringe pump situated outside the NMR magnet. The liquid flow is started by setting the target flow rate on the syringe pump to 8 lmin^{-1} (marked by an arrow Fig. 3.10a). The NMR signal intensity begins to rise about 30 s later, and reaches saturation after about two minutes. The NMR spectra are dominated by an antiphase doublet, centred at 5.17 ppm, and an antiphase multiplet at 5.92 ppm, corresponding to protons in the A and B positions of the hydrogenation product (Fig. 3.10b). Upon replacing the para-enriched hydrogen gas with normal hydrogen gas, these signals are no longer observed (Fig. 3.10c).

Using normal hydrogen gas, a fully labelled spectrum of the reaction mixture was obtained using a lower flow rates whilst maintaining the 5 bar of hydrogen pressure. This allowed the solution to saturate with methanol and facilitated the quantification of the product and dissolved hydrogen. A fully labelled spectrum obtained using a flow rate of $2\mu \text{lmin}^{-1}$ is shown in Fig. 3.12

3.6.4 Hydrogen Transport

The hydrogen transport through the membrane and its uptake into the flowing liquid was simulated using two coupled finite element models: a dilute species diffusion model for hydrogen gas in the PDMS membrane, and a dilute species diffusion and convection model for hydrogen dissolved in the flowing liquid. The hydrogen partial pressures at the liquid/PMDS interface are constrained to be equal, and the hydrogen partial

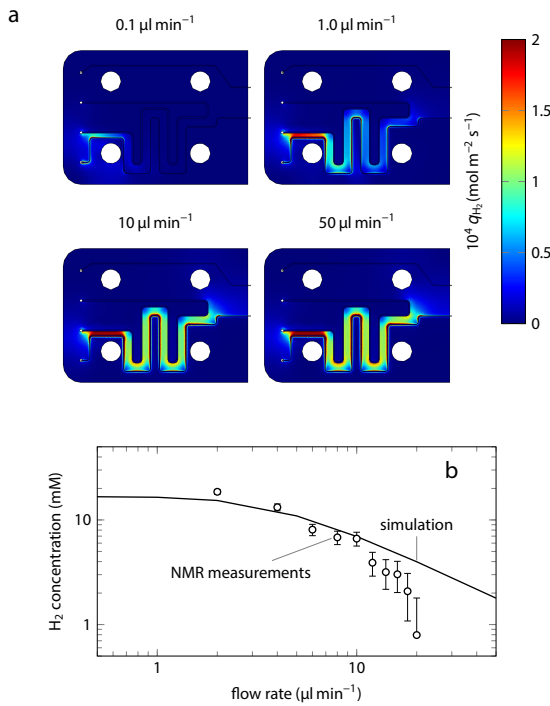


FIGURE 3.11: Finite element simulation of hydrogen uptake. a: Diffusive hydrogen flux in the PDMS membrane for different liquid flow rates; b: final hydrogen concentration in flowing methanol as a function of flow rate. Dashed line: simulation, open circles: NMR measurements.

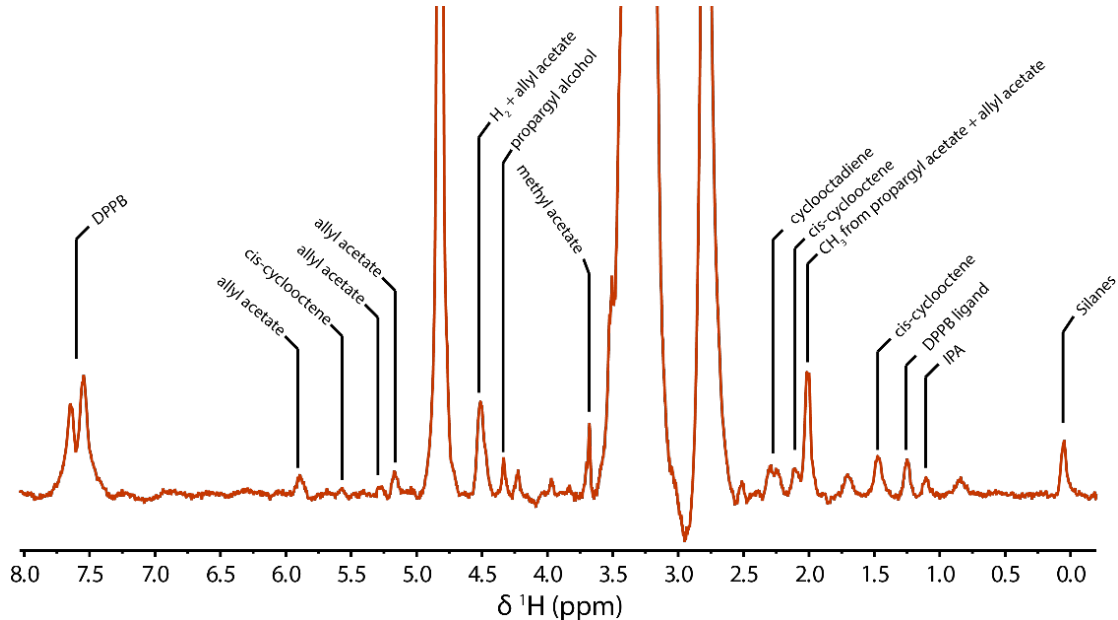


FIGURE 3.12: Labelled ${}^1\text{H}$ spectrum acquired using a flow rate of $2\mu\text{l min}^{-1}$ and a normal hydrogen pressure of 5 bar. The spectrum was collected using 64 transients with a delay of 5 seconds.

pressure at the gas/PDMS interface was set to a fixed value of 5 bar. Fig. 3.11a shows the diffusive flux of hydrogen through the PDMS membrane. Since the gas/PDMS interface acts as a source, and the liquid/PDMS interface as a sink for hydrogen, the flux is strongest where the two channels are in close proximity. At the lowest flow rate, significant transport only takes place in a very small area, and the liquid is saturated with hydrogen within the first few mm of the path which is in contact with the PDMS. The higher the flow rate, the further the area of significant flux extends downstream. At about 10 l min^{-1} , the hydrogen flux covers the entire length of the area between the liquid and gas channel interfaces. The finite element model also predicts the resulting concentration of hydrogen in the liquid (methanol) as a function of flow rate. This is shown by the solid line in Fig. 3.11b. The circles represent NMR measurements. At flow rates between 2 and 10 l min^{-1} , experimental results are in good agreement with the simulation. At higher flow rates, however, the experimentally observed hydrogen concentrations are significantly lower than the predictions. It is currently unclear what causes this discrepancy; possibly high flow rates lead to deformation of the PDMS layer over the liquid channel and thus change the uptake geometry. At flow rates below 10 l min^{-1} , the simulation and experiments both indicate that the flowing solvent is nearly saturated with hydrogen. Detailed information on the finite element simulations, as well as data on parahydrogen partial pressure throughout the chip is given in the supporting information.

3.6.5 Sensitivity and Limit of Detection

Clearly, the steady-state signals observed at constant flow rate are the result of a dynamic equilibrium between the rate of hydrogenation, the rate of transport of the hydrogenated product to the sample chamber and its removal from it, and spin-lattice relaxation. In order to probe the interplay of these factors, the NMR signal was suppressed by saturating the spin populations with a train of 512 $\pi/2$ pulses separated by $100 \mu\text{s}$ delays. The signal intensity was then measured as a function of the delay between the end of the saturation train and the NMR excitation pulse. Fig. 3.13a shows an example of the data thus obtained at a flow rate $q = 8 \text{ l min}^{-1}$. The signal increases rapidly after saturation, reaching steady-state levels after about 10 s.

The intensity of the steady-state NMR signal exhibits a clear maximum with flow rate (Fig. 3.13b), reflecting a balance between hydrogen uptake, reaction kinetics, and spin-lattice relaxation. The optimum, with the largest signal at saturation, is reached at a flow rate of $8 \mu\text{l min}^{-1}$. The nature of the stationary state established in the system at each flow rate becomes clearer if the saturation recovery data is plotted in terms of the volume displaced during the saturation recovery time $q\tau$, rather than the recovery time itself, and normalised to the steady-state signal intensity at each flow rate, as shown in Fig. 3.14. At flow rates below the intensity maximum at $q < 8 \text{ l min}^{-1}$ (solid circles in

Fig. 3.14), the data points collapse onto a curve that shows an initial linear increase up to a displaced volume of about $1 \mu\text{l}$, followed by rapid saturation to the steady-state value. This initial linear behaviour clearly indicates that the signal recovery in this regime is dominated by the convective fluid transport. This means that at these flow rates, a constant concentration of hyperpolarised material is established in the flowing liquid upstream of the sample chamber, and this is simply carried back into view of the NMR detector after the saturation pulses end. The maximum signal is reached after a volume of about $1.5 \mu\text{l}$ has been displaced. This is less than the capacity of the sample chamber, reflecting the uneven velocity distribution inside it. At flow rates above the optimum ($q \geq 8 \text{ l min}^{-1}$), a somewhat different behaviour is observed. The initial recovery rate is faster (Fig. 3.14, open circles), and appears to follow an exponential rather than linear shape. This suggests that at these flow rates, the stationary state is not yet established at the point where the liquid enters the sample chamber, and therefore, the observed recovery is dominated by the ongoing hydrogenation reaction.

In order to determine the sensitivity of detection of the hydrogenation product at the optimum flow rate, the experiment was repeated using normal hydrogen. In this case, the signal from protons A and B of the hydrogenation product are too weak to be observed above the noise in a single scan. Fig. 3.13d shows the averaged signal of 512 transients. Since the methyl group in the precursor and the hydrogenation product contribute to the same signal at 2.05 ppm , this signal can be used as a calibration standard, with a concentration of 20 mM which is unaffected by the hydrogenation reaction. By comparing this integral to that of the signal from the A protons, the concentration of hydrogenated product can be quantified. At a flow rate of 8 l min^{-1} , an allyl acetate (product) concentration of $(0.29 \pm 0.05) \text{ mM}$ was found, corresponding to a total of $(0.725 \pm 0.125) \text{ nmol}$ in the 2.5 l sample volume.

This quantity can be used to determine the limit of detection of the hyperpolarised product. The signal/noise ratio (SNR) in the spectrum shown in Fig. 3.13c is $400(\pm 10\%)$, and the line width is $6 \pm 0.5 \text{ Hz}$. The normalised limit of detection is given by Eqn. 1.113

$$\text{nLOD}_\omega = \frac{3n}{\text{SNR} \sqrt{\Delta f}},$$

where n is the amount of sample and Δf is the signal bandwidth. In the present case, one finds $\text{nLOD}_\omega = (2.2 \pm 0.4) \text{ pmol} \sqrt{\text{s}}$. Limits of detection in this range have so far only been reported in very limited circumstances, including chemically-induced dynamic nuclear polarisation (CIDNP) [165], or by making use of unconventional detection systems such as force-detected magnetic resonance or optical detection methods. Here, conventional inductive detection is used, and retains the full resolution and specificity that make proton NMR spectroscopy such a powerful analytical tool.

The mass limit of detection (LOD) for protons at a magnetic field of 14.1 T (corresponding to a proton Larmor frequency of 600 MHz) in state-of-the-art commercial

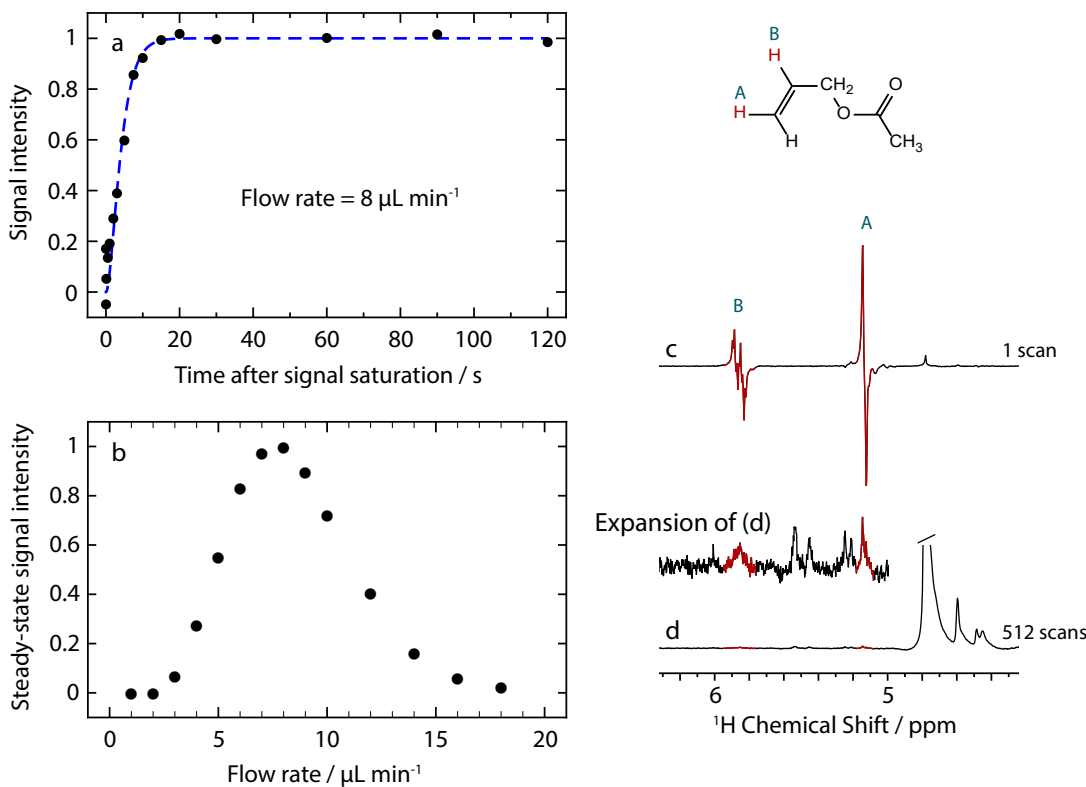


FIGURE 3.13: Saturation recovery results. a: signal buildup at constant flow rate after saturation; b: magnitude of the steady-state signal after full recovery (at least 100 s after saturation) as a function of flow rate. A clear maximum at $8 \mu\text{l min}^{-1}$ is observed. c: single-scan steady-state spectrum obtained at the optimum flow rate with para-enriched H_2 ; d: spectrum obtained with hydrogen gas in thermal equilibrium. 512 transients have been averaged. Signal enhancement by PHIP was determined by comparing the integral of the positive lobe of signal A in spectrum c to the integral of the corresponding (purely absorptive) peak in spectrum d.

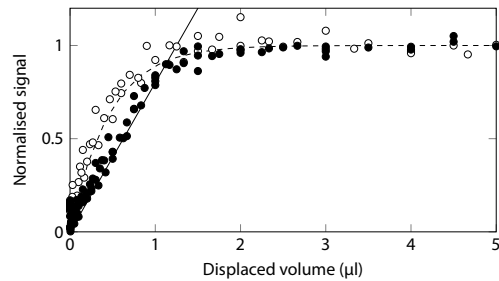


FIGURE 3.14: Signal recovery after saturation, normalised by the maximum signal observed at long recovery times. The horizontal axis is the volume moved through the chip during the recovery time τ_r , i.e., $q\tau_r$, where q is the flow rate. Filled circles correspond to flow rates below the optimum ($q < 8 \mu\text{l min}^{-1}$), whereas open circles are obtained at flow rates $q \geq 8 \mu\text{l min}^{-1}$. The solid and dashed lines are guides to the eye for the solid and open circle data points, respectively.

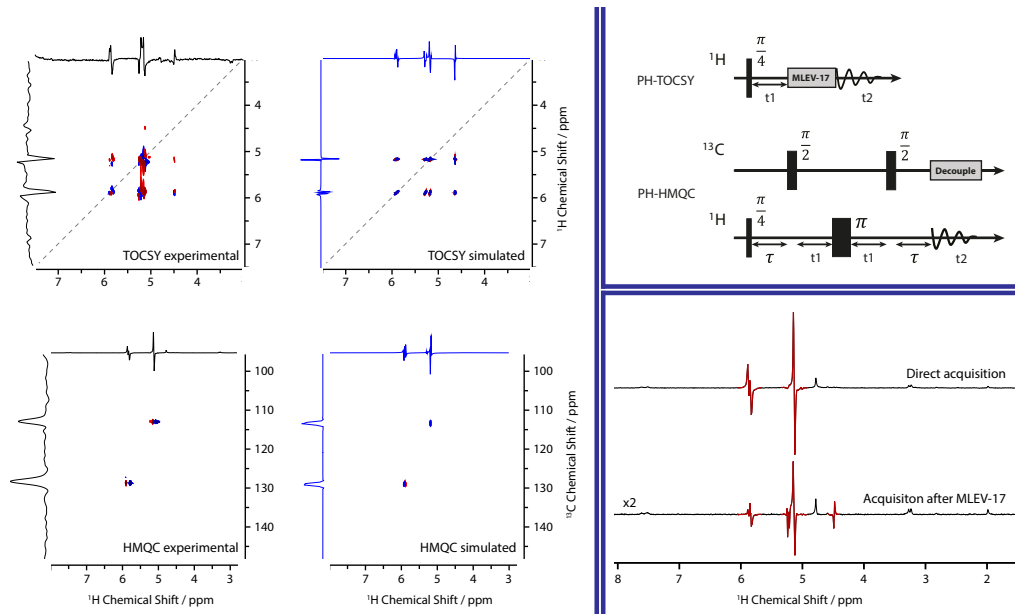


FIGURE 3.15: The continuous flow PHIP@chip approach allows acquisition of two-dimensional spectra with very high sensitivity. Left pane: experimental 2D NMR spectra of the hyperpolarised reaction mixture, flowing at $8 \mu\text{l min}^{-1}$, along with simulations (right). The diagonal in the TOCSY spectrum is marked by a dashed grey line. Only the protons originating from parahydrogen give signals on the diagonal; the polarisation is transferred to the other locations by the isotropic mixing sequence. The ^1H - ^{13}C HMQC spectrum shows two separate multiplets, each correlating one of the two hyperpolarised protons with the directly bonded ^{13}C spin. The ^{13}C traces in the HMQC spectrum are shown in absolute mode. Right pane (top): Pulse sequences used to acquire TOCSY and HMQC spectra. Right pane (bottom): 1D ^1H spectrum obtained directly after a single $\pi/4$ pulse (top) and after applying the MLEV-17 isotropic mixing sequence (bottom). This demonstrates that the hyperpolarisation can be spread throughout the J -coupling network.

NMR probes with a conventional sample volume of 0.5 ml is approximately $100 \text{ nmol } \sqrt{s}$. Microfluidic NMR systems can make use of miniaturised NMR detectors, which benefit from a favourable scaling of the mass sensitivity with detection volume [108, 2, 61]. At a size scale of $2.5 \mu\text{l}$, a mass sensitivity around $1 \text{ nmol } \sqrt{s}$ has been reported [17]. However, due to the limited volume in such systems, the *concentration* sensitivity is very poor, such that only compounds present at mM levels can be quantified in microfluidic NMR systems. This situation gets worse as the detector volume decreases. By contrast, many samples of interest, such as metabolites in microfluidic culture systems, are only present at μM levels.

In the present case, the concentration limit of detection from Eqn. 1.114 is

$$\text{cLOD}_\omega = \frac{n\text{LOD}_\omega}{V} = (0.88 \pm 0.16)\mu\text{M}\sqrt{s}. \quad (3.23)$$

From the ratio of the signal intensities in the thermal and hyperpolarised spectra shown in Fig. 3.13c and d, it is possible to estimate the ^1H polarisation levels. In the thermal spectrum, the SNR is about 5:1, whereas it is 400:1 in the hyperpolarised spectrum.

The thermal spectrum is obtained from 512 transients, therefore the single transient thermal SNR would be $5/\sqrt{512} \approx 0.22$. This leads to a signal enhancement factor of $\epsilon \approx 400/0.22 \approx 1800$.

This can be compared to the expected signal enhancement given the enrichment level of para-hydrogen used in the experiment. The ideal enhancement factor is given by

$$\epsilon_{id} = \frac{4x_p - 1}{3\sqrt{2}} \frac{2k_B T}{\hbar\gamma B_0}, \quad (3.24)$$

where x_p is the mole fraction of parahydrogen in the feed gas, γ is the magnetogyric ratio, B_0 is the magnetic field, and \hbar and k_B are Planck's and Boltzmann's constants, respectively. At a temperature of $T = 298\text{K}$ and a magnetic field of 11.7T , and with $x_p = 0.5$, this yields $\epsilon_{id} \approx 6100$, which is a factor of 3.5 larger than the experimentally observed enhancement factor. We can therefore conclude that about 2/3 of the theoretically available spin order is lost to relaxation under the present experimental conditions.

3.6.6 2D NMR

A great advantage of the continuously operating microfluidic PHIP system is the ability to acquire many transients in succession under virtually unchanged conditions. This is difficult to achieve with bubbling hydrogen through a solution. As a consequence, hyperpolarised multi-dimensional NMR spectra[166, 160, 158, 161, 162, 167]. have been recorded either using automated reactors combined with NMR flow probes,[161, 162] or using ultrafast acquisition techniques[166, 160, 167].

The PHIP@chip setup allows straight-forward acquisition of 2D spectra, using conventional t_1 incrementation. To demonstrate this, 2D TOCSY (Total Correlation Spectroscopy) and HMQC (Heteronuclear Multiple Quantum Coherence) NMR spectra of the reaction mixture at a flow rate of $8\text{ }\mu\text{l min}^{-1}$ were collected. The pulse sequences were modified by replacing the initial $\pi/2$ pulse with a $\pi/4$ pulse, and are referred to as “PH-TOCSY” (parahydrogen TOCSY) and “PH-HMQC” (parahydrogen HMQC) in Fig. 3.15. In the text they will henceforth simply be referred to as “TOCSY” and “HMQC”.

A TOCSY spectrum acquired in 20 min is shown in Fig. 3.15, alongside a simulated spectrum and the pulse sequence, which deviates from the standard TOCSY sequence only in the initial pulse. The acquisition parameters are given in 3.5

We would expect a *thermal equilibrium* TOCSY spectrum of this compound to contain diagonal peaks connecting the identical nuclear spins in the two acquisition dimensions, and off-diagonal peaks connecting J -coupled spins. In this *hyperpolarised* experiment, the diagonal peaks only appear for the two parahydrogen proton signals, because they are the only spins significantly polarised in the direct detection dimension. The other

protons are only polarised during the isotropic spin-mixing step of the pulse sequence, and hence don't appear in the direct dimension. These protons only produce off-diagonal peaks, connecting them to the parahydrogen pair.

An HMQC spectrum acquired in 60 min is shown in Fig. 3.15, alongside a simulated spectrum and the pulse sequence, which deviates from the standard HMQC sequence only in the initial pulse. The acquisition parameters are given in 3.5

The HMQC spectrum shows two peaks, linking the parahydrogen protons to the ^{13}C spins to which they have a direct $^1J_{\text{CH}}$ coupling. This is supported by the simulated spectrum. An experiment of this kind, in which signals are detected at full natural abundance of the ^{13}C spins (about 1%) in a $2.5 \mu\text{l}$ detection volume, is only possible due to both the high polarisation levels and stability of the system.

The results in Fig. 3.15 show that the hyperpolarised spin order can be spread to other protons in the molecule by the application of the isotropic mixing sequence MLEV-17 prior to 1D signal acquisition. This simple trick allows one to hyperpolarise any protons that are J -coupled to the parahydrogen pair, which makes the technique more general.

Much ongoing research in the field of hyperpolarisation is motivated by in-vivo applications, where hyperpolarised compounds are used as magnetic resonance imaging contrast agents [168]. Mostly, this involves transferring the nuclear spin polarisation after hydrogenation to other nuclei (^{13}C , ^{15}N , ^{31}P) with lower magnetogyric ratios, where spin-lattice relaxation times are longer. [169, 170, 155] Many of these approaches use zero or very low magnetic fields for hydrogenation and polarisation transfer. This has the advantage that near magnetic equivalence between the two added protons is maintained through the reaction, leading to longer lifetimes [151, 152, 153, 154, 155, 156, 171, 172]. The present work opens a complementary strategy, in that the hydrogenation is done at high field. Deleterious effects of relaxation are minimised by the proximity of the site of hydrogenation to the point of use. Arguably, this approach has advantages in the context of microfluidic systems, where only small quantities of hyperpolarised agents are needed.

3.7 Conclusions

The combination of a highly efficient transmission-line NMR micro detector with parahydrogen-induced hyperpolarisation leads to an unprecedented sensitivity in inductively detected NMR, with a mass limit of detection around $2.2 \text{ pmol} \sqrt{\text{s}}$. This corresponds to a concentration sensitivity of less than $1 \mu\text{M} \sqrt{\text{s}}$, which, to our knowledge, has not previously been reached at the volume scale of $2.5 \mu\text{l}$. This opens the perspective to be able to study chemical processes involving low-abundance species in mass-limited samples. Obviously, such applications require preparation of a hyperpolarised reactant. As the foregoing

study shows, the necessary chemistry can be integrated in a microfluidic system. It should be noted that the parahydrogen used here is enriched to 50% (compared to 25% at thermal equilibrium); the sensitivity could easily be boosted by a factor of three by using pure parahydrogen. Microfluidic systems hold great potential in combination with hyperpolarised NMR. All hyperpolarisation techniques require coordinated manipulation of fluids and spin transformations. The results shown in the foregoing demonstrate that in the case of parahydrogen-induced polarisation, this can be assisted considerably by integrating some of the necessary chemical steps on a microfluidic chip. Parahydrogen can be delivered to a reactive solution through a PDMS membrane at sufficient rate to achieve significant levels of hyperpolarisation; dissolution and transport of hydrogen in PDMS does not appear to lead to significant ortho-para equilibration. The highly stable continuous operation of the PHIP@chip system allows quantitative studies of the hydrogenation kinetics, and the relevant relaxation processes. This is demonstrated by the dependence of the steady-state signal intensity on flow rate (Fig. 3.13b, and the recovery of the hyperpolarised signal after saturation (Fig. 3.13a)).

The successful demonstration of PHIP on a chip opens important perspectives. Conditions can be optimised for continued production of hyperpolarised metabolites, which opens the possibility to conduct *in-situ* metabolic studies in microfluidic cultures of cells, tissues, and organisms. While the hyperpolarised compound used here, allyl acetate, is not a metabolite per se, the production of hyperpolarised metabolic species through PHIP has been demonstrated before [156, 154, 173, 174, 175, 168]. Some metabolites, such as Fumarate [174], can be generated directly by hydrogenation of an unsaturated precursor. Aime et al. have proposed a more generally applicable method [173], which relies on the metabolite bound to an alkyne sidearm through an ester linkage. After hydrogenation, the polarisation is transferred to a ^{13}C nucleus in the metabolic moiety, and the sidearm is cleaved. PHIP@chip opens the possibility of implementing these additional production steps on the same chip. In turn, this may enable integration of the hyperpolarised metabolite generation with an on-chip culture of cells or other biological systems. Thanks to its stability, the setup provides a convenient means to optimise pulse sequences and reaction conditions for producing hyperpolarised targets.

Chapter 4

An NMR compatible on-chip Peristaltic Pump

4.1 Introduction

The flow and control of liquids in microfluidics is essential, with microfluidic pumping and mixing playing an integral role in many biological and chemical applications, such as DNA analysis[176, 177], protein folding[178], enzyme assays[179, 180], chemical synthesis[181, 182], and kinetic studies[183, 184]. Many solutions exist for the pumping and mixing challenge on small scales. These include 3D printed valves[185, 186], syringe pumps[187, 188, 189], pressure actuated valves[190, 191, 192], electrowetting (sometimes referred to as digital microfluidics[193, 194], piezoelectric pumps[195, 196], magnetic pumping[197, 198], and centrifugal forces[199, 200, 201]

In this chapter, the design and implementation of an NMR compatible, low dead volume microfluidic pump will be discussed. The aim of this is to be able to mix two fluids in a controlled manner inside an NMR magnet. It will involve having an on-chip reservoir that can be drawn from and mixed with whichever liquid that's under investigation. These aims are important as the technology will be useful in chemistry applications such as a chemical reaction study, kinetics study, or hyperpolarisation on chip. The pump will be useful in biological studies too with protein binding studies already being shown to be possible[202] these pumps could be used to do the whole experiment on chip. Cell and living tissue culture could also benefit from perfusion provided by the pump supplying them with fresh O₂ and nutrients. Ultimately, the goal is to observe active changes on the chip, induced by pumping, in real time, using NMR.

Pumps that integrate pumping ‘on chip’ are key to minimising the dead volume within the device. Unger and co-workers[7] were amongst the first to do this by using micro-fabricated PDMS valves using soft lithography. Fig. 4.1 shows the devices, these work

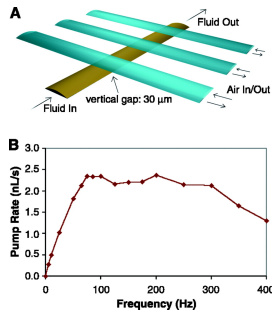


FIGURE 4.1: A) A 3D scale diagram of an elastomeric peristaltic pump. The channels are 100 μm wide and 10 μm high. Peristalsis was typically actuated by the pattern 101, 100, 110, 010, 011, 001, where 0 and 1 indicate “valve open” and “valve closed,” respectively. B) Pumping rate of a peristaltic micropump versus various driving frequencies.

this figure is reproduced from [7]

by having a fluid path that has various gas channels running perpendicular above. Then by simply applying air pressure, the gas channel expands cutting off the flow in the fluid path. When these are actuated in sequence it produces a net movement of fluid and flow rates of 2.5 nL/s were achieved.

Leslie et al[203] had slightly different approach, they used PDMS but in direct contact with the fluid. In the ‘pump’ the PDMS forms a dome above a circular structure in the fluid channel that is depressed using air pressure. In order to control the flow they use so called fluidic diodes, these work analogously with electric diodes, by only allowing fluid flow above a certain pressure in one direction only. These diodes are formed by having a weir that separates two fluid channels covered by a compliant PDMS membrane. When the internal fluid pressure reaches the threshold, this pushes the PDMS membrane up and allows fluid connection over the weir. The pressure required to open the diode depends on the thickness of the PDMS ceiling and is predictable which allowed control of flow in the chip at large.

There are challenges to enabling on-chip pumping in a high magnetic field to enable high resolution NMR spectroscopy. Firstly, the materials used should be compatible with a high magnetic field – this clearly rules out ferrous metals. This also rules out materials that have a significantly different magnetic susceptibility to that of the chosen fluid (in this case water) as described in chapter 1 and susceptibility mismatches need to be carefully managed or they will interfere with the homogeneity of the magnetic field and broaden the line which is essential for any high resolution NMR experiments. Secondly, materials chosen must also be conducive to rapid prototyping and as such must be cheap and readily available as well as be easily cut by a laser cutter and bonded using a simple method. These reasons rule out glass, a common microfluidic material, as it is not easily bonded or cut using a standard laser cutter. Thirdly, the chip when fully assembled should not be more than 1 mm in thickness due to the strip-line probe geometry preventing this meaning that the glass would be too fragile for continuous

insertion into the probe and magnet. Lastly, the device should be able to seal against gas and liquid pressures whilst in operation inside the magnet.

With all these limitations another material one might suggest is PDMS. It's cheap and readily available; easy to cut and bond; and can be made into 1 mm layers to fit the transmission line probe. However, due to its amorphous structure the ^1H background signal is large and broad across the range of ppm that our signal that we are interested in appears. This makes it impractical to suppress and any suppression would also suppress the signals that we are interested in and what lead to difficulties in quantification of substances present in the mixture of interest.

In the design shown, a PDMS layer is still used. However, it is removed from the sensitive area around the sample chamber so that it does not interfere with the signal collected from the device. The 3D printed parts role here is three-fold. Firstly, it acts as a conduit for delivering liquids and transporting them around the device. Secondly, it allows for the pressurised air to be delivered which drives the pneumatic valves and enables pumping. Lastly, when screwed together, the 3D printed parts form a seal against liquid and gas leaks.

Nuclear magnetic resonance (NMR) is an ideal tool with which to study live systems which, owing to its non invasive non destructive nature, can give insight into living systems *in situ* and allows for longitudinal studies of these. However, in order to keep these systems alive they need fresh supplies of oxygen and nutrients in order to truly replicate *in vivo* conditions. One way of achieving this is by perfusion of liquid that has been exposed to fresh supplies of oxygen. This can be achieved by pumping liquid through the microfluidic device and then out to a reservoir that is in contact with a supply of oxygen. This method would, however, dilute any metabolites given off by the living system that one is trying to study within the device and since the biggest limitation of NMR is sensitivity it is pertinent to avoid this. This means that the pump would ideally be integral to the device itself. This could reduce the overall volume of the system to 10s of microlitres which is much better than the 10s of millilitres that come from having an external pumping network. This means that the pump would ideally be integral to the device itself. This could reduce the overall volume of the system to 10s of microlitres which is much better than the 10s of millilitres that come from having an external pumping network.

In summary, the device must meet the following criteria:

- Non-magnetic, susceptibility matched
- Easily fabricated using rapid prototyping
- Low dead volume
- Biocompatible

- Geometry compatible with transmission line probe.
- Easily assembled and operated *in situ*

The solution employed here, shown in Fig. 4.5, involves a multilayered PMMA device with two PDMS membranes sandwiched between two 3D printed holders held together with brass screws. The PMMA device houses the structures for the valves as well as the fluid circuits including an NMR sensitive sample chamber and on-chip reservoir. The PDMS layers have two separate functions, the top membrane forms the valves with the PMMA structures whilst the bottom membrane acts as an o-ring to seal against liquid leaks. The 3D printed holders are also multi purpose. The top holder forms the last part of the valves by sealing the PDMS-PMMA valve and allowing the delivery of pneumatic pressure through the bore of the magnet to the device. The bottom 3D printed holder allows the device to be filled and supplys external ports for fluid short circuiting. Together, they help seal the device against gas and liquid leaks. This device coupled with a bespoke, homebuilt probe enables pumping and observation by NMR in a microfluidic device.

4.1.1 Materials and Methods

The devices were composed of three layers of cell cast Polymethyl methacrylate (PMMA, Weatherall Equipment). The sheet thickness was 200 m for the top and bottom layers, and 500 m for the middle layer. The channels and sample chambers were designed in AutoCAD and cut using a CO₂ laser (HPC Laser ltd.) to an approximate width and depth of 150 m. These layers were bonded together using plasticiser (2.5% v/v dibutyl phthalate in isopropyl alcohol) and subjected to heat and pressure (358 K, 18.6 MPa). To seal the devices, two polydimethyl siloxane (PDMS, Shielding Solutions) were designed in AutoCAD and cut using the same laser as the PMMA layers.

The PMMA and PDMS were screwed together and held in place using 3D printed devices designed in SolidWorks (Acura Xtreme, ProtoLabs). These, as shown in Fig. 4.5, seal the device whilst enabling the filling of the device as well as delivering the pressurised air for the peristaltic pumping.

Firmware for controlling the peristaltic pump was written in Arduino and is in the supplementary information. This has the ability to put the pump into 3 states “advance”, “mixing” and “quiet”. The “advance” state pumps from the outside loop of the device to the inside loop for a desired number of seconds; “mix” pumps around the inner loop for a desired number of seconds; and “quiet” stops all pumping and leaves all valves open indefinitely.

The hardware for controlling pumping comprised of a solenoid valve system with 8 individual valves (Festo, RS). These were connected to 3mm plastic tubes (Festo, RS)

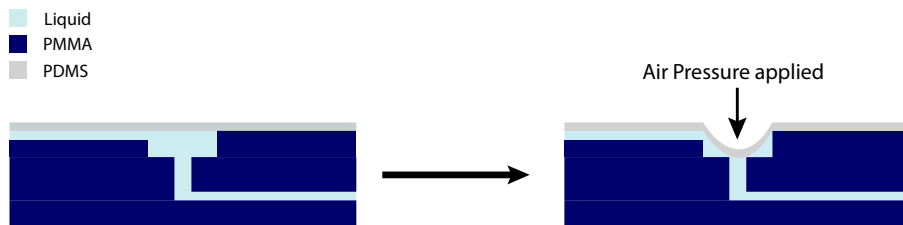


FIGURE 4.2: A cut-through view of the valves in the device showing how when air pressure is applied the PDMS membrane is pushed down and seals the small hole cut in the middle layer.

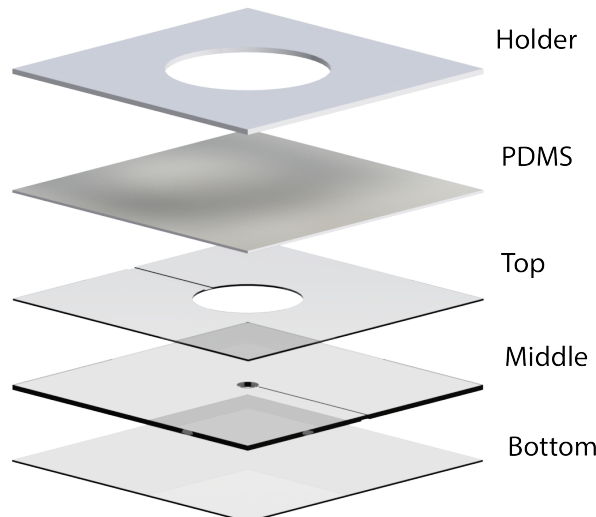


FIGURE 4.3: 3D render of a single valve with 3D printed layer shown too

and all supplied from an in-lab air pressure source. This valve system was connected, via a solderless breadboard, to an arduino (Mega 2560, RS) controller allowing for individual control of each of the valves. The Solenoid valve system was powered using a 24V supply.

The device was put into a transmission line based home-built probe. In this, the device is held between two striplines with the inner sample chamber lining up with the constriction on the strip-lines. NMR measurements were performed on a bruker AVANCE III spectrometer and 11.7 T magnet. Spectra were collected using 64 scans using a 90 degree pulse length of 2.5 us at 50 W of power. Water suppression was achieved by using presaturation with 5×10^{-4} W.

100mM solutions of sodium acetate (Merck) and 3-(Trimethylsilyl)-1-propanesulfonic

acid (DSS, Merck) by dissolving 82 mg and 196 mg in 10 ml of deionised water (ReAgent) respectively. The two fluidic loops were then filled with these separately and the in/out ports short circuited.

4.2 Results and Discussion

4.2.0.1 Peristaltics

In order for the dead volume in the device to be kept at a minimum, the valves should be implemented in the fluid path on the device itself. Shown below in Fig. 4.2 is the basic principle behind the design.

In the device, there are valves cut into the layers of PMMA. These are formed by two holes in the top and middle layer. The hole in top layer has a radius of $500\mu m$ whilst the hole in the middle layer has a radius of $100\mu m$. The top layer has a channel (approx. $100\mu m$ in width and depth) scored into it to deliver fluid to the top chamber whilst the middle layer has a similar channel scored on the under-side to carry fluid away. When covering the hard PMMA structure with the more compliant PDMS membrane of $250\mu m$ thickness and applying air pressure from above one seals the valve by covering the hole in the middle layer.

A 3D rendering of a single valve is shown in Fig. 4.3 and shows the ratio of pump holder opening, top hole; and middle hole respectively. The central principle of these valves are the differing side that the scored channels are on.

In Fig. 4.6, micrographs of the chip outside the holders are shown with the valves where one can see the fluid channels on opposing side of their respective layers. Also given, is side by side comparison of the same valve (valve 2 in Fig. 4.4) open (2) and closed (3) one can see the 'ring' formed by the PDMS as it seals against the middle layer.

In my design, there are 6 such valves all individually addressable with air pressure that, when coupled with home-written Arduino firmware, can be actuated in sequence in order to move fluid in a given direction. The block diagram of the arduino set-up is shown in Fig. 4.7. By varying the frequency and lambda parameters, listed in the firmware, one can control the liquid pumped in a given time.

As well as 6 valves the chips also have two separate liquid circuits that can be connected externally by connecting tubes to the top of the 3D holders as shown in FIG. The inner circuit on the diagram comprises the pumping network which can be modified to pump around the internal circuit or the complete network; and an NMR sensitive sample chamber where measurements are performed. The external circuit, contains an identical sample chamber that helps to keep the relative volumes of the two circuits similar. The chip is filled from the 'bottom' using the 4 small access holes at the top of

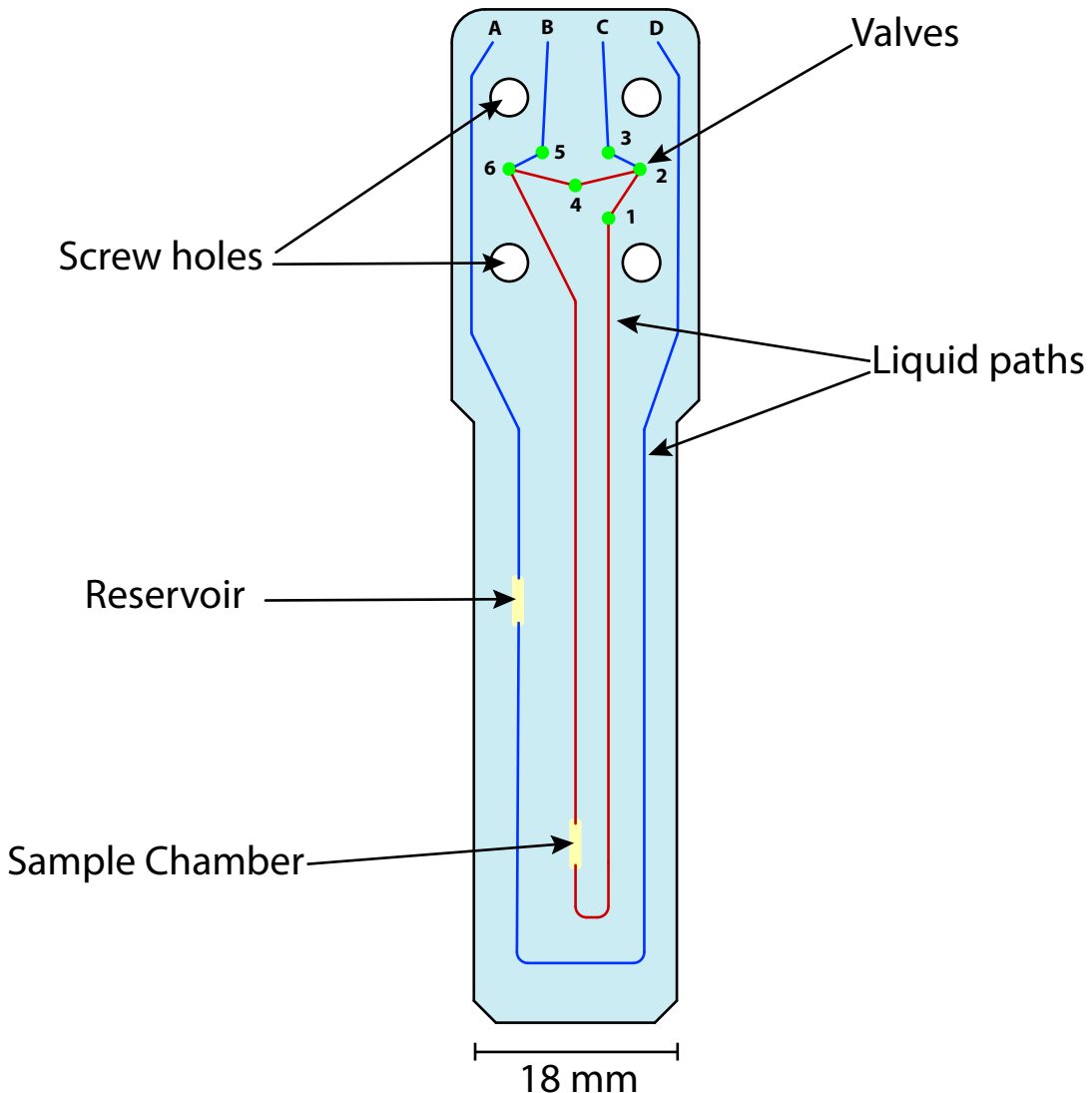


FIGURE 4.4: A CAD drawing of the chip designed for pumping and mixing. Inner (red) and outer (blue) liquid circuits; liquid ports (A-D) and valve positions (1-6) shown

the chip. This then allows the valve network and pressurised air to be on the top side of the chip. The challenge in the chip was to fit all the liquid paths and valve network around the 4 large screw holes in the top of the design which accomodate the screws neccesary to hold the device together and seal against leaks of both liquid and gas.

4.2.0.2 Characterisation of flow

Characterisation of flow experiments where performed with the device in “open” configuration. This means that after the device was screwed together the two circuits shown in blue and red were joined together by fixing tubing between the A and B ports shown

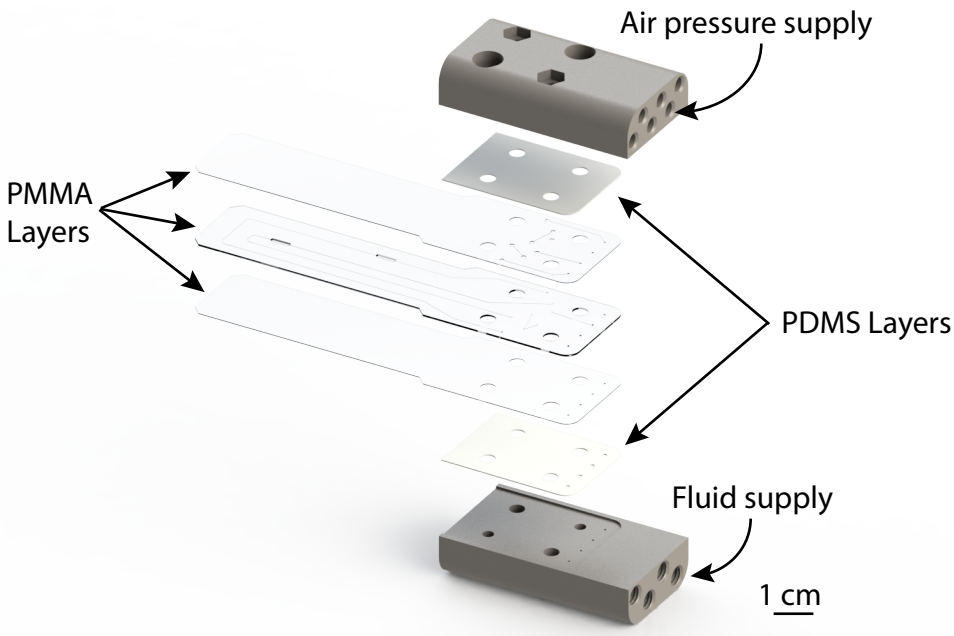


FIGURE 4.5: A 3D representation of the device with separate layers of chips and PDMS layers shown.

in Fig. 4.4. This left C to be “in” and D to be the “out” port with valves 3, 2, and 1 being actuated in sequence to pump and valve 4 sealed.

The device was connected to translucent polytetrafluoroethylene (PTFE) tubing (Outer diameter 1.6 mm, inner diameter 0.8 mm) with one end submerged in a 500 mL beaker containing filtered DI water (Reagent). Next to the device a ruler was secured to the bench top with the tubing fixed parallel to it. The pump was then switched on and the device allowed to draw water and pump out the other side. When the meniscus reached the tubing next to the ruler a timer was started and the distance along the ruler was recorded every minute for 10 minutes. This was repeated 3 times for frequencies from 0.25-1 keeping the lambda constant at 3, which had shown through trial and error to be the optimum number.

The graph shown in Fig. 4.8 is the result of plotting the cumulative volume pumped vs. time. All 4 frequencies show very little deviation from linearity (quantify) in the long term and also show very small error bars (plotted as ± 2).

In Fig. 4.9, the flow rate of the pump at varying frequencies is plotted. This shows that the rate doesn’t linearly depend on frequency and seems to level off at higher frequencies. When initially observing the slope of the lines in Fig. 4.8 the non-linearity was attributed to inconsistencies in the tightening of the screws in the device. However, the small error bars associated with the flow rates across three separate experiments

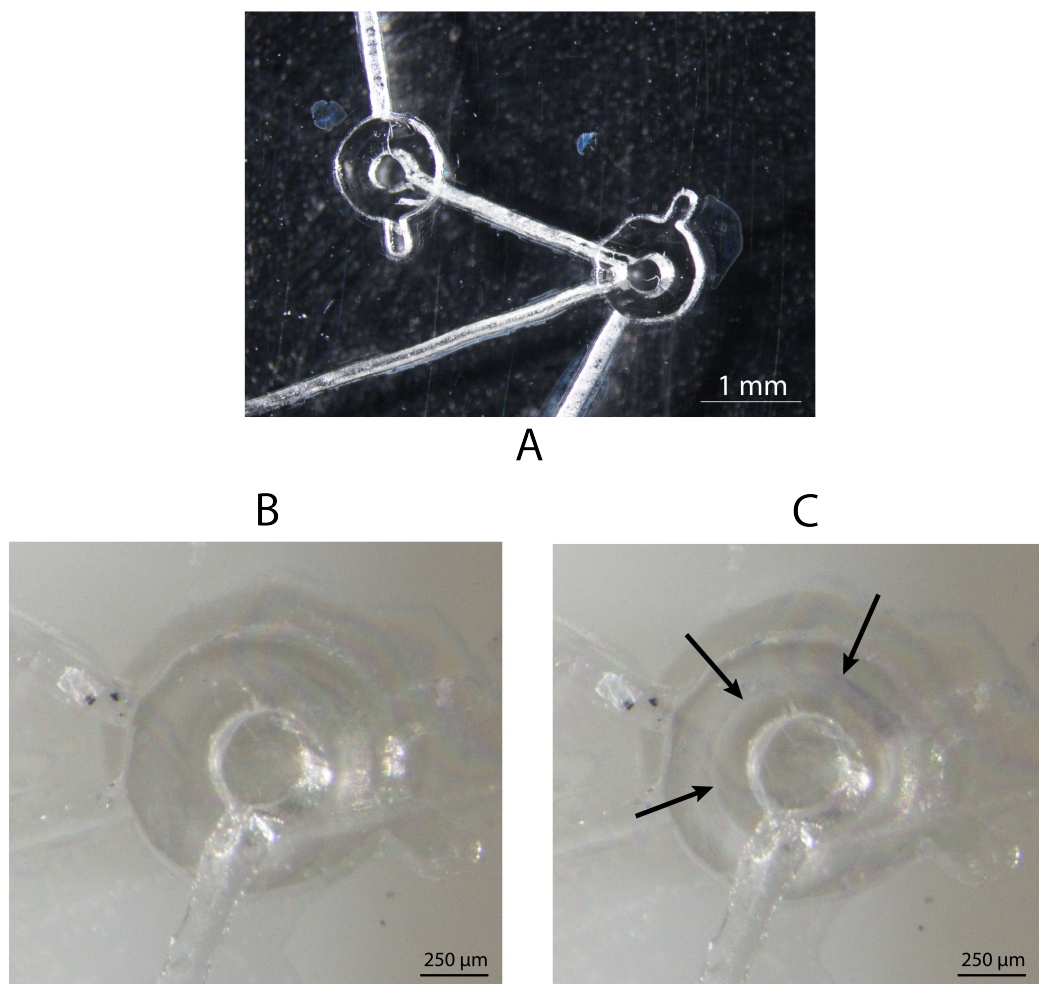


FIGURE 4.6: Micrographs of A: free chip showing two valves B: An assembled device with an open valve C: An assembled device with a closed valve, the arrows indicate the area where the PDMS is in contact with the PMMA and is sealing the hole.

each with at least one disassembly it is known thought that the limit of the pump rate is related to the elasticity of the membrane and how fast it's able to 'snap back' and re prime itself to pump in each valve.

4.2.1 *In situ* operation of the device

In order to validate the pumps compatibility with NMR, the device was placed into a home built transmission line probe inside a 500 MHz magnet. The arduino controller and solenoid valve bank were secured outside the magnet and the 6 pressurised air lines fed in to the top of the magnet. The device was then filled with 100mM sodium acetate in DI water (Sigma Aldrich) in the inner circuit by attaching a syring to inlet **B** in Fig. 4.4. 100mM DSS in DI water (Sigma Aldrich) was added to the outer circuit by syringing into inlet **A**. Such that all the initial signal should come from the sodium

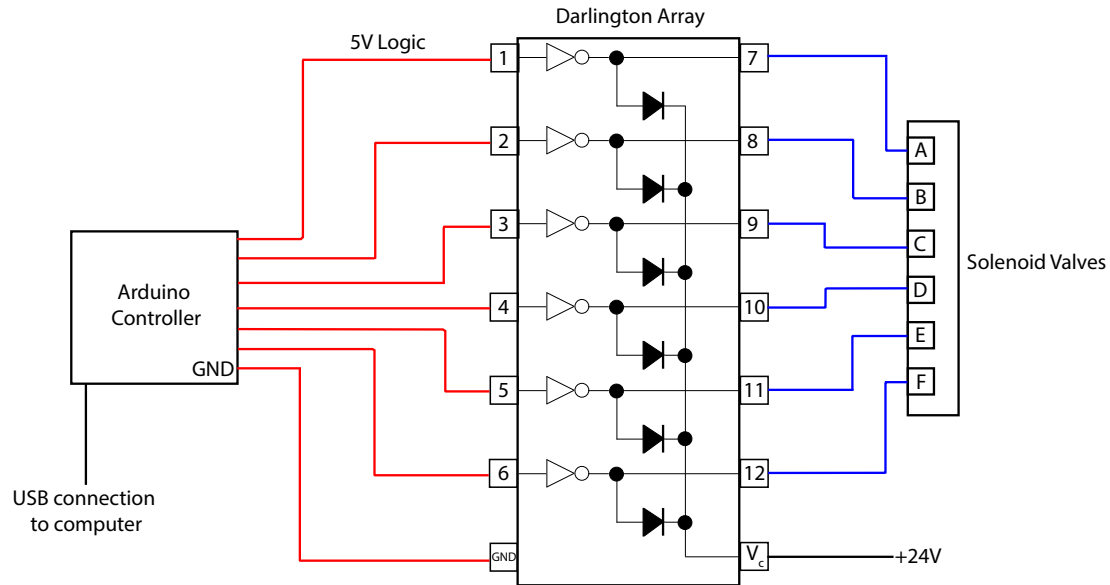


FIGURE 4.7: An arduino controller is connected to, and powered by, a laptop via USB. The controller is connected to a darlington array via six 5V logic connections (shown in red) when addressed, these allow the corresponding pin opposite to draw power from the +24V connected from an outside source. The blue lines indicate the the wires carrying 24V to the solenoid bank which are pneumatically connected to the valves in the chip as labelled.

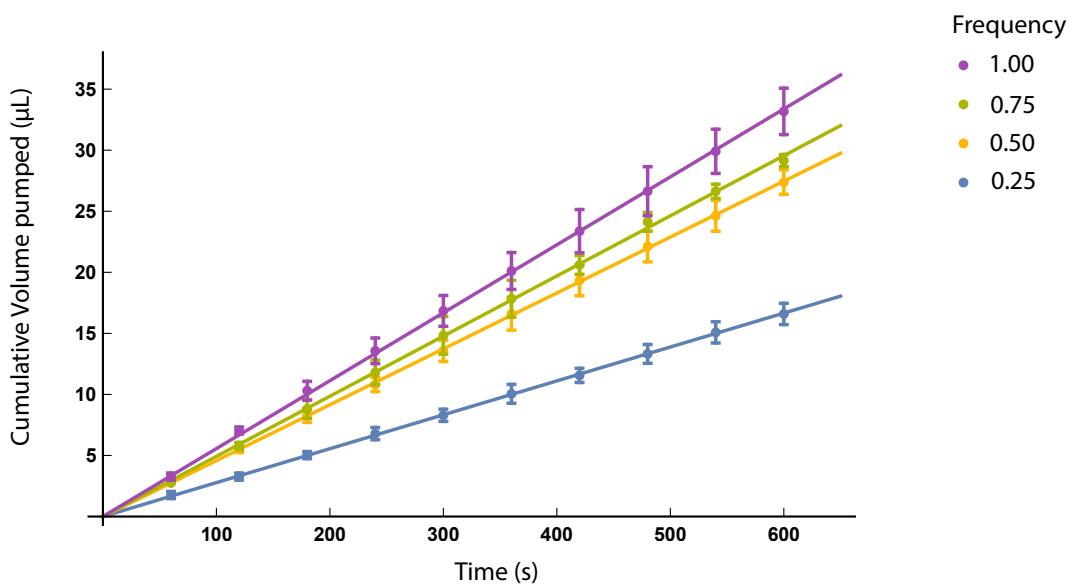


FIGURE 4.8: Plot of the total volume pumped vs time for a chip in the open configuration

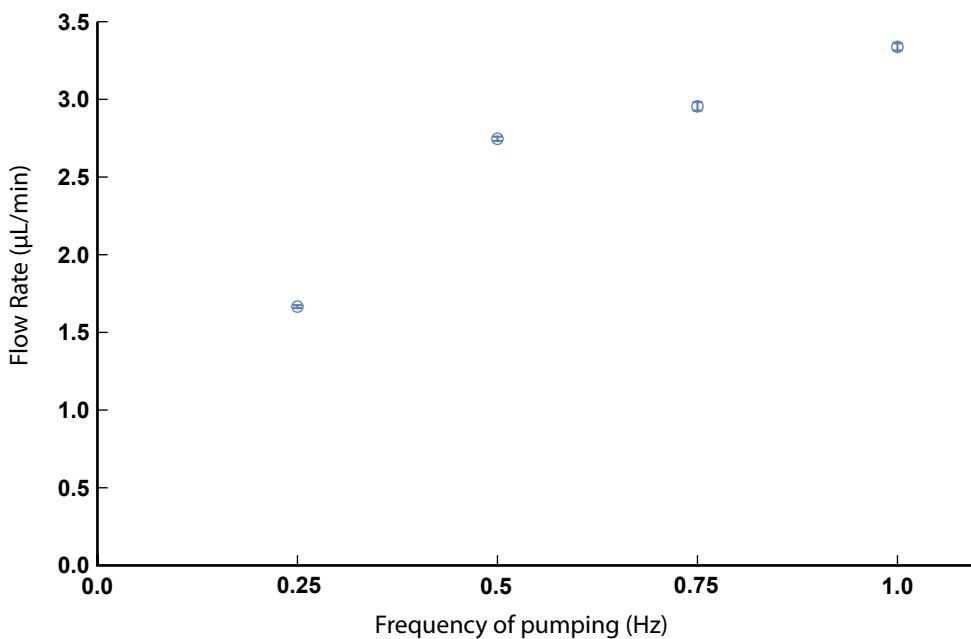


FIGURE 4.9: Flow rates produced by the pump at different frequencies.

acetate solution. The two fluid networks were then connected using two short lengths of 1/16" outer diameter PTFE tubing by joining **A** to **B** and **C** to **D**.

First a spectra was collected of the chip after filling, A in Fig. 4.10, using 16 transients and shows mainly the acetate signal at 1.9 ppm. The pump was then put into the 'advance' state for 120 seconds which mean the valves are actuated in order to pump liquid around both circuits. The pump then mixed in the inner circuit for 120 seconds and a second spectra was recorded, B. This shows the 4 signals typical of DSS at 2.91 ppm, 1.75 ppm, 0.63 ppm and 0 ppm and very little acetate signal. Indicating that the volume inside the NMR sensitive area has been almost entirely exchanged. Lastly the pump again advanced and mixed for the same time as before producing the spectra shown in C. Again, this spectrum is different. It shows all signals expected in abundance. This points to mixing of the two substances facilitated by the peristaltic pump and serves as proof, at least in principle, that an NMR compatible microfluidic peristaltic pump capable of mixing liquids in a controllable manner has been presented here.

4.3 Conclusions

In conclusion, an NMR compatible; low dead volume microfluidic pump has been designed and manufactured that works inside the bore of a high field magnet. The pump

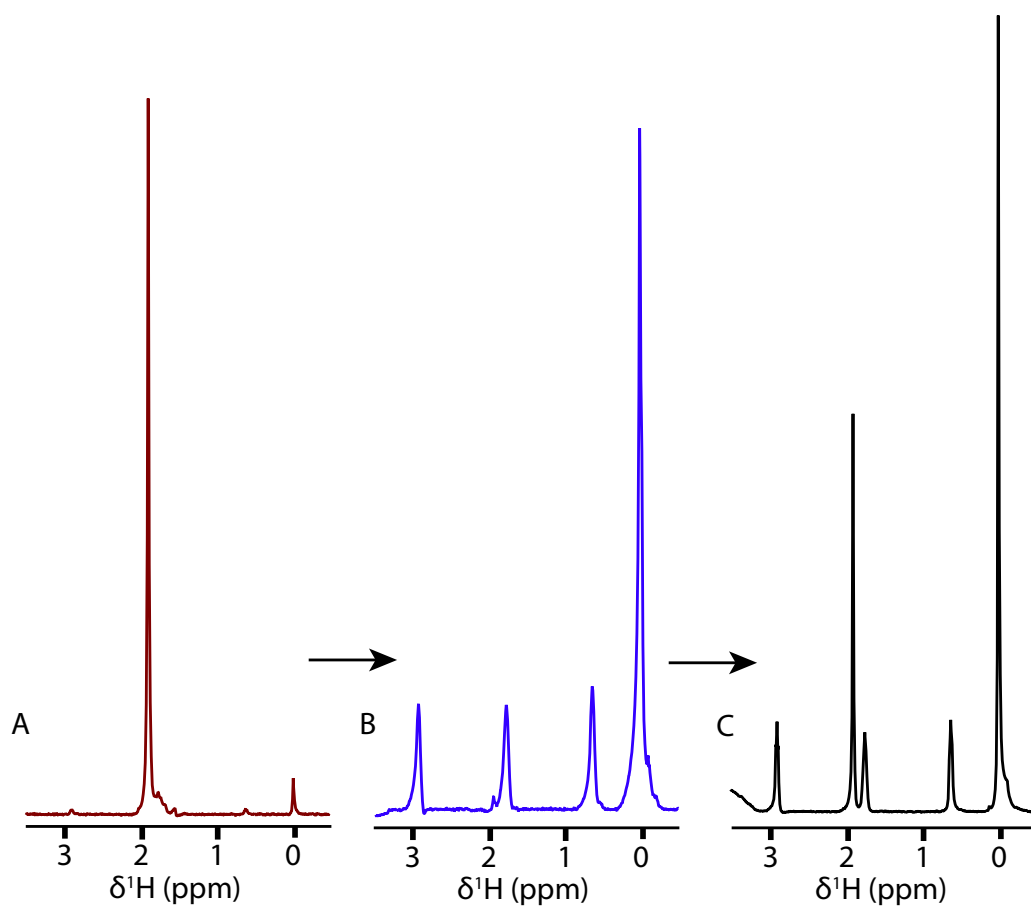


FIGURE 4.10: NMR spectra recorded with 16 transients on a device containing 100mM Sodium acetate in the inner circuit and 100mM DSS in the outer circuit.

has shown excellent linearity (quantify?) and stability in the long term as well as performing exchange and mixing of two substances within the device inside a high field magnet. The present limitations are that precise volume control has not yet been achieved. This is, however, thought to be linked with the varied tightening of the screws of the 3D holder as well as the presence of bubbles within the device. Another element that requires further probing is the non-linear dependence of flow rate on frequency. My intuition is that this depends on the thickness of the PDMS layer used however further experimentation with varying thicknesses is needed. Potential future applications of this pump include microfluidic protein binding experiments; *in situ* liver slice culture and metabolomics; and hyperpolarisation experiments.

Bibliography

- [1] M. Sharma and M. Utz, *Journal of Magnetic Resonance*, 2019.
- [2] V. Badilita, R. C. Meier, N. Spengler, U. Wallrabe, M. Utz and J. G. Korvink, *Soft Matter*, 2012, **8**, 10583–10597.
- [3] R. C. Meier, J. Höfflin, V. Badilita, U. Wallrabe and J. G. Korvink, *J. Micromech. Microeng.*, 2014, **24**, 045021.
- [4] N. Spengler, A. Moazenzadeh, R. C. Meier, V. Badilita, J. Korvink and U. Wallrabe, *Journal of Micromechanics and Microengineering*, 2014, **24**, 034004.
- [5] H. Ryan, A. Smith and M. Utz, *Lab on a Chip*, 2014, **14**, 1678–1685.
- [6] D. A. Barskiy, A. M. Coffey, P. Nikolaou, D. M. Mikhaylov, B. M. Goodson, R. T. Branca, G. J. Lu, M. G. Shapiro, V.-V. Telkki, V. V. Zhivonitko *et al.*, *Chemistry—A European Journal*, 2017, **23**, 725–751.
- [7] M. A. Unger, H.-P. Chou, T. Thorsen, A. Scherer and S. R. Quake, *Science*, 2000, **288**, 113–116.
- [8] M. H. Levitt, *Spin dynamics: basics of nuclear magnetic resonance*, John Wiley Sons, 2001.
- [9] J. Keeler, *Understanding NMR spectroscopy*, John Wiley Sons, 2011.
- [10] F. Bloch, *Phys. Rev.*, 1946, **70**, 460–474.
- [11] P. A. M. Dirac, *Mathematical Proceedings of the Cambridge Philosophical Society*, 1939, **35**, 416–418.
- [12] J. von Neumann, *Mathematical Foundations of Quantum Mechanics*, Princeton University Press, new edn, 2018.
- [13] A. Webb, *Magn Reson Chem*, 2005, **43**, 688–696.
- [14] A. Abragam, *The Principles of Nuclear Magnetism*, Oxford University Press, 1961.
- [15] D. I. Hoult and R. E. Richards, *Journal of Magnetic Resonance (1969)*, 1976, **24**, 71–85.

- [16] P. J. M. van Bentum, J. W. G. Janssen, A. P. M. Kentgens, J. Bart and J. G. E. Gardeniers, *Journal of Magnetic Resonance*, 2007, **189**, 104–113.
- [17] G. Finch, A. Yilmaz and M. Utz, *Journal of Magnetic Resonance*, 2016, **262**, 73–80.
- [18] N. Spengler, J. Höfflin, A. Moazenzadeh, D. Mager, N. MacKinnon, V. Badilita, U. Wallrabe and J. G. Korvink, *PloS one*, 2016, **11**, e0146384.
- [19] I. Swyer, S. von der Ecken, B. Wu, A. Jenne, R. Soong, F. Vincent, D. Schmidig, T. Frei, F. Busse and H. J. Stronks, *Lab on a Chip*, 2019, **19**, 641–653.
- [20] W. Hale, G. Rossetto, R. Greenhalgh, G. Finch and M. Utz, *Lab Chip*, 2018, **18**, 3018–3024.
- [21] I. Kobayashi, Y. Wada, K. Uemura and M. Nakajima, *Microfluidics and Nanofluidics*, 2010, **8**, 255–262.
- [22] T. Thorsen, R. W. Roberts, F. H. Arnold and S. R. Quake, *Physical review letters*, 2001, **86**, 4163.
- [23] J. Zhang, R. J. Coulston, S. T. Jones, J. Geng, O. A. Scherman and C. Abell, *Science*, 2012, **335**, 690–694.
- [24] J. Ju, C. Zeng, L. Zhang and N. Xu, *Chemical Engineering Journal*, 2006, **116**, 115–121.
- [25] J. Kobayashi, Y. Mori, K. Okamoto, R. Akiyama, M. Ueno, T. Kitamori and S. Kobayashi, *Science*, 2004, **304**, 1305–1308.
- [26] U. Demirci and G. Montesano, *Lab on a Chip*, 2007, **7**, 1428–1433.
- [27] L. Mazutis, J. Gilbert, W. L. Ung, D. A. Weitz, A. D. Griffiths and J. A. Heyman, *Nature protocols*, 2013, **8**, 870.
- [28] W. Shi, J. Qin, N. Ye and B. Lin, *Lab on a Chip*, 2008, **8**, 1432–1435.
- [29] F. Schuler, M. Trotter, M. Geltman, F. Schwemmer, S. Wadle, E. Domínguez-Garrido, M. López, C. Cervera-Acedo, P. Santibáñez and F. von Stetten, *Lab on a Chip*, 2016, **16**, 208–216.
- [30] S. C. Kim, I. C. Clark, P. Shahi and A. R. Abate, *Analytical chemistry*, 2018, **90**, 1273–1279.
- [31] M. Y. Tang and H. C. Shum, *Lab on a Chip*, 2016, **16**, 4359–4365.
- [32] K. T. Kotz, Y. Gu and G. W. Faris, *Journal of the American Chemical Society*, 2005, **127**, 5736–5737.
- [33] S.-Y. Teh, R. Lin, L.-H. Hung and A. P. Lee, *Lab on a Chip*, 2008, **8**, 198–220.

- [34] M. He, J. S. Kuo and D. T. Chiu, *Applied Physics Letters*, 2005, **87**, 031916.
- [35] S.-H. Tan, N.-T. Nguyen, L. Yobas and T. G. Kang, *Journal of Micromechanics and Microengineering*, 2010, **20**, 045004.
- [36] B. Dura, M. M. Servos, R. M. Barry, H. L. Ploegh, S. K. Dougan and J. Voldman, *Proceedings of the National Academy of Sciences*, 2016, **113**, E3599–E3608.
- [37] W. Hale, G. Rossetto, R. Greenhalgh, G. Finch and M. Utz, *Lab on a Chip*, 2018.
- [38] P. Garstecki, I. Gitlin, W. DiLuzio, G. M. Whitesides, E. Kumacheva and H. A. Stone, *Applied Physics Letters*, 2004, **85**, 2649–2651.
- [39] P. Umbanhower, V. Prasad and D. A. Weitz, *Langmuir*, 2000, **16**, 347–351.
- [40] P. Zhu, T. Kong, Z. Kang, X. Tian and L. Wang, *Scientific reports*, 2015, **5**, 11102.
- [41] P. Zhu and L. Wang, *Lab on a Chip*, 2017, **17**, 34–75.
- [42] J. L. Markley, R. Brüschweiler, A. S. Edison, H. R. Eghbalnia, R. Powers, D. Raftery and D. S. Wishart, *Current opinion in biotechnology*, 2017, **43**, 34–40.
- [43] R. Powers, *Magnetic Resonance in Chemistry*, 2009, **47**, S2–S11.
- [44] V. Kasivisvanathan, A. S. Rannikko, M. Borghi, V. Panebianco, L. A. Mynderse, M. H. Vaarala, A. Briganti, L. Budäus, G. Hellawell and R. G. Hindley, *New England Journal of Medicine*, 2018, **378**, 1767–1777.
- [45] M. H. Horrocks, L. Tosatto, A. J. Dear, G. A. Garcia, M. Iljina, N. Cremades, M. Dalla Serra, T. P. Knowles, C. M. Dobson and D. Klenerman, *Analytical chemistry*, 2015, **87**, 8818–8826.
- [46] S. Schlimpert, K. Flärdh and M. J. Buttner, *JoVE (Journal of Visualized Experiments)*, 2016, e53863.
- [47] E. A. Redman, J. S. Mellors, J. A. Starkey and J. M. Ramsey, *Analytical chemistry*, 2016, **88**, 2220–2226.
- [48] K. Choi, E. Boyaci, J. Kim, B. Seale, L. Barrera-Arbelaez, J. Pawliszyn and A. R. Wheeler, *Journal of Chromatography A*, 2016, **1444**, 1–7.
- [49] J. D. Jackson, *Classical Electrodynamics*, John Wiley & Sons, 3rd edn, 2007.
- [50] M. H. Levitt, *Concepts Magn. Reson.*, 1996, **8**, 77–103.
- [51] P. W. Kuchel, B. E. Chapman, W. A. Bubb, P. E. Hansen, C. J. Durrant and M. P. Hertzberg, *Concepts in Magnetic Resonance Part A*, 2003, **18A**, 56–71.
- [52] J. C. VANDENENDEN, D. WADDINGTON, H. VANALST, C. G. VANKRALINGEN and K. J. PACKER, *Journal of Colloid and Interface Science*, 1990, **140**, 105–113.

- [53] I. FOUREL, J. P. GUILLEMENT and D. LEBOTLAN, *Journal of Colloid and Interface Science*, 1994, **164**, 48–53.
- [54] K. G. Hollingsworth, A. J. Sederman, C. Buckley, L. F. Gladden and M. L. Johns, *Journal of Colloid and Interface Science*, 2004, **274**, 244–250.
- [55] J. P. Hindmarsh, J. H. Su, J. Flanagan and H. Singh, *Langmuir*, 2005, **21**, 9076–9084.
- [56] M. L. Johns, *Current Opinion in Colloid & Interface Science*, 2009, **14**, 178–183.
- [57] R. Bernewitz, G. Guthausen and H. P. Schuchmann, *Magnetic Resonance in Chemistry*, 2011, **49**, S93–S104.
- [58] I. A. Lingwood, T. C. Chandrasekera, J. Kolz, E. O. Fridjonsson and M. L. Johns, *Journal of Magnetic Resonance*, 2012, **214**, 281–288.
- [59] M. E. Fabry and R. C. San George, *Biochemistry*, 1983, **22**, 4119–4125.
- [60] A. J. Lennon, N. R. Scott, B. E. Chapman and P. W. Kuchel, *Biophysical journal*, 1994, **67**, 2096–2109.
- [61] S. S. Zalesskiy, E. Danieli, B. Blümich and V. P. Ananikov, *Chem. Rev.*, 2014, **114**, 5641–5694.
- [62] N. Spengler, J. Höfflin, A. Moazenzadeh, D. Mager, N. MacKinnon, V. Badilita, U. Wallrabe and J. G. Korvink, *Plos One*, 2016, **11**, e0146384.
- [63] C. J. Durrant, M. P. Hertzberg and P. W. Kuchel, *Concepts Magn. Reson.*, 2003, **18A**, 72–95.
- [64] J. A. Peters, J. Huskens and D. J. Raber, *Progress in Nuclear Magnetic Resonance Spectroscopy*, 1996, **28**, 283–350.
- [65] *CRC Handbook of Chemistry and Physics*, ed. J. Rumble, 2017, pp. 1–4.
- [66] M. C. Wapler, J. Leupold, I. Dragonu, D. von Elverfeld, M. Zaitsev and U. Wallrabe, *Journal of Magnetic Resonance*, 2014, **242**, 233–242.
- [67] C. J. G. Bakker and R. de Roos, *Magn. Reson. Med.*, 2006, **56**, 1107–1113.
- [68] H. Ryan, A. Smith and M. Utz, *Lab Chip*, 2014, **14**, 1678–1685.
- [69] A. Yilmaz and M. Utz, *Lab Chip*, 2016, **16**, 2079–2085.
- [70] G. R. Finch, *PhD thesis*, University of Southampton, Southampton, 2017.
- [71] J. Bezanson, A. Edelman, S. Karpinski and V. B. Shah, *SIAM Rev.*, 2017, **59**, 65–98.
- [72] COMSOL Inc., *COMSOL Multiphysics®*, <https://www.comsol.com>.

- [73] Y. Takikawa, S. Ebisu and S. Nagata, *Journal of Physics and Chemistry of Solids*, 2010, **71**, 1592–1598.
- [74] J. Eills, W. Hale, M. Sharma, M. Rossetto, M. H. Levitt and M. Utz, *arXiv preprint arXiv:1901.07065*, 2019.
- [75] M. E. Halse, *TrAC Trends in Analytical Chemistry*, 2016, **83**, 76–83.
- [76] L. Schröder, T. J. Lowery, C. Hilty, D. E. Wemmer and A. Pines, *Science*, 2006, **314**, 446–449.
- [77] K. Golman and M. Thaning, *Proceedings of the National Academy of Sciences*, 2006, **103**, 11270–11275.
- [78] K. Ruppert, K. Qing, J. T. Patrie, T. A. Altes and J. P. Mugler III, *Academic radiology*, 2019, **26**, 355–366.
- [79] W. Zha, S. K. Nagle, R. V. Cadman, M. L. Schiebler and S. B. Fain, *Radiology*, 2018, **290**, 229–237.
- [80] Q. Chappuis, J. Milani, B. Vuichoud, A. Bornet, A. D. Gossert, G. Bodenhausen and S. Jannin, *The journal of physical chemistry letters*, 2015, **6**, 1674–1678.
- [81] Y. Kim, M. Liu and C. Hilty, *Analytical chemistry*, 2016, **88**, 11178–11183.
- [82] H. Allouche-Arnon, A. Gamliel, C. M. Barzilay, R. Nalbandian, J. M. Gomori, M. Karlsson, M. H. Lerche and R. Katz-Bruell, *Contrast media molecular imaging*, 2011, **6**, 139–147.
- [83] Y. Lee, G. S. Heo, H. Zeng, K. L. Wooley and C. Hilty, *Journal of the American Chemical Society*, 2013, **135**, 4636–4639.
- [84] M. Duewel, N. Vogel, C. K. Weiss, K. Landfester, H.-W. Spiess and K. Münnemann, *Macromolecules*, 2012, **45**, 1839–1846.
- [85] A. Bornet, M. Maucourt, C. Deborde, D. Jacob, J. Milani, B. Vuichoud, X. Ji, J.-N. Dumez, A. Moing and G. Bodenhausen, *Analytical chemistry*, 2016, **88**, 6179–6183.
- [86] N. Zacharias, J. Lee, S. Ramachandran, S. Shanmugavelandy, J. McHenry, P. Dutta, S. Millward, S. Gammon, E. Efstatheiu and P. Troncoso, *Molecular Imaging and Biology*, 2019, **21**, 86–94.
- [87] I. Romanenko, D. Gajan, R. Sayah, D. Crozet, E. Jeanneau, C. Lucas, L. Leroux, L. Veyre, A. Lesage and L. Emsley, *Angewandte Chemie International Edition*, 2015, **54**, 12937–12941.
- [88] T. Ong, W. Liao, V. Mougel, D. Gajan, A. Lesage, L. Emsley and C. Copéret, *Angewandte Chemie International Edition*, 2016, **55**, 4743–4747.

- [89] Y. Geiger, H. E. Gottlieb, U. Akbey, H. Oschkinat and G. Goobes, *Journal of the American Chemical Society*, 2016, **138**, 5561–5567.
- [90] L. Piveteau, T.-C. Ong, A. J. Rossini, L. Emsley, C. Coperet and M. V. Kovalenko, *Journal of the American Chemical Society*, 2015, **137**, 13964–13971.
- [91] Z. J. Berkson, R. J. Messinger, K. Na, Y. Seo, R. Ryoo and B. F. Chmelka, *Angewandte Chemie*, 2017, **129**, 5246–5251.
- [92] M. L. Hirsch, N. Kalechofsky, A. Belzer, M. Rosay and J. G. Kempf, *Journal of the American Chemical Society*, 2015, **137**, 8428–8434.
- [93] D. T. Peat, M. L. Hirsch, D. G. Gadian, A. J. Horsewill, J. R. Owers-Bradley and J. G. Kempf, *Physical Chemistry Chemical Physics*, 2016, **18**, 19173–19182.
- [94] G. Liu, M. Levien, N. Karschin, G. Parigi, C. Luchinat and M. Bennati, *Nature chemistry*, 2017, **9**, 676.
- [95] K. J. Pike, T. F. Kemp, H. Takahashi, R. Day, A. P. Howes, E. V. Kryukov, J. F. MacDonald, A. E. Collis, D. R. Bolton and R. J. Wylde, *Journal of Magnetic Resonance*, 2012, **215**, 1–9.
- [96] J. H. Ardenkjær-Larsen, B. Fridlund, A. Gram, G. Hansson, L. Hansson, M. H. Lerche, R. Servin, M. Thaning and K. Golman, *Proceedings of the National Academy of Sciences*, 2003, **100**, 10158–10163.
- [97] A. Gamliel, H. Allouche-Arnon, R. Nalbandian, C. M. Barzilay, J. M. Gomori and R. Katz-Bruell, *Applied Magnetic Resonance*, 2010, **39**, 329–345.
- [98] B. Feng, A. M. Coffey, R. D. Colon, E. Y. Chekmenev and K. W. Waddell, *Journal of Magnetic Resonance*, 2012, **214**, 258–262.
- [99] C. R. Bowers and D. P. Weitekamp, *Journal of the American Chemical Society*, 1987, **109**, 5541–5542.
- [100] M. G. Pravica and D. P. Weitekamp, *Chemical Physics Letters*, 1988, **145**, 255–258.
- [101] R. Zhou, W. Cheng, L. M. Neal, E. W. Zhao, K. Ludden, H. E. Hagelin-Weaver and C. R. Bowers, *Physical Chemistry Chemical Physics*, 2015, **17**, 26121–26129.
- [102] M. Maiwald, H. H. Fischer, Y.-K. Kim, K. Albert and H. Hasse, *J. Magn. Reson.*, 2004, **166**, 135–146.
- [103] D. A. Foley, E. Bez, A. Codina, K. L. Colson, M. Fey, R. Krull, D. Piroli, M. T. Zell and B. L. Marquez, *Analytical chemistry*, 2014, **86**, 12008–12013.
- [104] D. S. Wishart, *TrAC Trends in Analytical Chemistry*, 2008, **27**, 228–237.

- [105] M. Gottschalk, G. Ivanova, D. M. Collins, A. Eustace, R. O'Connor and D. F. Brougham, *NMR in Biomedicine*, 2008, **21**, 809–819.
- [106] M. Cuperlovic-Culf, D. A. Barnett, A. S. Culf and I. Chute, *Drug Discovery Today*, 2010, **15**, 610–621.
- [107] L. Shintu, R. Baudoin, V. Navratil, J. M. Prot, C. Pontoizeau, M. Defernez, B. J. Blaise, C. Domange, A. R. R. Péry and P. Toulhoat, *Analytical chemistry*, 2012.
- [108] D. Olson, T. Peck, A. Webb, R. Magin and J. Sweedler, *Science*, 1995, **270**, 1967–1970.
- [109] J. Bart, A. J. Kolkman, A. J. Oosthoek-de Vries, K. Koch, P. J. Nieuwland, H. J. W. G. Janssen, P. J. M. van Bentum, K. A. M. Ampt, F. P. J. T. Rutjes, S. S. Wijmenga, H. J. G. E. Gardeniers and A. P. M. Kentgens, *J Am Chem Soc*, 2009, **131**, 5014–5015.
- [110] J. Wang, G. Sui, V. P. Mocharla, R. J. Lin, M. E. Phelps, H. C. Kolb and H.-R. Tseng, *Angew. Chem.*, 2006, **118**, 5402–5407.
- [111] A. B. Theberge, E. Mayot, A. El Harrak, F. Kleinschmidt, W. T. S. Huck and A. D. Griffiths, *Lab Chip*, 2012, **12**, 1320–1326.
- [112] P. H. Hoang, C. T. Nguyen, J. Perumal and D.-P. Kim, *Lab Chip*, 2011, **11**, 329–335.
- [113] K. i. Ohno, K. Tachikawa and A. Manz, *Electrophoresis*, 2008, **29**, 4443–4453.
- [114] X. Zhou, S. Cai, A. Hong, Q. You, P. Yu, N. Sheng, O. Srivannavit, S. Muranjan, J. M. Rouillard and Y. Xia, *Nucleic acids research*, 2004, **32**, 5409–5417.
- [115] H. Fang, Y. Sun, X. Wang, M. Sharma, Z. Chen, X. Cao, M. Utz and Z. Tian, *Sci. China Chem.*, 2018, **61**, 1460–1464.
- [116] P. H. Hoang, H. Park and D.-P. Kim, *J Am Chem Soc*, 2011, **133**, 14765–14770.
- [117] A. Günther and K. Jensen, *Lab Chip*, 2006, **6**, 1487–1503.
- [118] A. Manz, N. Gruber and H. WIDMER, *Sensor Actuat B-Chem*, 1990, **1**, 244–248.
- [119] G. M. Whitesides, *Nature*, 2006, **442**, 368–373.
- [120] J. El-Ali, P. K. Sorger and K. F. Jensen, *Nature*, 2006, **442**, 403–411.
- [121] J. West, M. Becker, S. Tombrink and A. Manz, *Analytical chemistry*, 2008, **80**, 4403–4419.
- [122] P. Neužil, S. Giselbrecht, K. Länge, T. J. Huang and A. Manz, *Nature Reviews Drug Discovery*, 2012, **11**, 620–632.

- [123] A. D. Gracz, I. A. Williamson, K. C. Roche, M. J. Johnston, F. Wang, Y. Wang, P. J. Attayek, J. Balowski, X. F. Liu, R. J. Laurenza, L. T. Gaynor, C. E. Sims, J. A. Galanko, L. Li, N. L. Allbritton and S. T. Magness, *Nature Cell Biology*, 2015, **17**, 340–349.
- [124] H. Ryan, S.-H. Song, A. Zaß, J. Korvink and M. Utz, *Anal. Chem.*, 2012, **84**, 3696–3702.
- [125] N. Spengler, A. Moazenzadeh, R. C. Meier, V. Badilita, J. G. Korvink and U. Wallrabe, *J. Micromech. Microeng.*, 2014, **24**, 034004.
- [126] D. Rugar, C. S. Yannoni and J. Sidles, *Nature*, 1992, **360**, 563–566.
- [127] D. Rugar, R. Budakian, H. J. Mamin and B. W. Chui, *Nature*, 2004, **430**, 329–332.
- [128] H. J. Mamin, M. Poggio, C. L. Degen and D. Rugar, *Nature Nanotech*, 2007, **2**, 301–306.
- [129] M. Poggio and C. L. Degen, *Nanotechnology*, 2010, **21**, 342001.
- [130] J. R. Maze, P. L. Stanwix, J. S. Hodges, S. Hong, J. M. Taylor, P. Cappellaro, L. Jiang, M. V. G. Dutt, E. Togan, A. S. Zibrov, A. Yacoby, R. L. Walsworth and M. D. Lukin, *Nature*, 2008, **455**, 644–647.
- [131] T. Staudacher, F. Shi, S. Pezzagna, J. Meijer, J. Du, C. A. Meriles, F. Reinhard and J. Wrachtrup, *Science*, 2013, **339**, 561–563.
- [132] D. Rugar, H. J. Mamin, M. H. Sherwood, M. Kim, C. T. Rettner, K. Ohno and D. D. Awschalom, *Nature Nanotech*, 2015, **10**, 120–124.
- [133] R. McDermott, A. H. Trabesinger, M. Mück, E. L. Hahn, A. Pines and J. Clarke, *Science*, 2002, **295**, 2247–2249.
- [134] D. Budker and M. Romalis, *NATURE PHYSICS*, 2007, **3**, 227–234.
- [135] S. Xu, V. V. Yashchuk, M. H. Donaldson, S. M. Rochester, D. Budker and A. Pines, *Proceedings of the National Academy of Sciences*, 2006, **103**, 12668–12671.
- [136] J. W. Blanchard, M. P. Ledbetter, T. Theis, M. C. Butler, D. Budker and A. Pines, *J Am Chem Soc*, 2013, **135**, 3607–3612.
- [137] D. R. Glenn, D. B. Bucher, J. Lee, M. D. Lukin, H. Park and R. L. Walsworth, *Nature*, 2018, **555**, 351–354.
- [138] K. Münnemann and H. W. Spiess, *Nature Physics*, 2011, **7**, 522.
- [139] E. McDonnell, S. Han, C. Hilty, K. Pierce and A. Pines, *Anal. Chem.*, 2005, **77**, 8109–8114.

- [140] H. Desvaux, D. J. Y. Marion, G. Huber and P. Berthault, *Angewandte Chemie International Edition*, 2009, **48**, 4341–4343.
- [141] V.-V. Telkki, V. V. Zhivonitko, S. Ahola, K. V. Kovtunov, J. Jokisaari and I. V. Koptyug, *Angewandte Chemie International Edition*, 2010, **49**, 8363–8366.
- [142] E. Paciok and B. Blümich, *ANGEWANDTE CHEMIE-INTERNATIONAL EDITION IN ENGLISH-*, 2011, **50**, 5258–5260.
- [143] R. Jiménez-Martínez, D. J. Kennedy, M. Rosenbluh, E. A. Donley, S. Knappe, S. J. Seltzer, H. L. Ring, V. S. Bajaj and J. Kitching, *Nature Communications*, 2014, **5**, 3908.
- [144] A. Causier, G. Carret, C. Boutin, T. Berthelot and P. Berthault, *Lab Chip*, 2015, **15**, 2049–2054.
- [145] W. Hale, J. Eills, M. Rossetto, M. Levitt and M. Utz, Oral presentation, Euromar conference, Nantes, 2018.
- [146] L. Bordonali, N. Nordin, E. Fuhrer, N. MacKinnon and J. G. Korvink, *Lab Chip*, 2019, **19**, 503–512.
- [147] J.-B. Hövener, A. N. Pravdivtsev, B. Kidd, C. R. Bowers, S. Glöggler, K. V. Kovtunov, M. Plaumann, R. Katz-Brull, K. Buckenmaier and A. Jerschow, *Angewandte Chemie International Edition*, 2018, **57**, 11140–11162.
- [148] S. B. Duckett and R. E. Mewis, *Accounts of chemical research*, 2012, **45**, 1247–1257.
- [149] S. Glöggler, J. Colell and S. Appelt, *Journal of Magnetic Resonance*, 2013, **235**, 130–142.
- [150] R. A. Green, R. W. Adams, S. B. Duckett, R. E. Mewis, D. C. Williamson and G. G. Green, *Progress in nuclear magnetic resonance spectroscopy*, 2012, 1–48.
- [151] P. Bhattacharya, E. Y. Chekmenev, W. H. Perman, K. C. Harris, A. P. Lin, V. A. Norton, C. T. Tan, B. D. Ross and D. P. Weitekamp, *Journal of magnetic resonance*, 2007, **186**, 150–155.
- [152] E. Y. Chekmenev, J. Hövener, V. A. Norton, K. Harris, L. S. Batchelder, P. Bhattacharya, B. D. Ross and D. P. Weitekamp, *Journal of the American Chemical Society*, 2008, **130**, 4212–4213.
- [153] E. Y. Chekmenev, V. A. Norton, D. P. Weitekamp and P. Bhattacharya, *Journal of the American Chemical Society*, 2009, **131**, 3164–3165.
- [154] R. V. Shchepin, A. M. Coffey, K. W. Waddell and E. Y. Chekmenev, *Analytical chemistry*, 2014, **86**, 5601–5605.

- [155] F. Reineri, T. Boi and S. Aime, *Nature Communications*, 2015, **6**, 5858.
- [156] E. Cavallari, C. Carrera, M. Sorge, G. Bonne, A. Muchir, S. Aime and F. Reineri, *Scientific reports*, 2018, **8**, 8366.
- [157] J. Eills, G. Stevanato, C. Bengs, S. Glöggler, S. J. Elliott, J. Alonso-Valdesueiro, G. Pileio and M. H. Levitt, *Journal of Magnetic Resonance*, 2017, **274**, 163–172.
- [158] M. Roth, P. Kindervater, H. P. Raich, J. Bargon, H. W. Spiess and K. Münnemann, *Angew. Chem.*, 2010, **122**, 8536–8540.
- [159] S. Lehmkuhl, M. Wiese, L. Schubert, M. Held, M. Küppers, M. Wessling and B. Blümich, *Journal of Magnetic Resonance*, 2018, **291**, 8–13.
- [160] P. Giraudeau, Y. Shrot and L. Frydman, *J Am Chem Soc*, 2009, **131**, 13902–13903.
- [161] L. S. Lloyd, R. W. Adams, M. Bernstein, S. Coombes, S. B. Duckett, G. G. R. Green, R. J. Lewis, R. E. Mewis and C. J. Sleigh, *J Am Chem Soc*, 2012, **134**, 12904–12907.
- [162] N. Eshuis, R. L. E. G. Aspers, B. J. A. van Weerdenburg, M. C. Feiters, F. P. J. T. Rutjes, S. S. Wijmenga and M. Tessari, *Angew. Chem.*, 2015, **127**, 14735–14738.
- [163] E. Cavallari, C. Carrera, T. Boi, S. Aime and F. Reineri, *The Journal of Physical Chemistry B*, 2015, **119**, 10035–10041.
- [164] L. Bordonali, N. Nordin, E. Fuhrer, N. MacKinnon and J. G. Korvink, *Lab Chip*, 2019, **19**, 503–512.
- [165] M. Mompeán, R. M. Sánchez-Donoso, A. Hoz, V. Saggiomo, A. H. Velders and M. V. Gomez, *Nature communications*, 2018, **9**, 108.
- [166] M. Mishkovsky and L. Frydman, *Chemphyschem*, 2008, **9**, 2340–2348.
- [167] A. S. Kiryutin, G. Sauer, D. Tietze, M. Brodrecht, S. Knecht, A. V. Yurkovskaya, K. L. Ivanov, O. Avrutina, H. Kolmar and G. Buntkowsky, *Chemistry - A European Journal*, 2019, **32**, 211–7.
- [168] J. Hovener, A. N. Pravdivtsev, B. Kidd, C. R. Bowers, S. Glöggler, K. V. Kovtunov, M. Plaumann, R. Katz-Brull, K. Buckenmaier, A. Jerschow, F. Reineri, T. Theis, R. V. Shchepin, S. Wagner, N. M. M. Zacharias, P. Bhattacharya and E. Y. Chekmenev, *Angew. Chem.*, 2018.
- [169] M. Goldman, H. Johannesson, O. Axelsson and M. Karlsson, *Magn Reson Imaging*, 2005, **23**, 153–157.
- [170] M. Goldman, H. Johannesson, O. Axelsson and M. Karlsson, *Comptes Rendus Chimie*, 2006, **9**, 357–363.

- [171] B. Ripka, J. Eills, H. Kouřilová, M. Leutzsch, M. H. Levitt and K. Münnemann, *Chemical Communications*, 2018.
- [172] S. S. Roy, K. M. Appleby, E. J. Fear and S. B. Duckett, *The journal of physical chemistry letters*, 2018, **9**, 1112–1117.
- [173] F. Reineri, T. Boi and S. Aime, *Nature communications*, 2015, **6**, 5858.
- [174] B. Ripka, J. Eills, H. Kouřilová, M. Leutzsch, M. H. Levitt and K. Münnemann, *Chem. Commun.*, 2018, **54**, 12246–12249.
- [175] S. Korchak, S. Yang, S. Mamone and S. Glöggler, *ChemistryOpen*, 2018, **7**, 344–348.
- [176] J. Liu, B. A. Williams, R. M. Gwirtz, B. J. Wold and S. Quake, *Angewandte Chemie International Edition*, 2006, **45**, 3618–3623.
- [177] S. Huang, C. Li, B. Lin and J. Qin, *Lab on a Chip*, 2010, **10**, 2925–2931.
- [178] L. Jiang, Y. Zeng, Q. Sun, Y. Sun, Z. Guo, J. Y. Qu and S. Yao, *Analytical chemistry*, 2015, **87**, 5589–5595.
- [179] I. N. Kefala, V. E. Papadopoulos, G. Karpou, G. Kokkoris, G. Papadakis and A. Tserepi, *Microfluidics and Nanofluidics*, 2015, **19**, 1047–1059.
- [180] A. G. Hadd, D. E. Raymond, J. W. Halliwell, S. C. Jacobson and J. M. Ramsey, *Analytical chemistry*, 1997, **69**, 3407–3412.
- [181] M. C. Mitchell, V. Spikmans and A. J. de Mello, *Analyst*, 2001, **126**, 24–27.
- [182] H. Kim, K.-I. Min, K. Inoue, D.-P. Kim and J.-i. Yoshida, *Science*, 2016, **352**, 691–694.
- [183] H. Fang, Y. Sun, X. Wang, M. Sharma, Z. Chen, X. Cao, M. Utz and Z. Tian, *Science China Chemistry*, 2018, **61**, 1460–1464.
- [184] A.-L. Liu, Z.-Q. Li, Z.-Q. Wu and X.-H. Xia, *Talanta*, 2018, **182**, 544–548.
- [185] H. Gong, A. T. Woolley and G. P. Nordin, *Lab on a Chip*, 2016, **16**, 2450–2458.
- [186] A. K. Au, N. Bhattacharjee, L. F. Horowitz, T. C. Chang and A. Folch, *Lab on a chip*, 2015, **15**, 1934–1941.
- [187] A. Terray, J. Oakey and D. W. Marr, *Science*, 2002, **296**, 1841–1844.
- [188] Z. Li, S. Y. Mak, A. Sauret and H. C. Shum, *Lab on a Chip*, 2014, **14**, 744–749.
- [189] T. Ward, M. Faivre, M. Abkarian and H. A. Stone, *Electrophoresis*, 2005, **26**, 3716–3724.

- [190] M. A. Unger, H.-P. Chou, T. Thorsen, A. Scherer and S. R. Quake, *Science*, 2000, **288**, 113–116.
- [191] V. Studer, G. Hang, A. Pandolfi, M. Ortiz, W. French Anderson and S. R. Quake, *Journal of applied physics*, 2004, **95**, 393–398.
- [192] C. Vicider, O. Ohman and H. Elderstig, Proceedings of the International Solid-State Sensors and Actuators Conference-TRANSDUCERS'95, pp. 284–286.
- [193] A. R. Wheeler, *Science*, 2008, **322**, 539–540.
- [194] W. Cui, M. Zhang, X. Duan, W. Pang, D. Zhang and H. Zhang, *Micromachines*, 2015, **6**, 778–789.
- [195] Y. Oda, H. Oshima, M. Nakatani and M. Hashimoto, *Electrophoresis*, 2019, **40**, 414–418.
- [196] C. H. Chen, S. H. Cho, F. Tsai, A. Erten and Y.-H. Lo, *Biomedical microdevices*, 2009, **11**, 1223.
- [197] A. Hatch, A. E. Kamholz, G. Holman, P. Yager and K. F. Bohringer, *Journal of Microelectromechanical systems*, 2001, **10**, 215–221.
- [198] J. Belardi, N. Schorr, O. Prucker and J. Rühe, *Advanced Functional Materials*, 2011, **21**, 3314–3320.
- [199] B. S. Lee, Y. U. Lee, H.-S. Kim, T.-H. Kim, J. Park, J.-G. Lee, J. Kim, H. Kim, W. G. Lee and Y.-K. Cho, *Lab on a Chip*, 2011, **11**, 70–78.
- [200] S. T. Krauss, T. P. Remcho, S. M. Lipes, R. Aranda IV, H. P. Maynard III, N. Shukla, J. Li, R. E. Tontarski Jr and J. P. Landers, *Analytical chemistry*, 2016, **88**, 8689–8697.
- [201] B. S. Lee, J.-N. Lee, J.-M. Park, J.-G. Lee, S. Kim, Y.-K. Cho and C. Ko, *Lab on a Chip*, 2009, **9**, 1548–1555.
- [202] G. Finch, A. Yilmaz and M. Utz, *Journal of Magnetic Resonance*, 2016, **262**, 73–80.
- [203] D. C. Leslie, C. J. Easley, E. Seker, J. M. Karlinsey, M. Utz, M. R. Begley and J. P. Landers, *Nature Physics*, 2009, **5**, 231.